Spring 2013

Geophysical Expression of the Northern Part of the Mono-Inyo Volcanic Chain, Mono Basin, California

Amanda McDonell
San Jose State University

GEOPHYSICAL EXPRESSION OF THE NORTHERN PART OF THE MONO-INYO VOLCANIC CHAIN, MONO BASIN, CALIFORNIA

A Thesis

Presented to

The Faculty of the Department of Geology

San Jose State University

In partial fulfillment

Of the requirements for the degree

Masters of Science

by

Amanda Pera McDonell

May 2013

The Designated Committee Approves the Thesis Titled

GEOPHYSICAL EXPRESSION OF THE NORTHEN PART OF THE MONO-INYO VOLCANIC CHAIN, MONO BASIN, CALIFORNIA

by

Amanda Pera McDonell

APPROVED FOR THE DEPARTMENT OF GEOLOGY

SAN JOSE STATE UNIVERSITY

May 2013

Dr. Jonathan Miller	Department of Geology
Dr. Maurizio Battaglia	Department of Geology
Dr. Richard Sedlock	Department of Geology
Dr. Darcy McPhee	U.S. Geological Survey

ABSTRACT

GEOPHYSICAL EXPRESSION OF THE NORTHERN PART OF THE MONO-INYO VOLCANIC CHAIN, MONO BASIN, CALIFORNIA

by Amanda Pera McDonell

The Mono Domes are located at the northernmost end of the Mono-Inyo volcanic chain just north of the Long Valley Caldera and include more than 30 overlapping domes and coulees that follow an arcuate trend. A shallow basement high, possibly bounded by a fault, as suggested by potential-field models of data collected in Mono Basin, California, may have influenced the geometry and location of the Mono Domes.

Over 320 new gravity stations and approximately 297 line-km of ground magnetic data were collected during the summer of 2010 to investigate the subsurface structure of the Mono Basin. Regional gravity data were collected throughout the basin, and ground magnetic data were collected on major roads along numerous transects throughout the region, one of which was coincident with a seismic refraction line. Gravity and magnetic data were compiled with pre-existing data from studies dating back to the 1960's to produce a new regional isostatic gravity anomaly map and ground magnetic profiles throughout the basin.

Aeromagnetic and ground magnetic data revealed an anomalous ring-shaped magnetic high centered over Aeolian Buttes, whose eastern margin follows the arcuate trend of the Mono Domes. This magnetic high is essentially coincident with what Kistler

(1966) inferred to be a ring-fracture. Two-dimensional forward modeling of potential field data along a profile across the basin suggests a basement high, or ridge, at roughly 700 m depth, the eastern edge of which lies beneath the Mono Domes. The basement ridge is probably fractured, as suggested by potential field data, indicating a possible pre-existing fault beneath the Mono Domes. This fault is along the eastern edge of the basement ridge and could have served as a conduit for the Mono Domes feeder dike.

ACKNOWLEGEMENTS

This thesis project would not have been possible without the support of many people. My deepest appreciation goes to my thesis committee for their continued encouragement and support. I would like to thank Dr. Jonathan Miller for having confidence in me and giving me the opportunity to work on this project. I would also like to thank Dr. Maurizio Battaglia for taking me on as a student and providing invaluable guidance throughout the thesis. It is an honor to have had Dr. Maggie Mangan as a supervisor and mentor and to have her support and encouragement, and for introducing me to the GUMP group. I am very fortunate to have been under the supervision of such an amazing woman/scientist. I owe my deepest gratitude to Dr. Darcy McPhee and Dave Ponce for teaching me more than any potential field geophysics book or class could have ever taught me, and for opportunities I would have never had without their help. I cannot find the words to express my appreciation to Dave for his mentoring and advising through every aspect of this work and for his patience and understanding, no matter how small the question. It was a privilege to work with both Darcy and Dave and never in my dreams would I have expected a thesis project to be as fun and exciting as this was; I will never forget my experience working with everyone at the USGS. I would also like to thank Erin Looby, John Spritzer, Bruce Chuchle, Janet Watt, Dave Hill, Mae Marcaida, Kevin Denton, Carole Tomasello, and Angela Jayko for their help and support in the field and the office.

TABLE OF CONTENTS

LIST OF FIGURES

LIST OF TABLES

INTRODUCTION

Geological studies suggest that of the several systems that form the Long Valley volcanic region (eastern California), the Mono Domes volcanic chain located in the Mono Basin appears to hold the greatest potential for renewed magmatic activity (Hildreth, 2004). Although the Mono Domes represent some of the youngest foci of volcanic activity in the region, the latest geophysical investigations were conducted in the mid-1980's, more than twenty years ago.

The Mono Basin is also a region of geothermal interest. The Long Valley caldera is located just south of the Mono Basin and is home to the Casa Diablo geothermal plant, which generates roughly 40 megawatts of electricity for Mammoth Pacific. Because the Mono Basin is a volcanically active area with the most recent eruption only 250 years ago, the region may hold geothermal potential.

In an attempt to characterize and explore the subsurface structure of Mono Basin several geophysical studies were conducted. Previous gravity and magnetic investigations focused on the depth, geometry, density distribution, and magnetization of Mono Basin (Pakiser and others, 1960; Gilbert and others, 1968; Christensen, 1969; Pakiser 1976). Other studies with geothermal motivations were conducted to determine the depth and geometry of a possible magma source beneath Mono Domes (Hermance and others, 1984; Hill and others, 1985; Achauer and others, 1986). However, many contrasting conclusions have been drawn from these works, and few constraints have been placed on the density distribution and subsurface structure across the Mono Domes.

In the summer of 2010, we collected new regional gravity and ground magnetic data in and around the Mono Domes to improve the gravity and magnetic coverage throughout the region. New gravity data were compiled with an existing gravity database (Battaglia et al, 2003) to produce a new regional isostatic gravity anomaly map. In addition, a ground magnetic anomaly map was also produced from the newly collected data. Utilizing the new data and modern technology, such as state-of-the-art Geographic Positioning System (GPS) equipment and modeling software, we were able to provide a fresh interpretation of the Mono Domes subsurface structure.

In this work, we presented two-dimensional subsurface models derived from the integrated gravity and existing aeromagnetic data that better constrain the density and magnetization distribution, depth, and structure of the Mono Domes region within the Mono Basin. These efforts were critical to improving the dynamic modeling of active range front-faulting and eruptions by dike intrusion in the Mono Basin (e.g., Bursik and others, 2003). The structural model based on the regional gravity and magnetic surveys provided a useful framework to better assess the potential geothermal resources and volcanic hazards of the region.

TECTONIC SETTING

The Mono Basin is bounded by the Bodie Hills on the north, Long Valley Caldera on the south, Cowtrack Mountains on the east, and the Sierra Nevada on the west (Fig. 1). The majority of the basin consists of quaternary alluvium, tertiary volcanic rocks, and pre-Cenozoic rocks including granitic basement and metasedimentary rocks (Fig. 2).

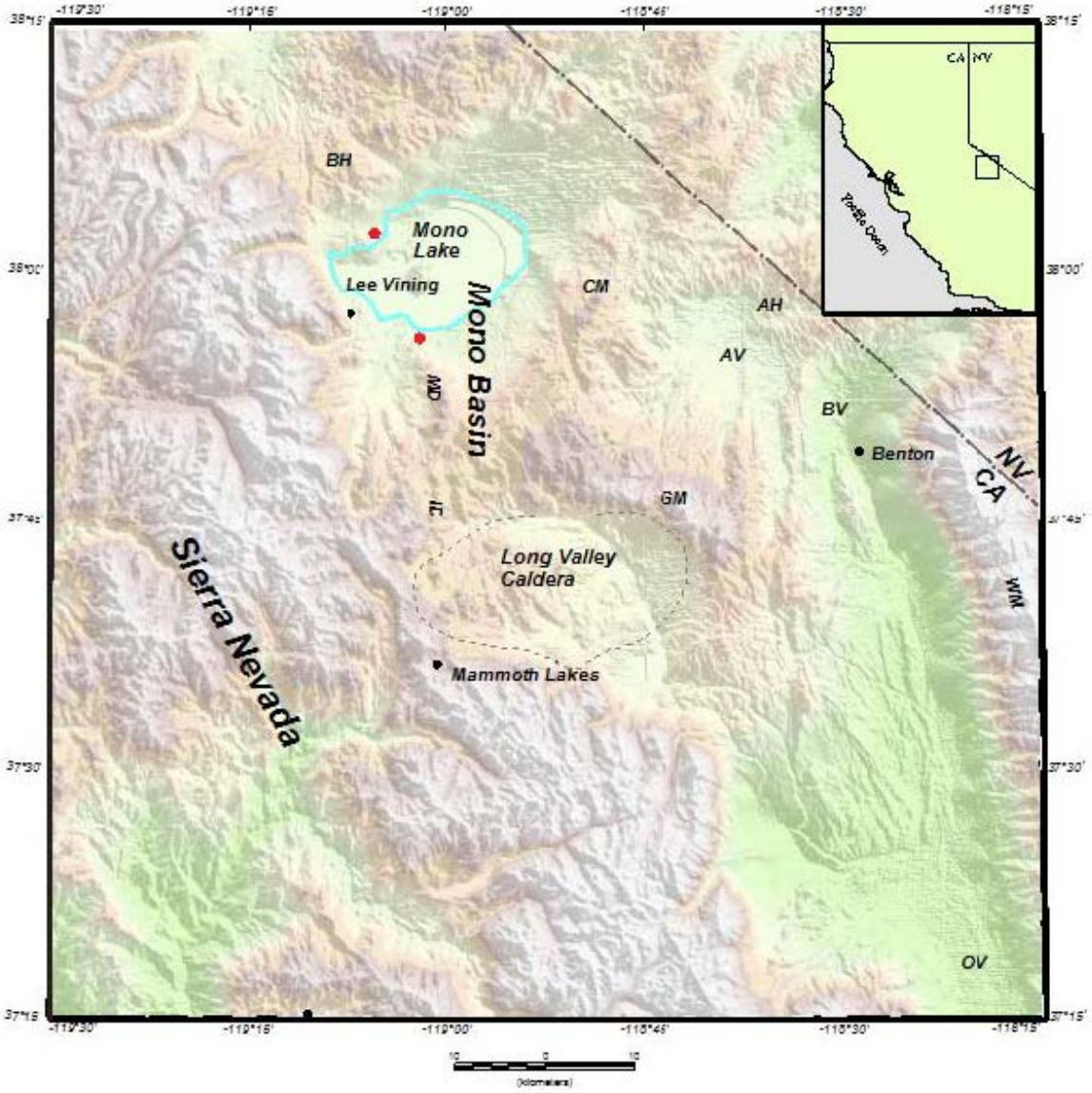

Figure 1. Index map of the Mono Basin study area. BH, Bodie Hills; CM, Cowtrack Mountain; AH, Adobe Hills; AV, Adobe Valley; MD, Mono Domes; ID, Inyo domes; GM, Glass Moutain; WM, White Mountains; OV, Owens Valley; BV, Benton Valley. Black box in inset map shows the map location in California and Nevada. Red dots show approximate locations of geothermal wells (Axtell, 1972), "State PRC 4572.1" located on the northwest shore and "State PRC 4397.1" is located on the south shore of Mono Lake.

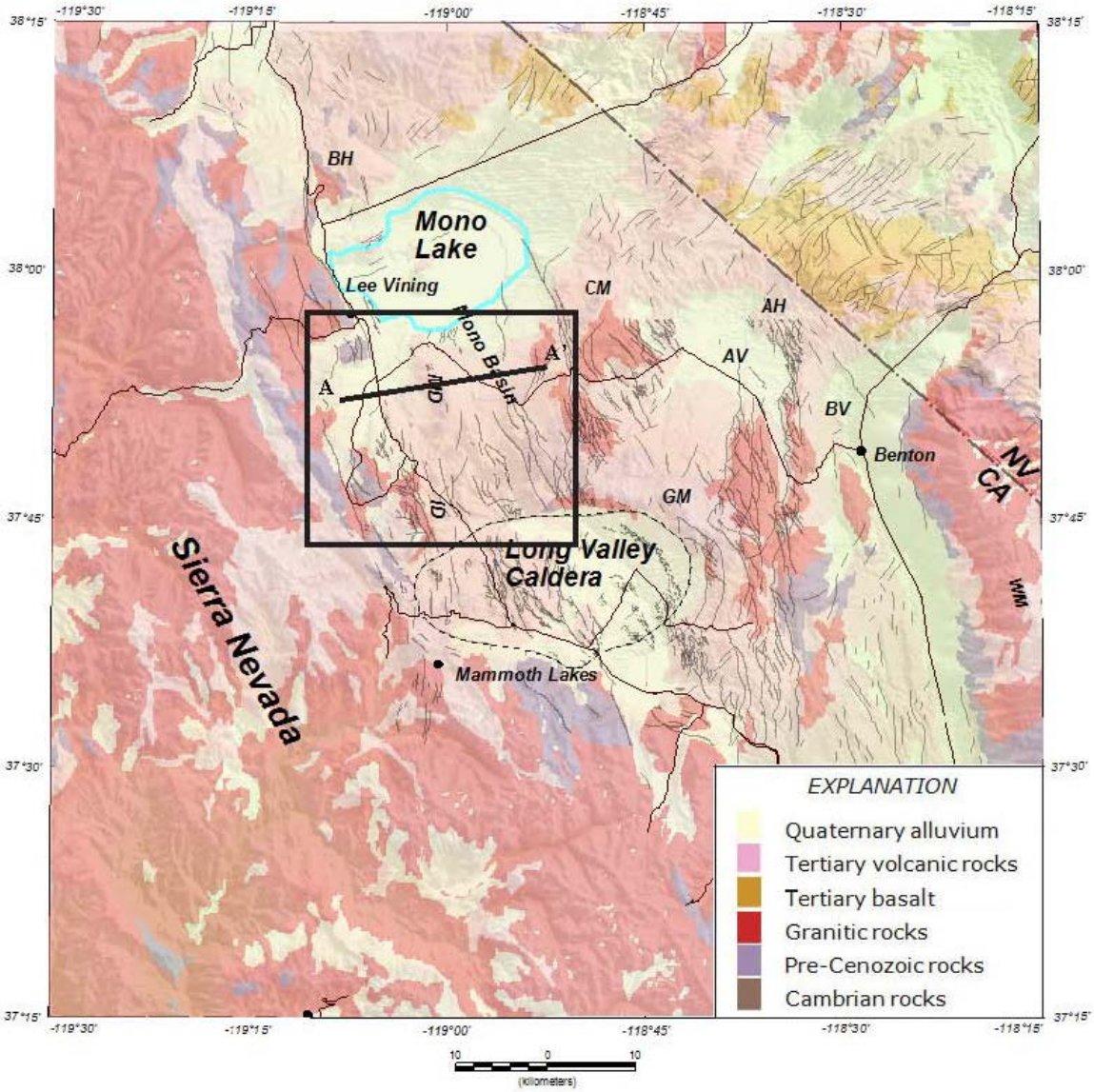

Figure 2. Simplified geologic map of the study area shown in Figure 1, modified from Jenning and others (1977) and Stewart and Carlson (1978). Grey lines represent faults from Bailey (1989) and Jennings and others (1977). The black box shows location of Figure 4. Profile A-A' shows location of the potential field model.

Mesozoic basement rocks within Mono Basin consists of quartz monzonite, granodiorite, diorite, gabbro, and other granitic rocks (Kistler, 1966; Bailey, 1989). The Mono Basin is located to the north of the Owens Valley graben in a left-lateral step in the

eastern escarpment of the Sierra Nevada. The basin lies on the western boundary of the Basin and Range Province, adjacent to large east-dipping normal faults of the eastern Sierra Nevada escarpment. Volcanism and tectonic deformation in this zone are contemporaneous, and most likely associated with the upwelling of magma into the crust from the underlying asthenosphere as the crust stretches, thins, and occasionally fractures in response to transtensional deformation (Hill, 2006).

Post-Miocene volcanism in the Mono Basin is related to the northern extensional Eastern California Shear Zone (ECSZ) and its continuation to the north along the southern Walker Lane Belt (WLB) in western Nevada (Fig. 3). This region has been tectonically influenced by extension of the crust across the Basin and Range to the west and by strike-slip motion along the Pacific and North American transform plate boundary (Hill, 2006). Dextral slip across the transtensional ECSZ and WLB accounts for 15-25% of the relative Pacific and North American plate motion, most of which is not on the San Andreas Fault System (Henry and Faulds, 2005). Linking the ECSZ and the WLB is the Mina Deflection (Fig. 3), a zone of several large pull-apart structures that are structurally controlled by NE-striking normal faults that transfer slip from the ECSZ to WLB, in which slip transfer is accommodated along dextral, sinistral and normal faults (Lee and Stockli, 2005). The Mina Deflection along with a 100-km wide topographic swell centered on the Mono Basin has been a significant component in Pliocene to recent volcanism within the region (Hill, 2006).

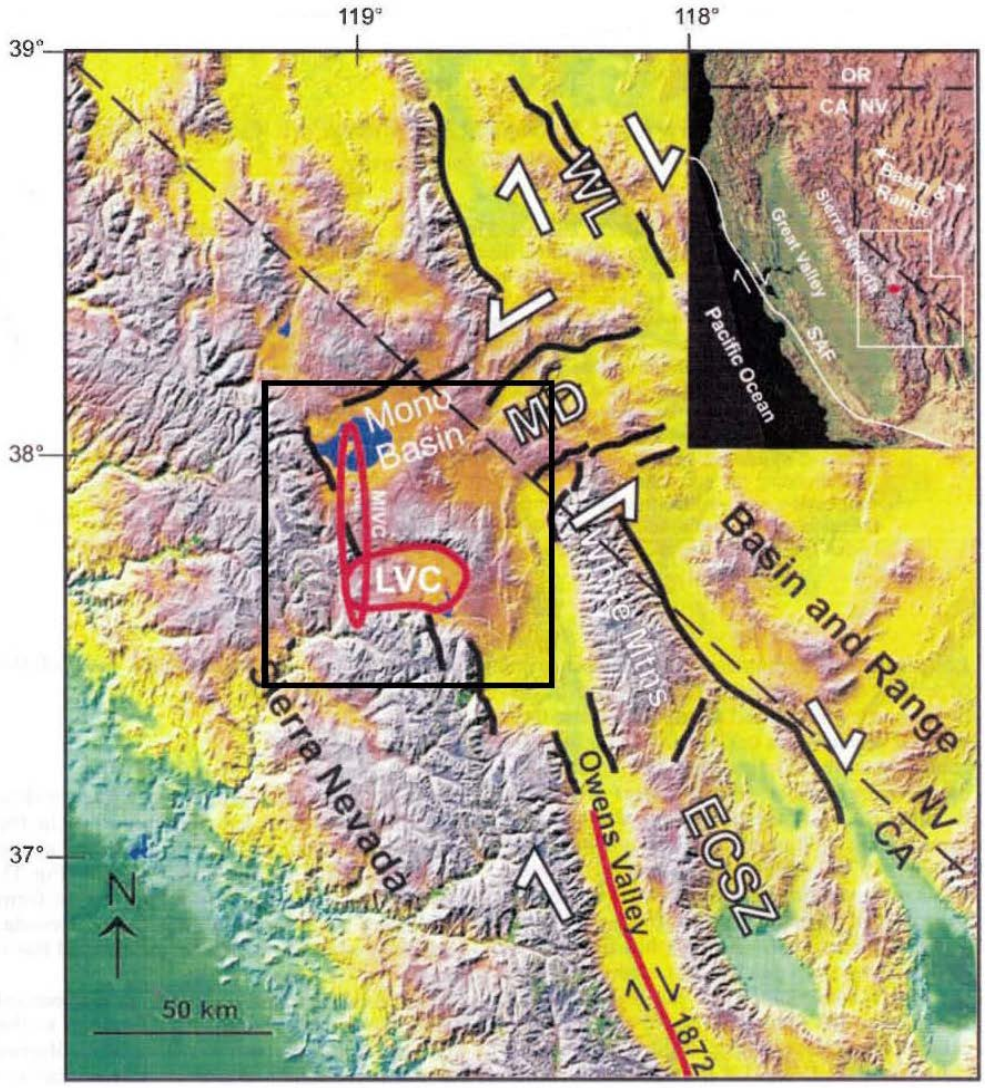

Figure 3. Map of eastern California and western Nevada (Hill, 2006) showing the direction of displacement along the Walker Lane belt (WL), the Mina deflection (MD), and the Eastern California Shear Zone (ECSZ). The location of the Mono-Inyo volcanic chain (MIVC) is shown by the north-south elongated red oval. Solid black lines indicate major Quaternary faults. The Long Valley Caldera (LVC) is outlined in red. The black box outlines the study area.

Mono Domes

The Mono Domes are defined by a 17-km long arcuate ridge of over 30 domes, coulees, and explosion domes between June Lake and Mono Lake (Fig. 4). The ridge has a maximum elevation of 2,800 m. Volcanic activity of the Mono Domes began 40 ka and continued through recent times. All but one of the Mono Domes lavas are composed of high-silica rhyolite. Most of the lavas are Holocene in age, three are approximately 13 ka, and one is 20 ka (Hildreth, 2004). The older Mono Domes (40-3 ka) are porhyritic and the younger domes (3 ka – 550 yr) are aphyric, suggesting a rise in temperature in the magma chamber or the source coming from a greater depth (Bailey, 1989). A group of young vents within and adjacent to Mono Lake follow the approximate trend of the Mono Domes. However, they are compositionally different and are considered to be independent of the magma reservoir that supplies the Mono Domes (Hildreth, 2004).

The youngest eruptions at the north end of Mono Domes are dated at 660 ± 20 yr and may have been be fed by a 6 km-long dike (Bursik and Sieh, 1989). The eruptions of the North Mono Domes were followed by the most recent eruption of the Inyo Domes. The interval between the eruptions is believed to be between one to two years as suggested by minor disturbances of the North Mono tephra prior to deposition of the Inyo tephra and the time frame of activity is indicative of a genetic relationship (Sieh and Bursik, 1986).

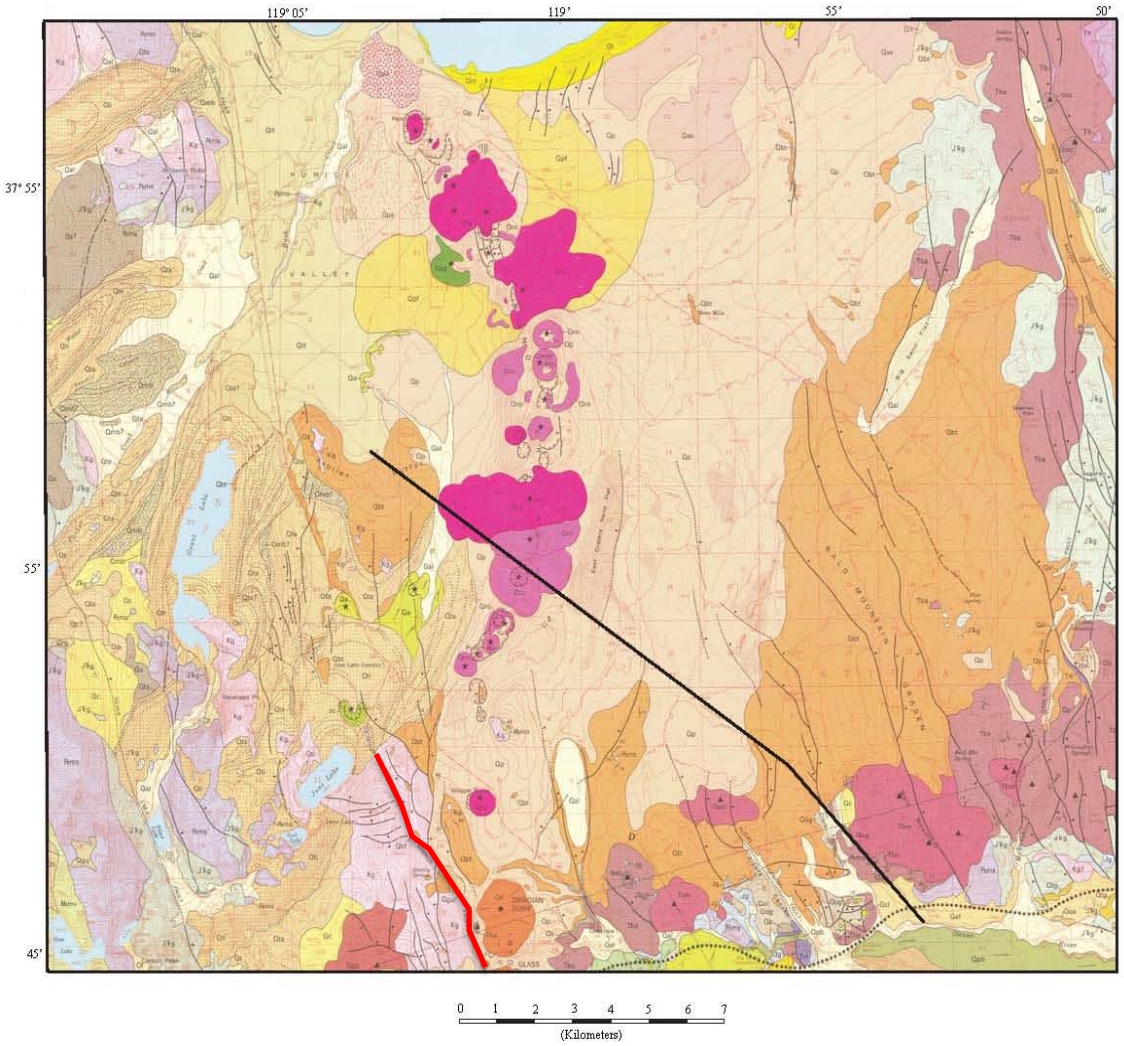

Figure 4. Modified geologic map of the Mono Basin study area (Bailey, 1989). Bold black line shows the approximate location of the Mono Craters Tunnel, red line shows the approximate location of the Hartley Springs Fault. Magenta, Mono Domes; Orange, Bishop Tuff; Tan, Alluvium; Pink, Basalt. Note map scale differs from Figure 1 and 2.

Stratigraphic investigations throughout the Mono Basin indicate that the explosive events of the North Mono and Inyo eruption sequences were accompanied by a series of strong earthquakes, most likely on the Hartley Springs Fault which runs from the southern-most end of the Mono Domes southward along the Inyo Domes, ending at Glass

Creek Flow (Fig. 4). The seismic events may have been triggered by dike emplacement near the fault (Bursik and others, 2003). Slipon the causes zones of low confinement stress, which allowed magma to be drawn up and erupt.

Two different hypotheses regarding the geometry of the Mono Domes can be found in the literature. (1) The Mono Domes are fed by a ring dike and erupted along the mylonitized border of a subcircular Cretacous pluton centered on Aeolian Buttes, which are composed of Bishiop Tuff and granitic rock (Kistler, 1966; Bailey and others, 1976; Bailey, 1982, 1989). (2) The Mono Domes formed along an extensional boundary of a pull-apart basin, defined by the north-northwest-striking faults of the Sierran range front in the Mono Basin that are oblique-slip faults with a right-lateral component (Bursik and Sieh, 1989). Hildreth (2004) suggested that the latter is more likely because the evidence for the mylonitic zone is poorly exposed in only three out crops along the pluton border.

PREVIOUS INVESTIGATIONS

Construction in the late 1930's and early 1940's of the Los Angeles water tunnel, known as the Mono Craters tunnel, provides detailed stratigraphic information along a transect across the Mono Basin. The West Portal of the tunnel is located 12.8 km southeast of the town of Lee Vining; the East Portal is about 18.2 km to the southeast near Aeolian Buttes (Fig. 4). Logs from several test holes and shafts drilled from the surface provide data for a simplified geologic profile along the tunnel transect (Gresswell, 1940; Jacques, 1940). Gresswell (1940) describes a wide fault zone beneath the axis of the Mono Domes encountered during the drilling of the water tunnel. In

addition to the tunnel, two geothermal wells were drilled on the shores of Mono Lake in 1971 (Axtell, 1972; see Fig. 1). Well "State PRC 4397.1" was drilled to an approximate depth of 1 km on the south shore and well "State PRC 4572.1" reached a depth of 0.7 km on the northwest shore of Mono Lake. Detailed lithologic logs are available for both wells (Fig. 5a and 5b). The temperature of the drilling mud for well "State PRC 4397.1" was continuously monitored and recorded. The average temperature of the returning mud was 29ºC at the surface and increased gradually to a maximum of 46ºC at the bottom of the well. Weathered basement was reached at a depth of approximately 0.5 km.

Interpretation of early gravity and seismic surveys suggests that the Mono Basin is a shallow structure resulting from regional warping and faulting with a depth of 1 - 1.5 km (Christensen and others, 1969) or 2-2.5 km (Pakiser, 1976). Christensen and others (1969) suggested that steep gravity gradients within Mono Basin are due to facies changes in the basin fill, faults buried within the basin, or density contrasts between lacustrine silts, marginal gravels and sands, and volcanic breccias. The deepest part of the basin is near the foot of the Sierra Nevada escarpment, towards the west. The density contrast between pre-Cenozoic metamorphic and granitic basement rocks is thought to be approximately 150 kg/m^3. Work by Pakiser (1976) indicates that a large gravity low (~50 mGal) covers the area of Mono Lake and reflects primarily low-density lacustrine sediments.

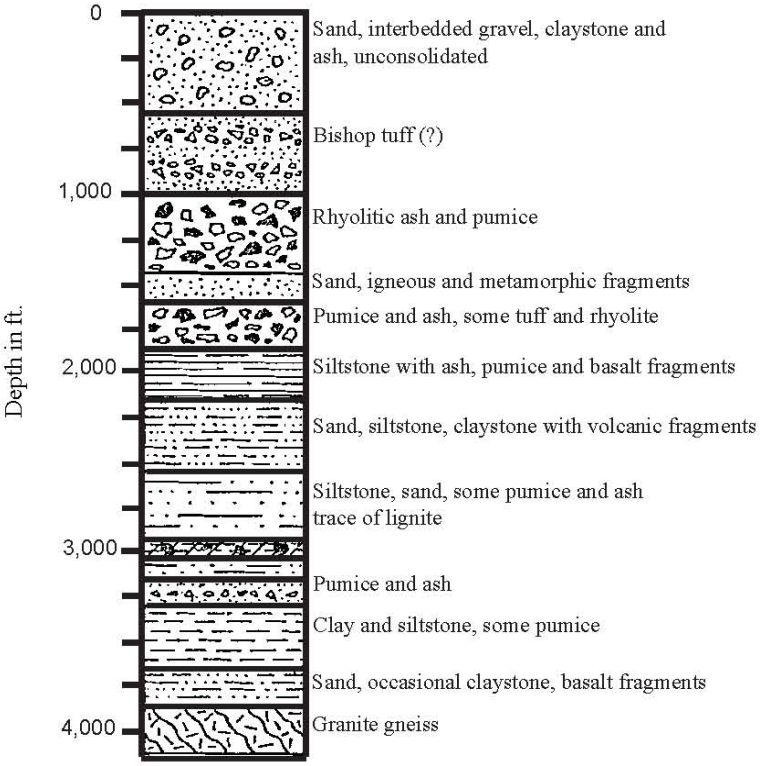

Figure 5a. Lithologic column of geothermal state well "State PRC 4397.1" modified from Axtell (1972). See Fig. 1 for location.

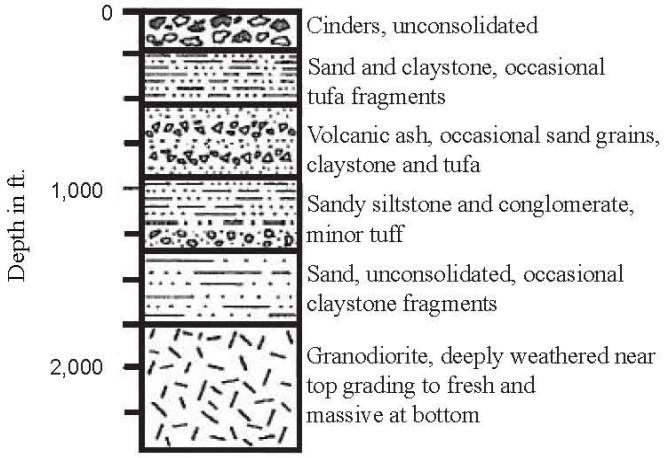

Figure 5b. Lithologic column of geothermal state well "State PRC 4572.1" modified from Axtell (1972). See Fig. 1 for location.

In an attempt to delineate the depth and geometry of a magmatic source for the Mono Domes, seismic and magnetotelluric studies were conducted. Hill and others (1985) performed a seismic refraction study which was used to: (1) evaluate the structure of the Mono-Inyo volcanic chain as a possible site for deep scientific drilling, (2) assess the possibility that a youthful magma chamber may exist in the upper crust beneath the chain, and (3) look for evidence of feeder dikes for the Mono Domes (Fig. 6a and 6b). Results from their work indicate that any large magma body would have to be at least 7 km beneath the surface. Hermance and others (1984) conducted a magnetotelluric study in Pumice Valley, adjacent to the Mono Domes. Their data did not indicate an observable decrease in resistivity at depths in the upper 10 km of crust beneath the valley, suggesting that the parent magma body feeding Mono Domes is either too thin or too deep (>10 km) to be resolved. However, an inversion of the travel-time residuals from 94 teleseismic events in 1986 revealed a 200-600 km^3 anomalous volume directly beneath the Mono Domes with at least 7% low velocity, and with a top 8 – 10 km deep (Achauer and others, 1986). This could be interpreted as a silicic melt or partial melt and in some measure may be controlled by the Sierran frontal fault zone (Achauer and others, 1986).

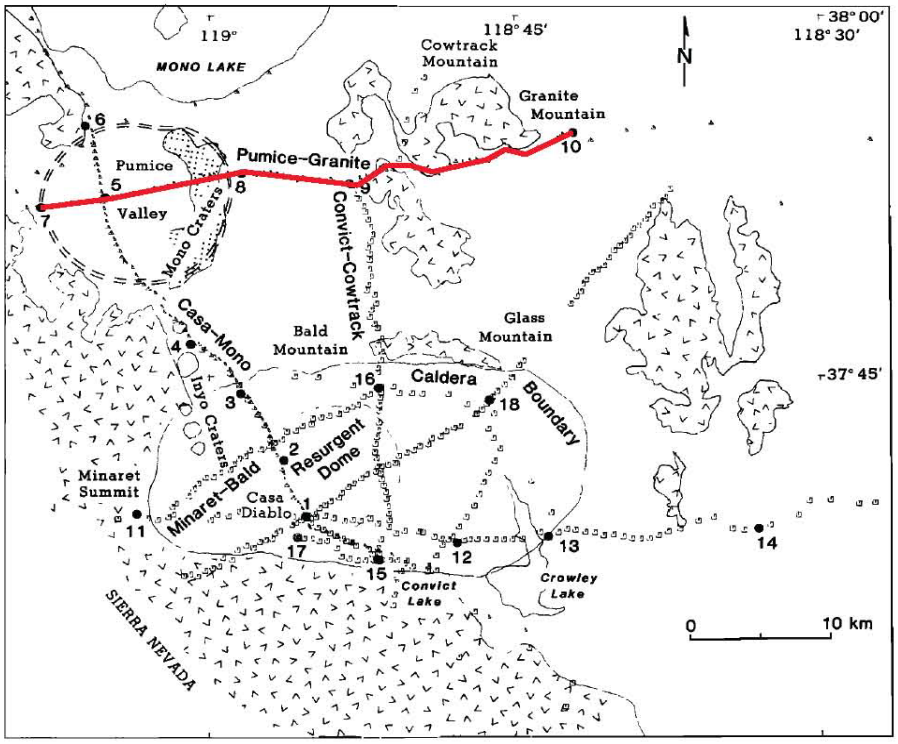

Figure 6a. Index map of seismic refraction surveys modified from Hill et al, (1985). Seismic refraction survey locations are indicated by open circles. The location of the seismic refraction survey referred to in this work is shown by the red line. The seismic model produced from this survey is shown below on Figure 6b.

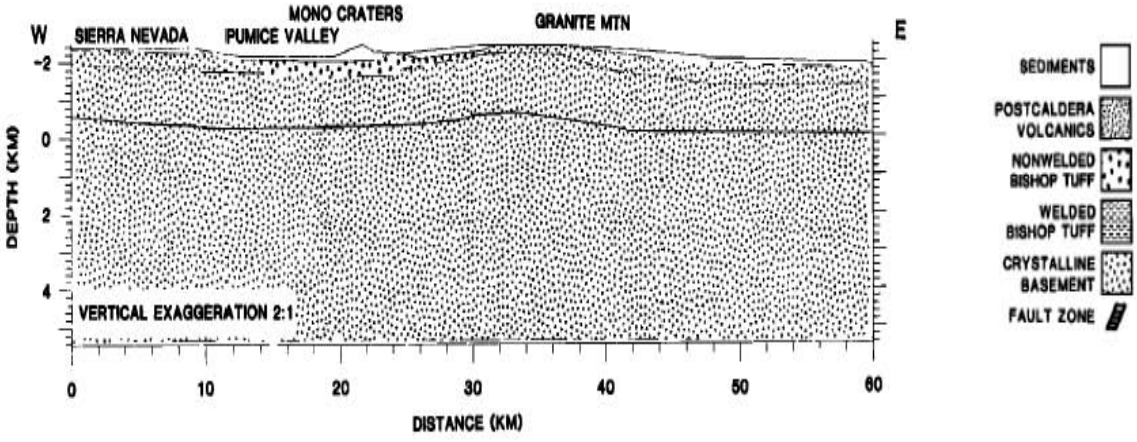

Figure 6b. Seismic refraction model from Hill et al. (1985) of the Pumice-Granite line.

Geologic studies of deformation and faulting along the Sierra Nevada front (Kistler, 1966) suggest a ring fracture is located on the border of a subcircular mylonitized Creatacous pluton. The ring fracture was mapped by tracing exposed mylonitic shear zones around a pluton of hornblende-bearing quartz monzonite near Grant Lake and extrapolating the trend to the south to join the southern arc of the Mono Domes. This trace was linked with a mapped normal fault of the Sierran frontal fault system to the north to complete the ring-fracture (Fig. 7).

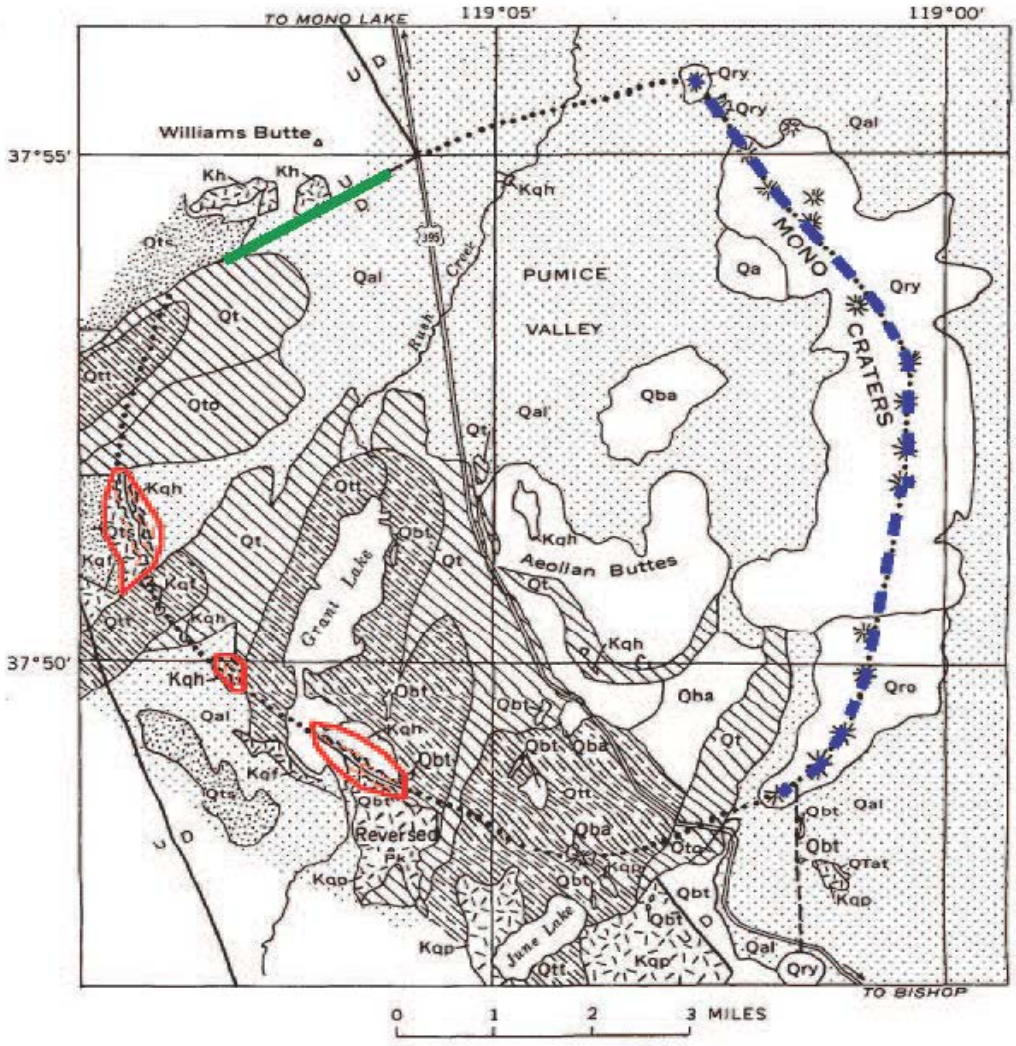

Figure 7. Modified geologic map from Kistler (1966). The ring fracture is shown by the dotted black line. Areas outlined in red show where mylonitic shear zones are exposed at the surface. The solid green line shows a mapped normal fault of sierra frontal fault system. The ring fracture was mapped by joining the axis of Mono Domes (or Mono Craters as labeled on map) with the exposed mylonitic zones and mapped normal fault south of Williams Butte.

GEOPHYSICAL DATA COLLECTION

Gravity Data

Previous gravity stations are within the Mono Basin, but most of the coverage is in and around the Long Valley Caldera. In order to improve the gravity coverage throughout the basin, additional gravity stations were collected in and around the Mono Domes. Approximately 320 gravity stations were collected in the Mono Basin during June and August of 2010 (Fig. 8). These include 51 closely spaced gravity stations at 400-800 m intervals along the seismic line occupied by Hill and others (1985). Additional gravity stations were collected at 800 m spacing along existing and unnamed roads within the Mono Basin. GPS data were collected at every gravity station using a handheld Trimble GeoXH, which provides vertical decimeter accuracy. A new gravity base station named LEEVIN was created at the Lee Vining Post Office (Appendix A). LEEVIN was tied to an existing high-precision gravity station located near Toms's Place, south of the Long Valley Caldera (MLEBQ1, Appendix A). LEEVIN was created to place a base station near the field operations to reduce time-dependent linear drift of the gravity meter. All gravity data are tied to the base station LEEVIN.

The LaCoste & Romberg gravity meter G614 and Scintrex gravity meter CG5A were used in this survey. Conversion of meter readings to gravity units for G614 and CG5A were made using factory calibration constants as well as a secondary calibration factor (1.00036 for G614 and 1.00630 for CG5A). These were determined by multiple gravity readings over the Mt. Hamilton calibration loop east of San Jose, California

(Barnes and others, 1969). Gravity data collected during the summer of 2010 were processed using standard gravity methods (e.g. Blakely, 1995) which are outlined in the geophysical data processing section.

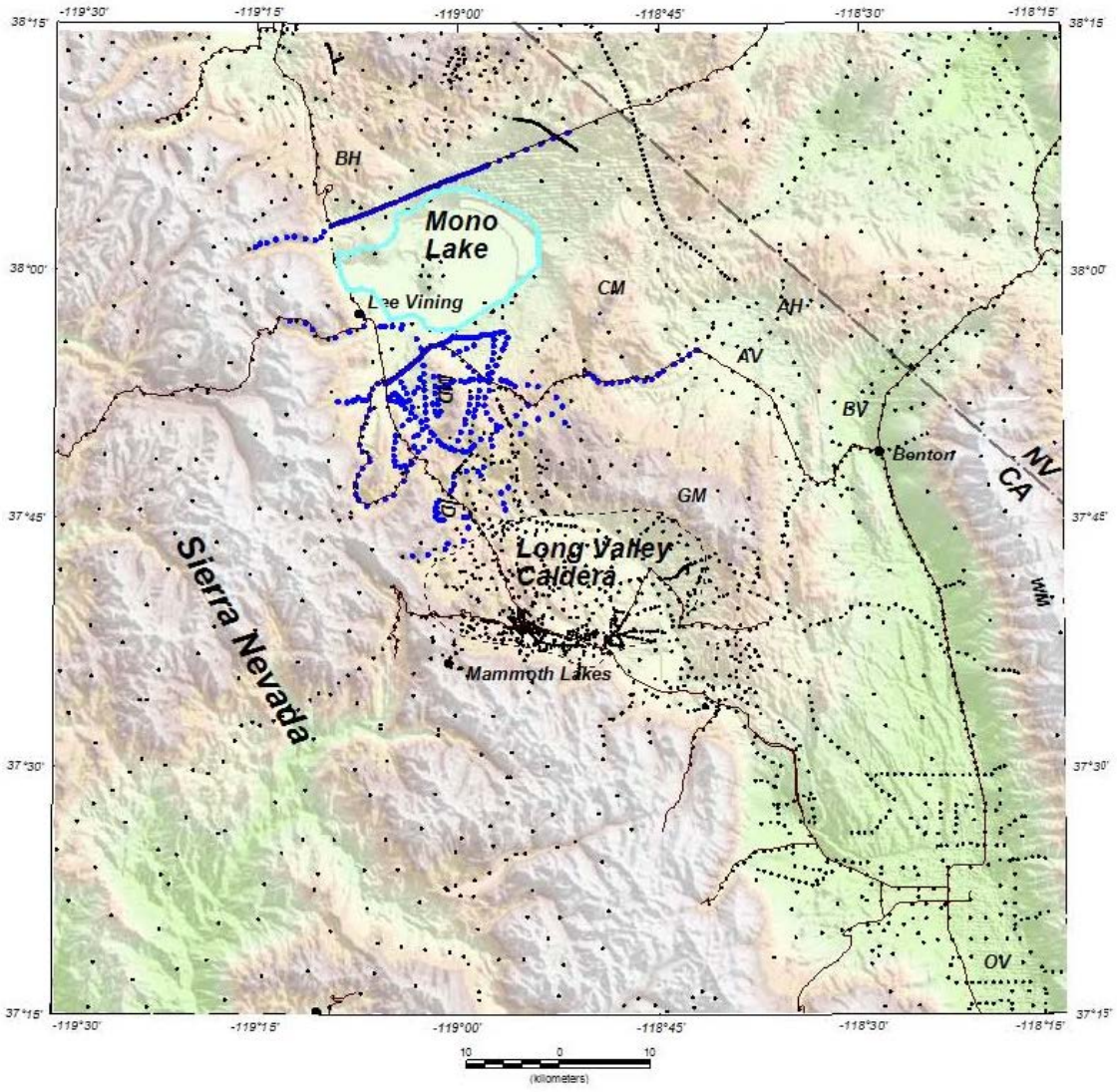

Figure 8. Map of gravity station locations throughout the Mono Basin study area. Blue dots show location of gravity stations collected during the summer of 2010. Black dots show locations of pre-existing gravity stations (Battaglia et al., 2003).

Magnetic Data

Aeromagnetic data used for this study are from a statewide compilation of California (Roberts and Jachens, 1999) and displayed as a color-contoured map (Table 1; Fig. 9 and 10). The regional aeromagnetic compilation consists of several surveys flown between 9,000 and 13,500 barometric elevation with flight lines oriented east-west and spaced 0.8 km to 1.6 km apart (Fig. 9). An International Geomagnetic Reference Field (IGRF), updated to the flight date of the individual surveys, was removed from each survey. Each survey was gridded at 1-km spacing and either upward or downward continued to a common datum of 305 m above the ground surface. A minimum curvature algorithm was used to grid each survey and grids were merged together into a final map.

Because the majority of the aeromagnetic data has poor resolution, additional ground magnetic data were necessary to better constrain magnetic anomalies throughout the basin, especially around the Mono Domes. Approximately 289 line-km of truck-towed magnetometer data were collected along numerous traverses throughout the Mono Basin (Fig. 11). Magnetic data were collected at one-second intervals using a Geometrics G858 cesium vapor magnetometer attached to an aluminum carriage. The carriage was connected to a vehicle by aluminum tubing and towed approximately 9 m behind the vehicle. The magnetometer was towed behind the vehicle to minimize any magnetic signal the vehicle may have, and it was positioned 2 m above ground surface. Truck-towed magnetic data were recorded and viewed in real-time using Geometrics MagLog software during field operations. The location of the magnetometer was recorded using a

Trimble nonmagnetic Ag132 GPS receiver mounted on the aluminum frame attached to the magnetometer. The Ag132 receiver has real-time differential correction capabilities using an Omnistar satellite system, resulting in submeter horizontal accuracy. Raw magnetic data were downloaded and processed using Geometrics MagMap 2000 software, where magnetometer and GPS data were merged.

Table 1. Aeromagnetic survey specification. See Figure 9 for survey boundaries. Numbers in parentheses are index numbers from the references publication (Roberts and Jachens, 1999). D, drape (above ground); B, barometric elevation

Index ID	Name	Date Flown	Flight line (mi)	Flight Dir.	Altitude (ft)
A (3134)	Hoover-Walker Lake	1978	0.5-1.	E-W	1,000 D
B (3002C)	Western Nevada – Aurora	1967	1	E-W	11,000 B
C (4233)	Bodie-Aurora	1999	0.093	N-S	500 D
D (4253)	Excelsior Mountains	2000-2001	0.155	N-S	820 D
E (3002A)	Western Nevada	1967	1	E-W	9000 B
F (4010)	Tioga Lake	1980	0.5	NE-SW	1,000 D
G (4058B)	White & Inyo Mountains B	1981	0.5	E-W	8,000 B
H (3027)	Eastern California	1973	1	E-W	13,500 B
I (0242)	Long Valley ‘56	1956	1	E-W	9,000 B
J (4058A)	White & Inyo Mountains A	1981	0.5	E-W	14,500 B
K (3135)	Devils Postpile	1978	0.5	E-W	1,000 D
L	Mariposa	1979	3	E-W	400 D
M (4058C)	White & Inyo Mountains C	1981	0.5	E-W	7,000 B

.

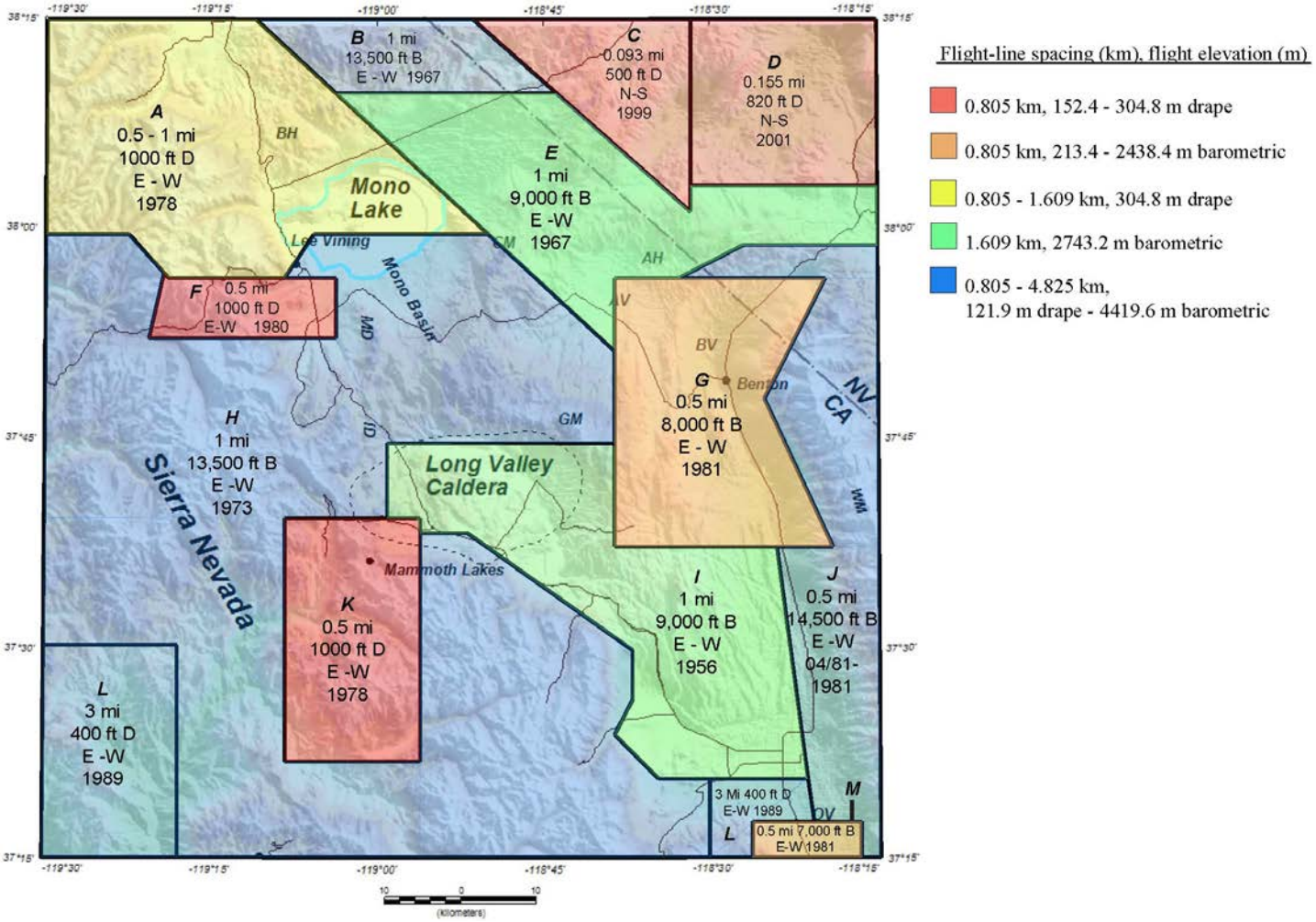

Figure 9. Aeromagnetic survey flight-line specifications, B, barometric; D, drape.

.

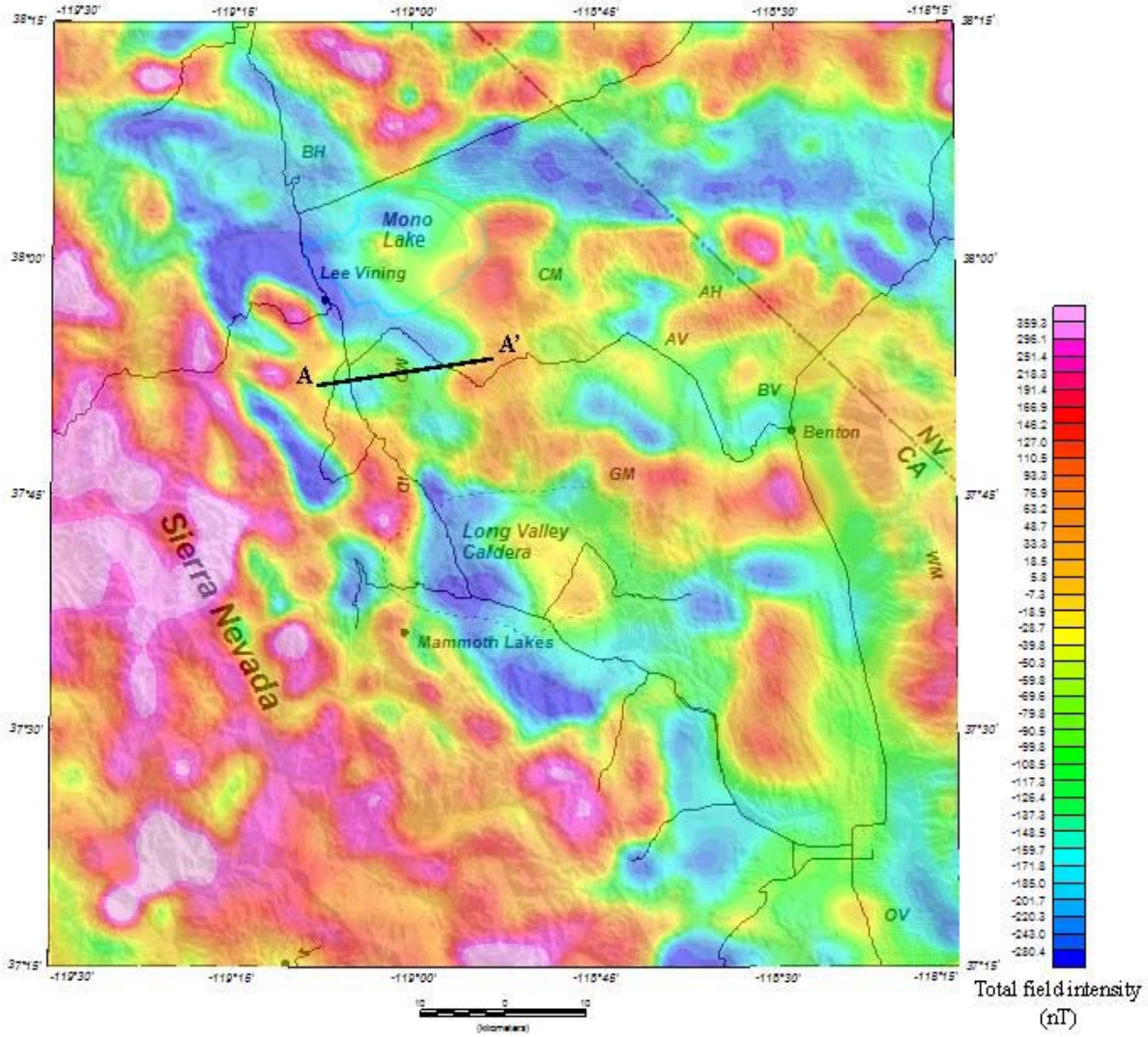

Figure 10. Regional aeromagnetic anomaly map of the Mono Basin study area. Black line shows location of profile A-A'.

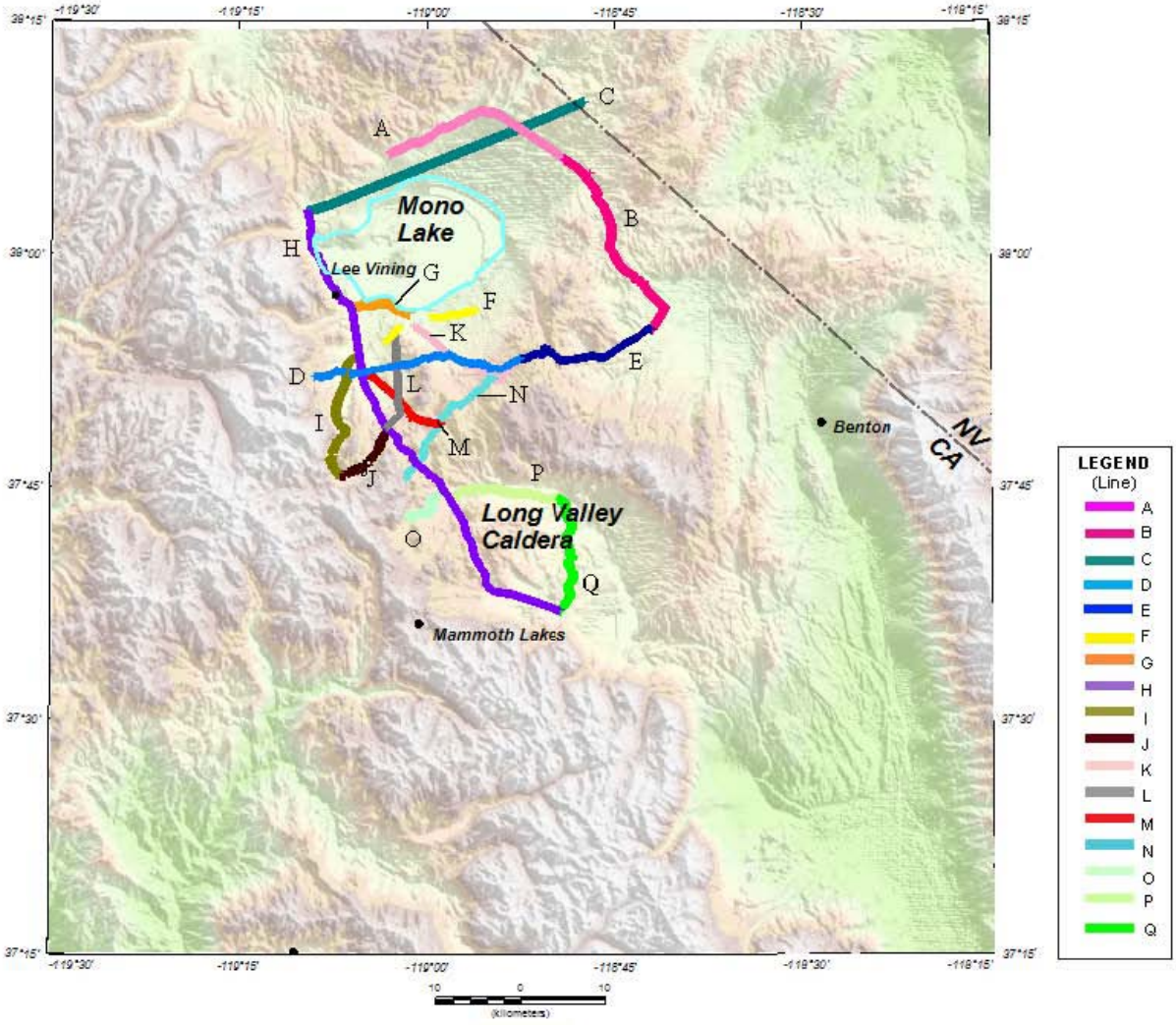

Figure 11. Location of truck-towed magnetometer and ground magnetic (Line D) traverses.

Approximately 8 line-km of ground magnetic data were collected along a traverse across the Mono Domes (Fig. 11, Line D). This traverse was collected using a Geometrics G858 cesium vapor magnetometer with the same survey and GPS specifications as the truck-

towed magnetometer surveys. The magnetometer height above the ground surface was approximately 2 m.

A portable Geometrics G856 proton-precession base-station magnetometer was used to record diurnal variations of the Earth's magnetic field during the truck-towed and ground magnetic surveys. The diurnal variations are known to be larger in the summer than in winter and the amplitudes can span tens of nanoteslas. These variations are believed to be caused by electric currents induced in the Earth from electric currents in the ionosphere which are in turn driven by solar activity.

Physical Property Data

Rock samples were collected throughout the study area to measure density and magnetic susceptibility. This information is necessary for geophysical modeling to constrain the physical properties of geologic units used. Rock samples were collected at newly acquired gravity stations when a rock outcrop was nearby and at other locations throughout the basin (Fig. 12). Densities and magnetic susceptibilities were averaged by rock type (Table 2). Physical properties of individual rock samples collected in the field are presented in Appendix B. Densities were measured using the buoyancy method with an electronic balance, and a Kappameter® KT-5 was used to measure magnetic susceptibility. Grain, saturated-bulk, and dry-bulk densities were calculated for each sample by weighing the sample in air *(Wa)*, saturated and submerged in water *(Ww)*, and weighed in air and saturated (*Was)* using the following formulas (all weights are measured in grams):

$$\text{Grain density} = 1{,}000 \text{ kg/m}^3 * Wa/(Wa-Ww),$$

Saturated-bulk density = 1,000 kg/m³ * *Was/(Was-Ww)*, (1)

Dry-bulk density = 1,000 kg/m³ * *Wa/(Was-Ww)*

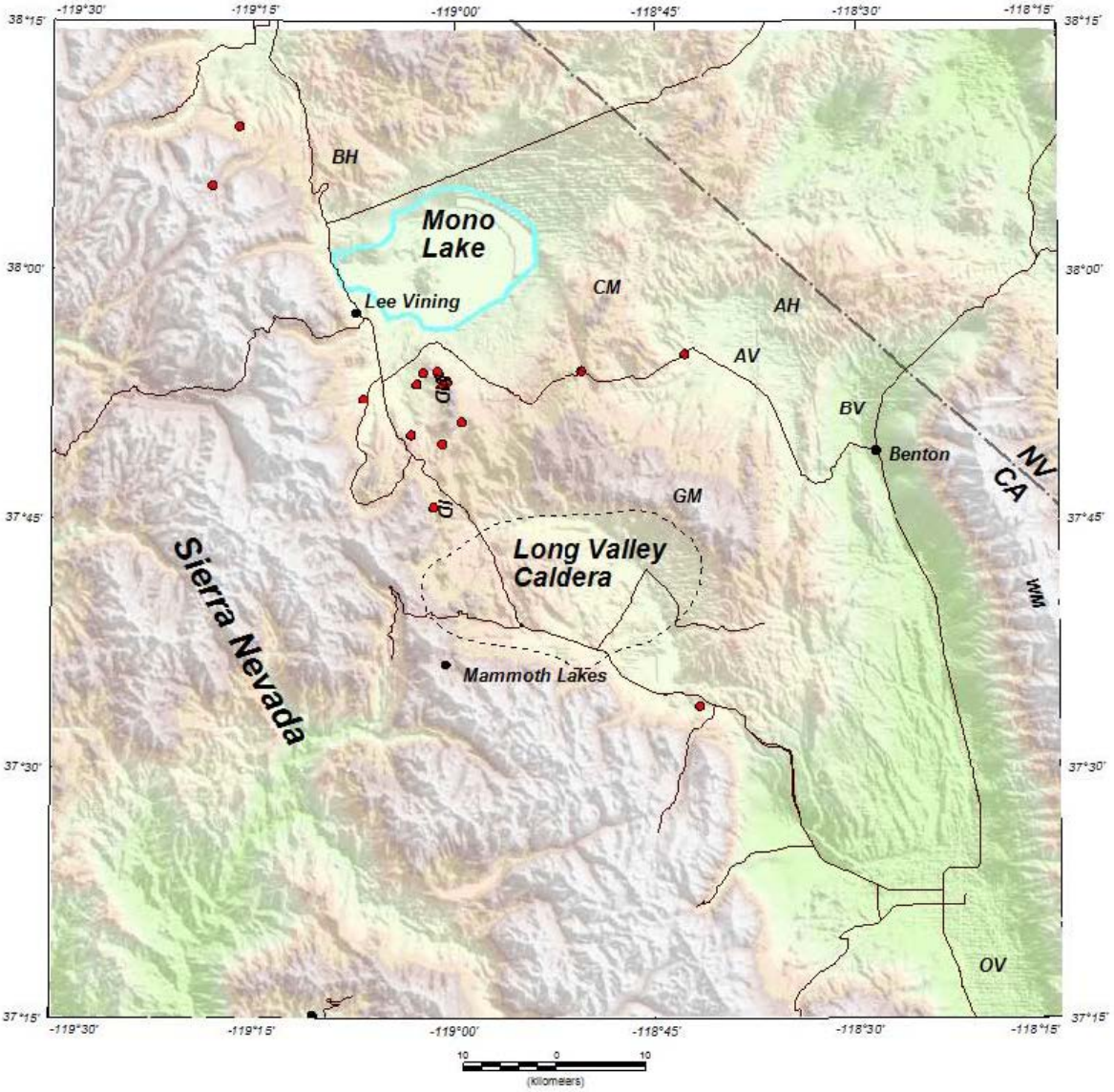

Figure 12. Location map of rock samples collected in 2010.

Table 2. Physical property measurements of selected rock types collected in 2010. GD, grain density; SBD, saturated bulk density; DBD, dry bulk density; Susc, magnetic susceptibility

Rock Type	No. of samples	GD (kg/m^3)	SBD (kg/m^3)	DBD (kg/m^3)	Susc. (10^{-3} SI)
Basalt	5	2557	2441	2363	13.476
Granite	8	2672	2615	2581	5.541
Granodiorite	3	2684	1983	2629	13.207
Metasediment	1	2675	2651	2636	0.03
Obsidian	9	2018	199	1975	0.779
Rhyolite	16	1872	1813	173	1.624
BishopTuff	6	1935	1687	1419	2.458

GEOPHYSICAL DATA PROCESSING

Gravity Methods

A new color-contoured, isostatic gravity anomaly map of the study area was produced using over 2,700 stations (Fig. 13). This dataset includes the gravity stations collected during the 2010 summer field season and an existing gravity dataset (Battaglia et al., 2003). The isostatic gravity anomaly map shows lateral variation in the density of subsurface rocks. Gravity values are given in milligals (mGal), a unit of acceleration or gravitational force equal to 10^{-5} m/s^2. Observed gravity readings were referenced to the International Gravity Standardization Net 1971 (IGSN 71) gravity datum (Morelli, 1974).

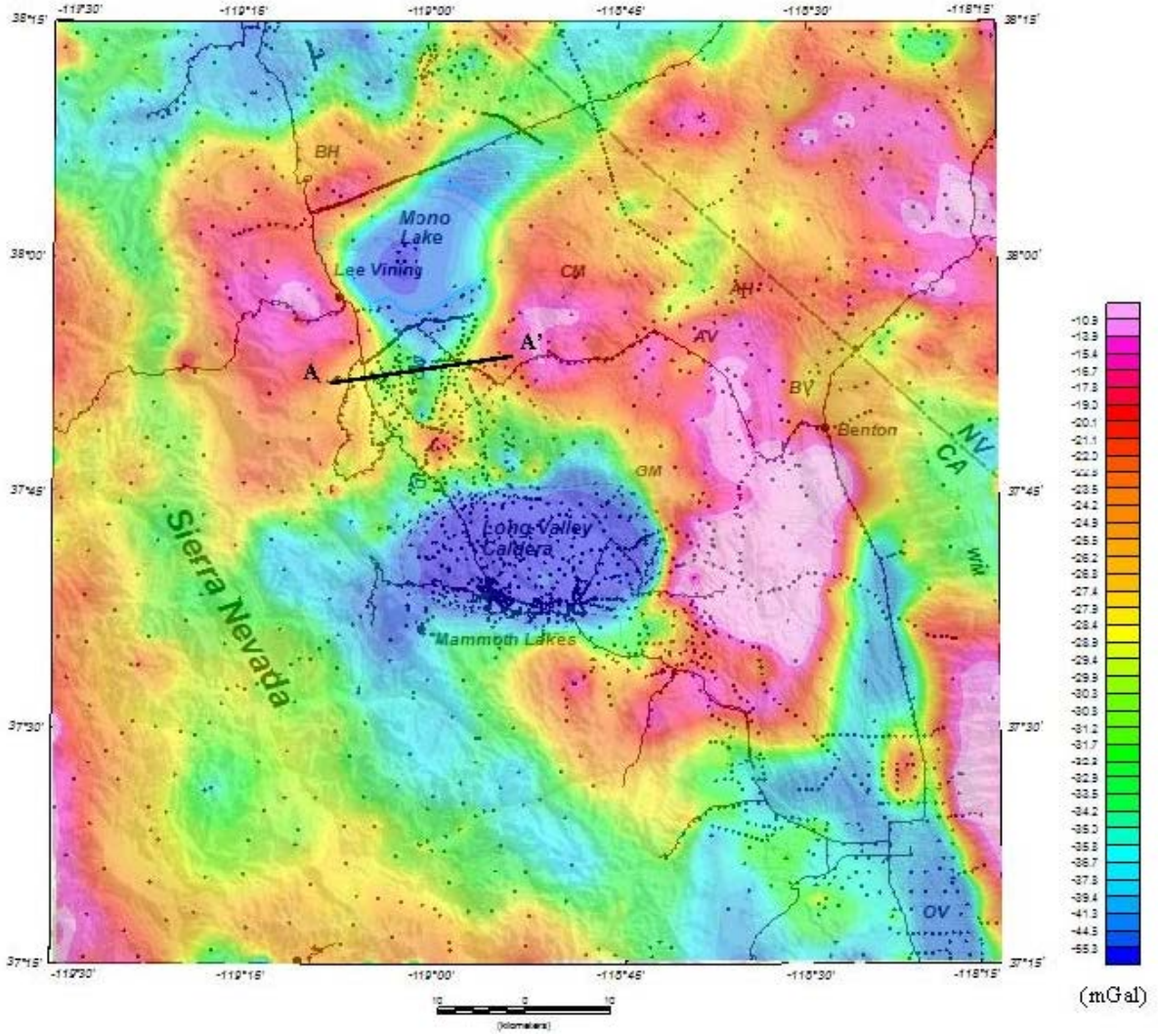

Figure 13. Isostatic gravity anomaly map of the Mono Basin study area. Grey dots represent gravity station locations. The black line shows the location of profile A-A'.

The following corrections were applied to the 2010 gravity data before they were merged in to the existing gravity dataset. Gravity data from 2010 is presented in Appendix C.

The *instrument-drift correction* accounts for the changes in the gravimeter spring over time or due to temperature changes. The instrument drift is addressed by re-occupying a

gravity base station at the beginning and end of each day and applying a linear time-dependent drift correction to all other measurements.

The *earth-tide correction* accounts for the gravitational pull of the moon and sun, which are dependent upon time and latitude. Although these effects are small, they are significant enough to be detected by a gravimeter. The change in gravity due to this phenomenon does not exceed 0.3 mGal.

The *latitude correction* removes the variation in the Earth's gravity with latitude, which is caused by the centrifugal force of the rotation of the earth along with the resulting bulge at the equator. This correction is accounted for in the theoretical gravity equation.

Theoretical gravity at sea level is given by the equation

$$g_t = (978{,}031.85)\ (1+0.005278895 \sin^2 \phi + 0.000023462 \sin^4 \phi \text{ mGal} \qquad (2)$$

where ϕ is latitude in degrees.

The *free-air correction* is applied to remove the variation in gravity due to changes in the gravity station's elevation relative to sea level. The free-air correction does not include the gravitational effect of the material between the station and sea level. The free-air correction was calculated using Swick's (1942) formula:

$$\text{fac} = h(0.30877 + \sigma\ (-0.0013398 + \sigma\ (-0.0005329 + \sigma\ (0.0000911)))$$

$$- h(0.072 \times 10^{-6}), \qquad (3)$$

where $\sigma = 0.0001\phi^2$ and *h* is the elevation of the station in meters and is positive if above sea level.

The *free-air anomaly* is the difference between the observed gravity and the theoretical gravity at the elevation and latitude of the measurement. The free-air anomaly was calculated using the Geodetic Reference System 1967 formula for theoretical gravity on the ellipsoid (International Union of Geodesy and Geophysics, 1971) and is given by the equation:

$$faa = (g_o - g_t) + fac \quad (4)$$

where g_o is the observed gravity.

The *Bouguer correctio*n corrects for the excess mass between the station and sea level. In our case, we assumes the material between sea level and the gravity station is an infinite slab of uniform density of 2670 kg/m³. The Bouguer correction equation is given by:

$$bc = -0.111897\ h \quad (5)$$

where h is the elevation of station in meters and is postive if above sea level.

The *terrain correction* removes the gravitational effect of topography to a radial distance of 167 km around the gravity station and was computed using both manual and digital methods. Three types of terrain corrections were applied: innermost or field terrain, innerzone-terrain, and outerzone-terrain. The innermost-terrain corrections were estimated in the field and extend from the station to a radial distance of 68 m, equivalent to Hayford and Bowie's (1912) zone B. Inner zone-terrain corrections were estimated from Digital

Elevation Models (DEMs) with 10 or 30-m resolutions derived from USGS 7.5' topographic maps and extend from 68 m to a radial distance of 2 km (D. Plouff, USGS, unpub. software, 2010). Outerzone-terrain corrections, from 2 km to a radial distance of 167 km, were computed using a DEM derived from USGS 1:250,000-scale topographic maps using an automated procedure based on geographic coordinates (Plouff, 1966; Plouff, 1977; Godson and Plouff, 1988). Digital-terrain corrections were calculated by computing the gravity effect of each grid cell in the DEM using the distance and difference in elevation of each grid cell from the gravity station.

The *curvature correction* accounts for the effect of the Earth's curvature. The curvature correction was calculated using the following equation (Plouff, 1977):

$$cc = h(0.001464 + h(4.5\times 10^{-14} - 3.533 \times 10^{-7})) \quad (6)$$

where h is the elevation in meters and is positive if above sea level.

The *complete Bouguer anomaly* combines the free-air anomaly, bouguer, terrain, and curvature corrections and is given by the equation:

$$cba = faa + bc + tc - cc \quad (7)$$

where tc is the terrain correction.

The *isostatic correction* removes long-wavelength differences in the gravity field related to the compensation of topographic loads. A regional isostatic gravity field was removed from the complete Bouguer anomaly assuming an Airy-Heiskanen model for isostatic compensation of topographic loads (Jachens and Roberts, 1981) with an assumed

sea-level crustal thickness of 25 km, a crustal density of 2,670 kg/m^3, and a density contrast across the base of the crust of 400 kg/m^3.

Magnetic Methods

Diurnal variations recorded by the base-station magnetometer were removed from the truck-towed and ground magnetic datasets. Both datasets were filtered using a low pass filter to remove anomalous high and low spikes caused by cultural "noise," such as passing cars, culverts, fences, and powerlines. The cut-off for the low-pass filter ranged from 10 to 50 wavelengths. A new magnetic anomaly profile map of the study area was produced using the filtered truck-towed and ground magnetic data (Fig. 14). Truck-towed magnetic datasets are presented in Appendix D.

Reduction-To-The-Magnetic Pole

Magnetic anomalies are frequently laterally shifted from their sources and may have distorted, irregular shapes because of the direction of magnetization rarely in the direction of the Earth's magnetic field. A reduction-to-the-magnetic-pole (RTP) filter changes the Earth's magnetic field inclination to 90˚, as if it were at the magnetic pole; results are shown on the resulting map (Fig.15).

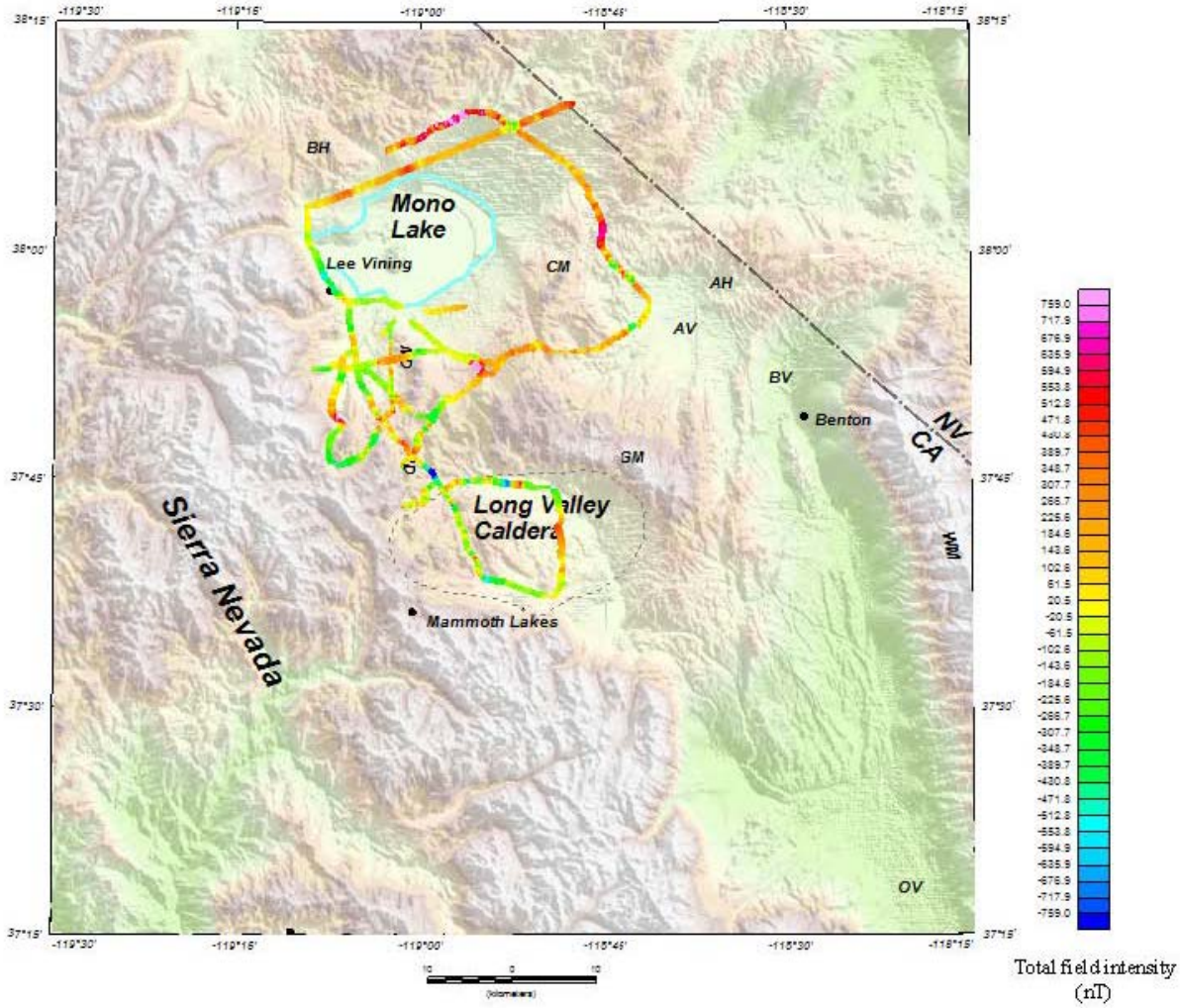

Figure 14. Truck-towed and ground magnetic anomaly map. See Figure 11 for location of truck-towed and ground magnetic surveys.

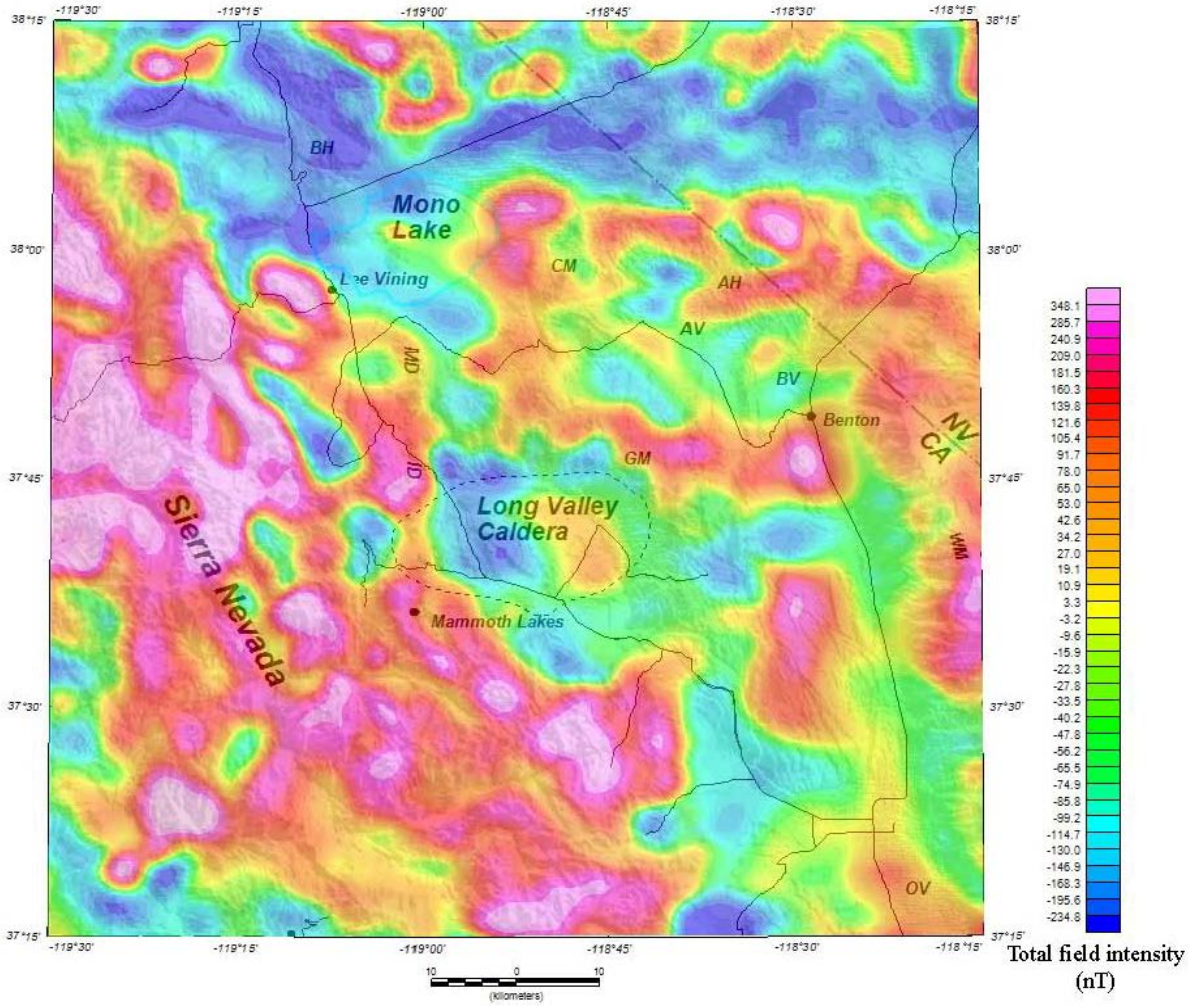

Figure 15. Reduction-to-the-magnetic pole map of the Mono Basin study area.

This procedure aids in the interpretation by creating symmetrical magnetic anomalies that are essentially centered over their sources. This transformation simplifies magnetic anomaly maps and is a fairly easy transformation at high magnetic latitudes (Telford and others, 2004).

Magnetic-Potential

A directional derivative links the gravity and magnetic potentials that are caused by a homogeneously dense and magnetized body, allowing the total magnetic field to be transformed into a corresponding gravity field. A magnetic potential map (Fig. 16) is produced by converting the magnetic anomalies to gravity anomalies using Poisson's relation, assuming magnetic and gravity anomalies are created by the same source.

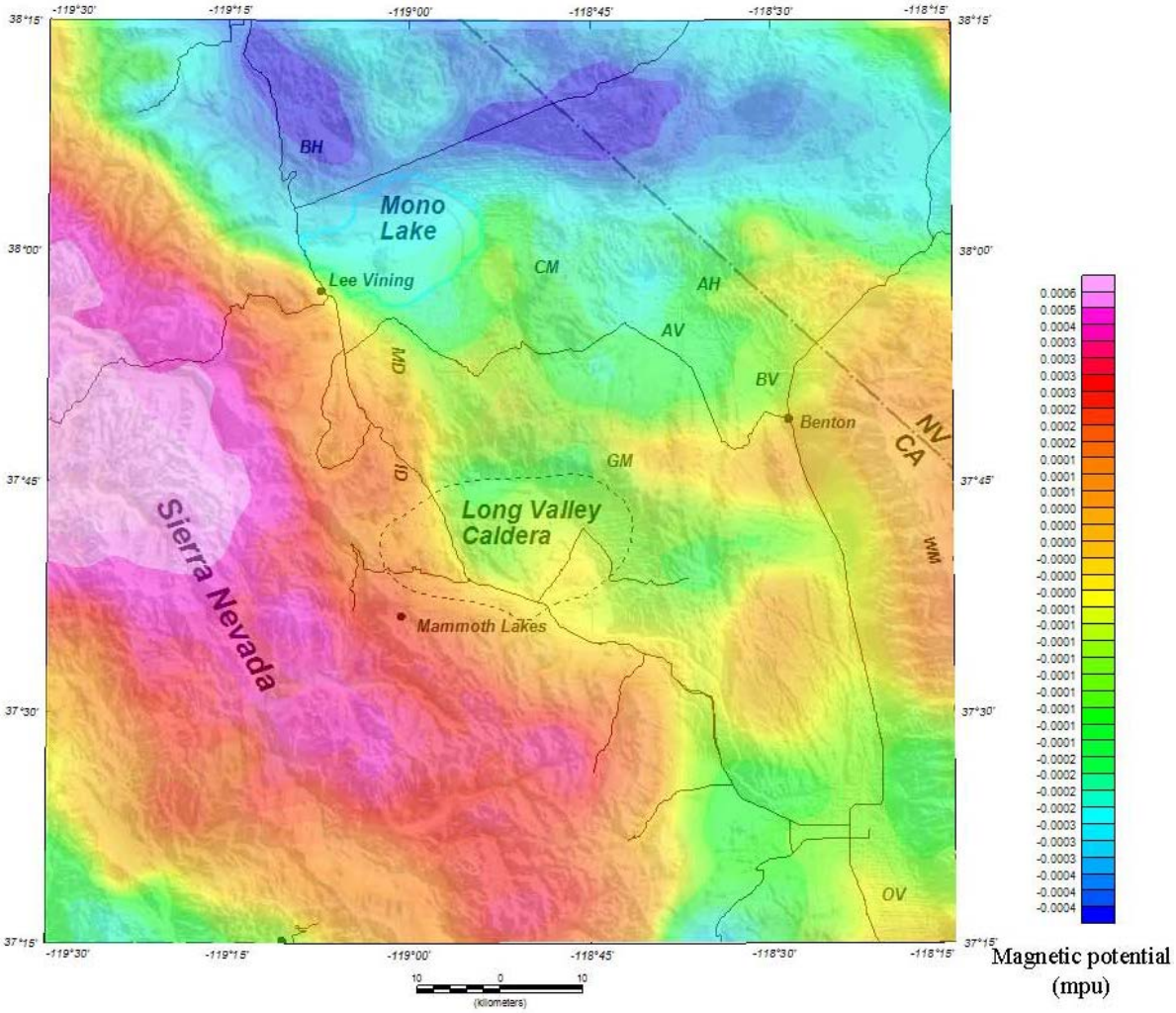

Figure 16. Magnetic potential map of the Mono Basin study area derived from the transformation of magnetic anomalies. mpu, magnetic potential units (dimensionally amperes).

The ratio between density and magnetization is kept constant. For this work the ratio is a density contrast of 0.10 g/cm^3 to a magnetization contrast of 0.001 cgs units. Magnetic potential transformations are helpful for simplifying the interpretation of magnetic anomalies because magnetic anomalies are more complex than gravity anomalies. Gravity anomalies often have the steepest horizontal gradient roughly over the edges of the causative source. This property can be utilized in magnetic interpretation by transforming the magnetic anomaly to a magnetic potential anomaly and locating the steepest horizontal gradients (Blakely, 1995).

Maximum horizontal gradients

Maximum horizontal gradients were calculated for gravity and magnetic data to help delineate the edges of potential-field sources. A procedure described by Blakely and Simpson (1986) was used to calculate the maximum horizontal gradients. Maximum horizontal gradients indicate abrupt lateral changes in the density or magnetization of subsurface rocks. Maximum horizontal gradients calculated for the isostatic gravity and magnetic-potential map and are shown on respective maps (Figs. 17 and 18).

Residual anomaly

The residual anomaly map displays the magnetic anomalies produced by shallow, short-wavelength magnetic sources and removes the effect of the deeper, longer-wavelength anomalies (Fig.19). To produce the residual anomaly map, an upward continuation of the data must be performed. The upward continuation transformation is a filtering process that reduces the intensity of anomalies produced by near-surface sources and enhances the

anomalies caused by long wavelength, deep sources. An upward continuation filter at a depth of 1 km was applied to the aeromagnetic anomaly map. The upward continued data was then subtracted from the original aeromagnetic data to produce a residual, or shallow magnetic, anomaly map (Fig. 19).

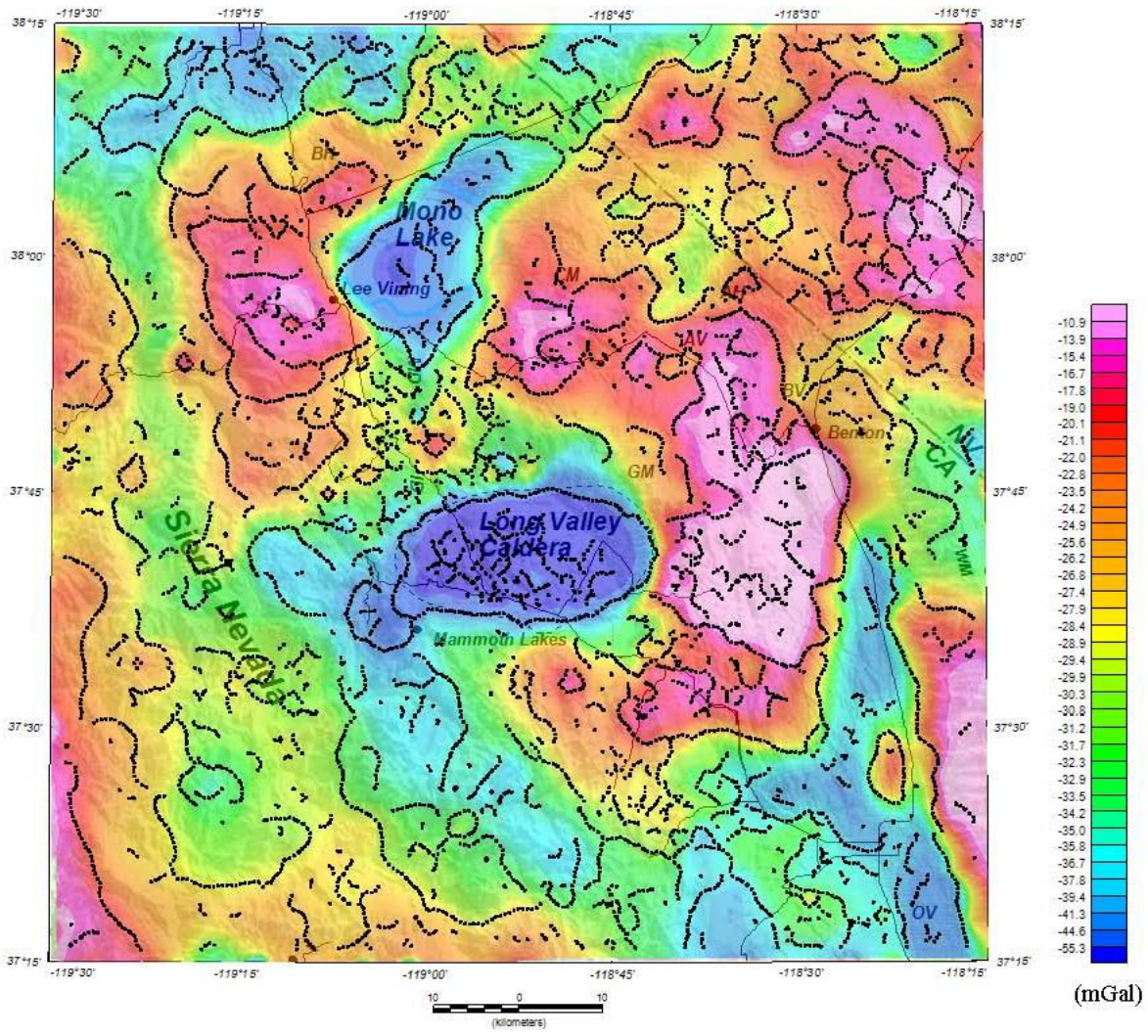

Figure 17. Isostatic gravity anaomaly map of the Mono Basin study area. Black dots represent maximum horizontal gradients derived from the isostatic gravity data.

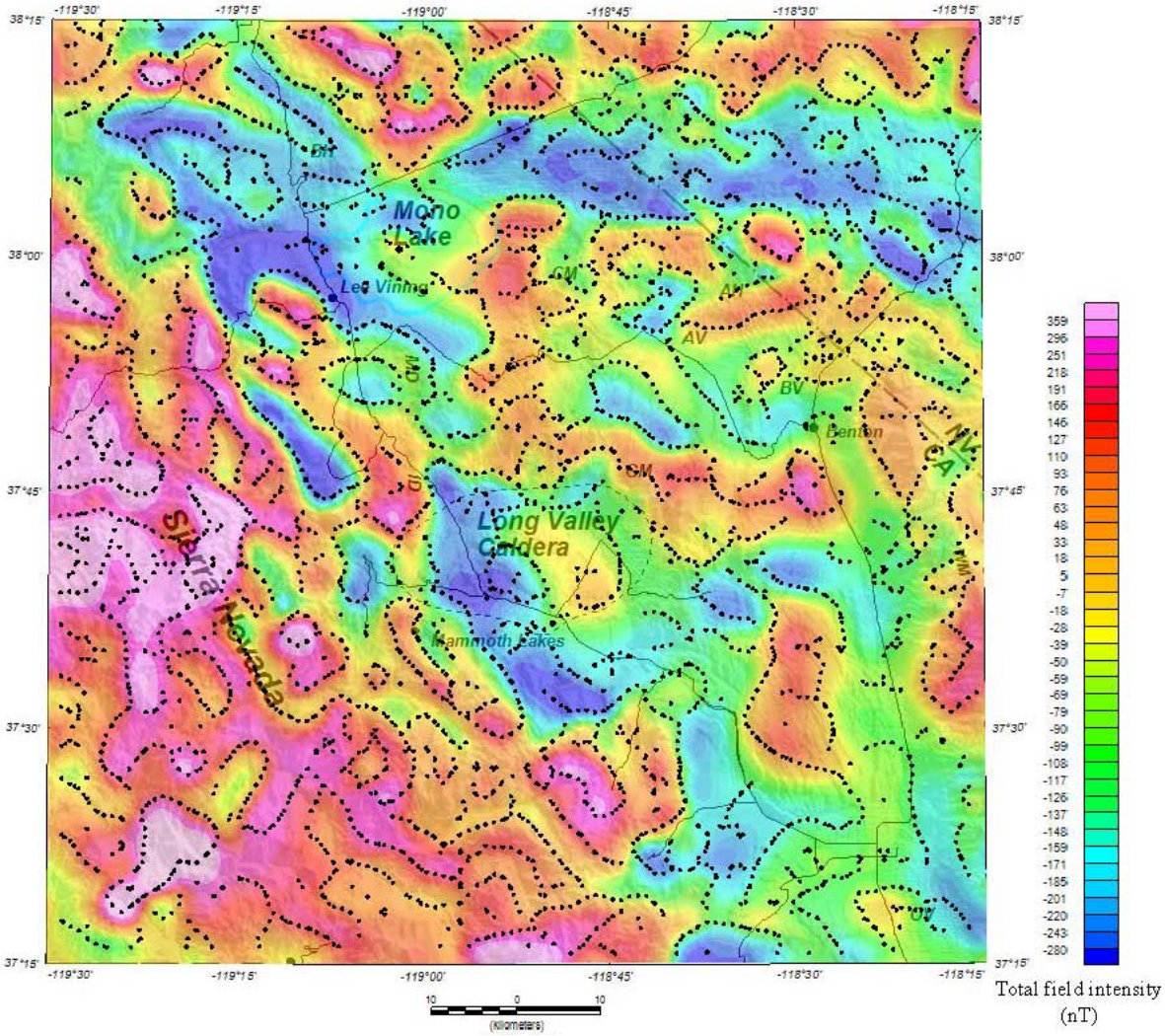

Figure 18. Aeromagnetic anomaly map of the Mono Basin study area. Black dots show maximum horizontal gradients derived from the magnetic potential data.

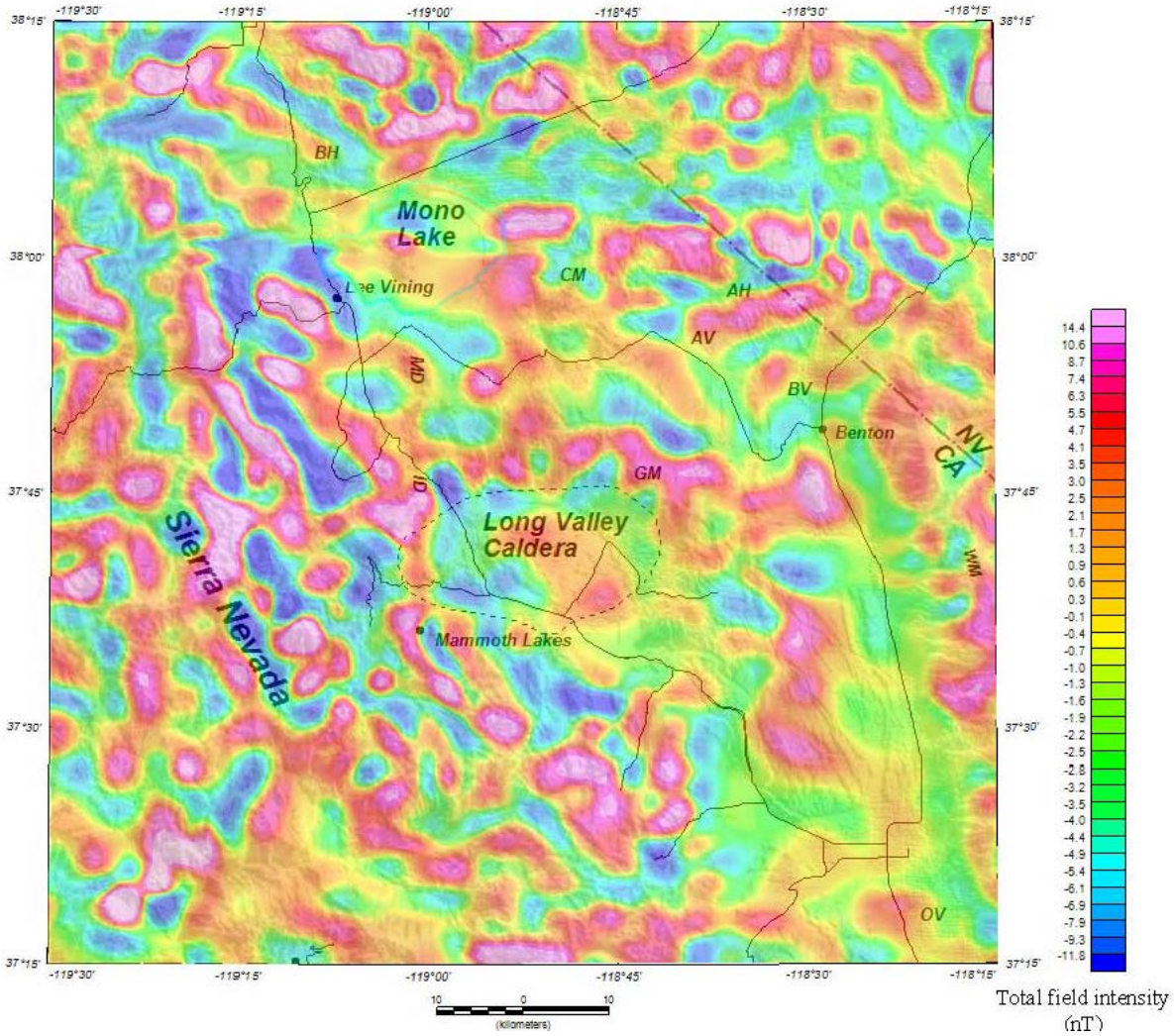

Figure 19. Residual, or shallow, magnetic map of the aeromagnetic data emphasizing anomalies in the upper 100m of the crust.

MODELING

We produced two geophysical forward models from gravity and aeromagnetic data taken along an east-west profile across the northern end of the Mono Domes (Profile A-A' is displayed on Figures 2, 10, and 13). An interactive gravity and magnetic modeling program, GM-SYS, was used to create geologic models of the subsurface (Fig. 20 and 21). Gravity and magnetic models are non-unique and many models can be constructed to fit the given dataset. Additional independent information is needed to help constrain the geophysical models.

Velocity data are used as a reference to constrain the depth and geometry of the basin along with the densities used in the model. The seismic velocity model shows layers of contrasting density within the basin and suggests the depth of the basin to be roughly 600 m (Hill and others, 1985). Seismic velocities taken from the seismic refraction survey co-located with our gravity and magnetic forward model are converted to densities using the formula

$$\rho = 1740v^{1/4} \qquad (8)$$

where ρ is density in kg/m³ and v is the velocity in km/s (Gardner et al., 1974; Table 3). The velocity data were used to constrain the depth and geometry of the basin and the densities used in the model.

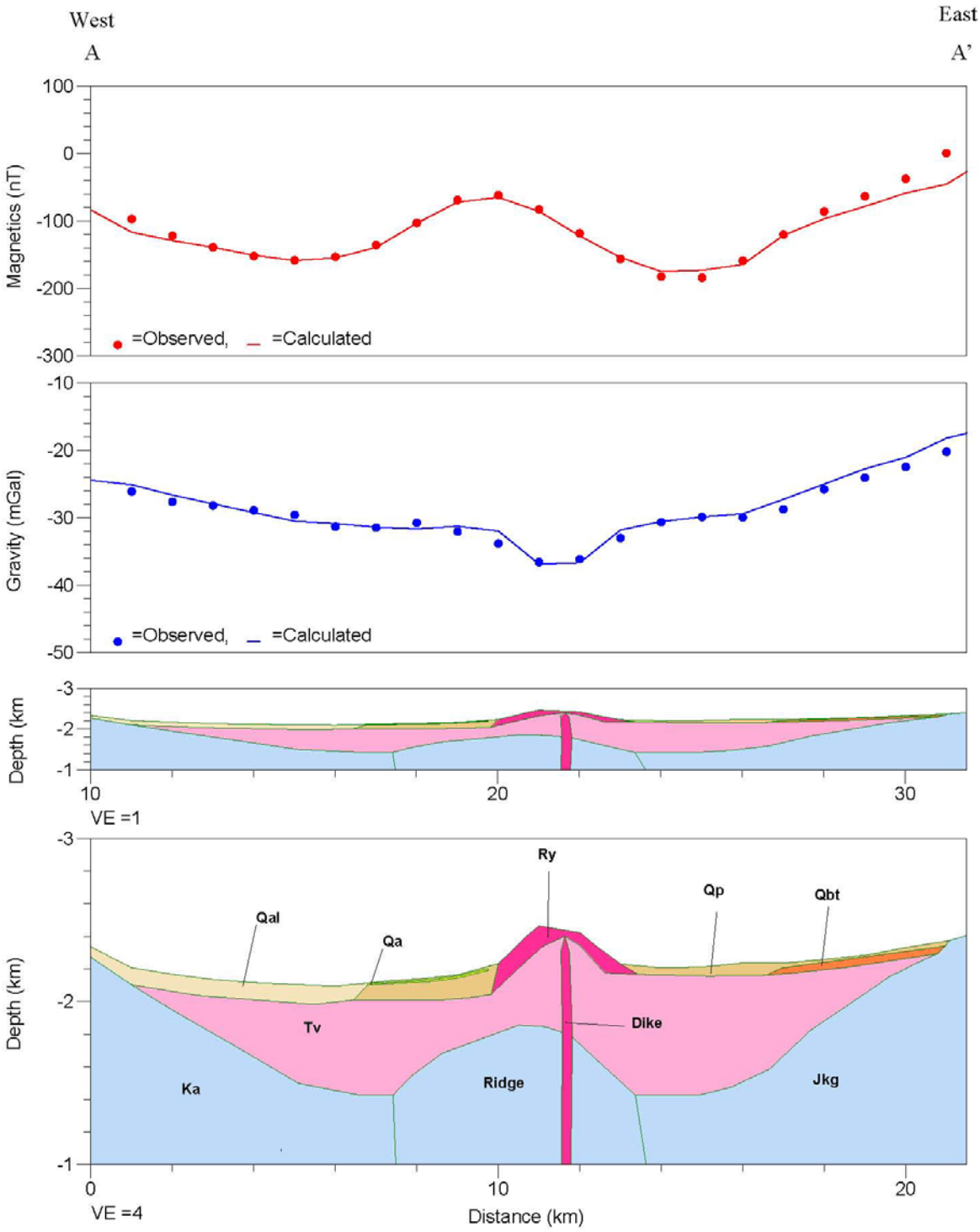

Figure 20. Model A, showing a subsurface basement ridge. Qal, alluvium; Qa, andesite; Qp, rhyolitic pumice and ash; Ry, rhyolite; Qbt, Bishop Tuff; Tv, volcanic basin fill; Ka (western basement block), quartz monzonite of Aeolian Buttes; Jkg (eastern basement block), granodiorite, diorite and gabbroic rocks. See Table 4 for model parameters.

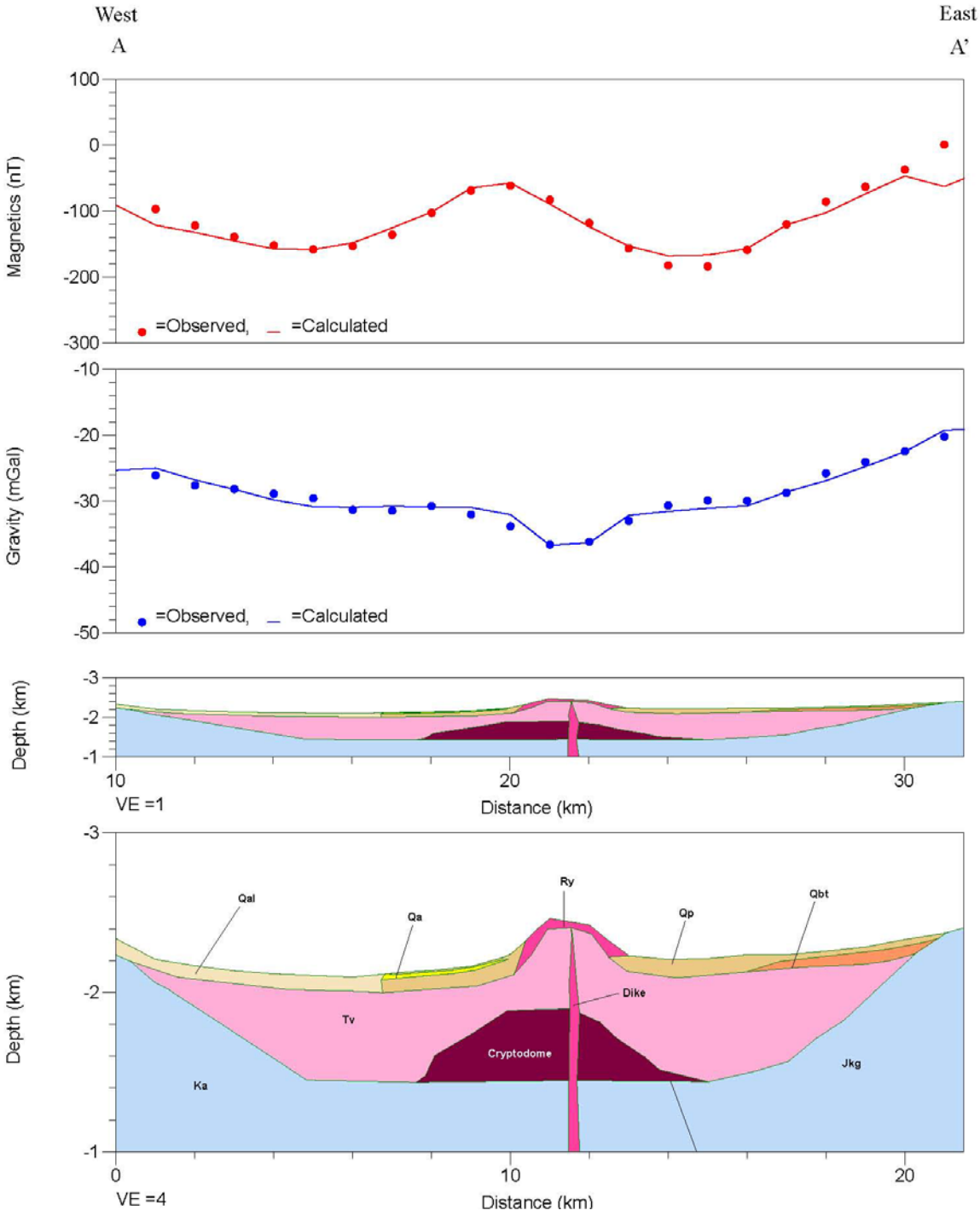

Figure 21. Model B, showing a cryptodome most likely containing basaltic materials. Qal, alluvium; Qa, andesite; Qp, rhyolitic pumice and ash; Ry, rhyolite; Qbt, Bishop Tuff; Tv, volcanic basin fill; Ka (western basement block), quartz monzonite of Aeolian Buttes; Jkg (eastern basement block), granodiorite, diorite and gabbroic rocks. See Table 4 for model parameters.

Table 3. Velocity-to-density conversions using Gardner et al. (1978).

Velocity (km/s)	Density (kg/m^3)
1200	1820
1250	1840
1300	1860
1500	1920
2900	2270
3000	2290
3500	2380
3600	2400
3900	2450
4000	2460
4100	2480
4900	2590
5500	2670
5600	2680
5750	2700

Surface geology used to constrain shallow densities in the model, consists of Bishop Tuff, andesite, alluvium, rhyolite, and rhyolitic pumice and ash outcrops (Bailey, 1989). The

basin fill consists of a mixture of rhyolite, andesite and basalt, flows, tuff, fragments, ash, and pumice inter-bedded with lacustrine sediments, based on units encountered in the Mono Craters tunnel drilling project and from geothermal wells drilled on the shores of Mono Lake (Gresswell, 1940; Axtell, 1972). A ~ 60-m thick layer of Bishop Tuff is presumed to be located on the eastern boundary of the basin and is overlain by a thin layer of rhyolitic pumice and ash, as suggested by two outcrops (Bailey, 1989). A rhyolitic feeder dike probably serves as the conduit for the dome (Bailey, 1989).

Our two geophysical models (Figs. 20 and 21) have a crystalline basement composed of a standard crustal density of 2670 kg/m^3 down to a depth of 1.3 -1.5 km. The composition of crystalline basement in the model varied from west to east and was determined from geologic maps (Kistler, 1966; Bailey 1989). The west side of the basement including the basement ridge is assumed to be the same quartz monzonite of Aeolian Buttes, as suggested by a geologic cross section south of the profile line (Kistler,1966). The magnetic susceptibility of the quartz monzonite unit ranges from 0.012 to 0.025 SI as determined by unpublished physical rock property measurements of the pluton (D.A. Ponce, oral commun., 2011). A magnetic susceptibility of 0.025 SI was used in the model as it best fits the data. The seismic velocity model (Fig. 22), rock property measurements (Table 1), and typical physical rock property measurements (Carmichael, 1982) were utilized when assigning both density and magnetic susceptibility values to the basin fill and surface geology in the models. Paleomagentic data (remanent magnetization) for the Bishop Tuff was also included in the models (Palmer and others, 1996).

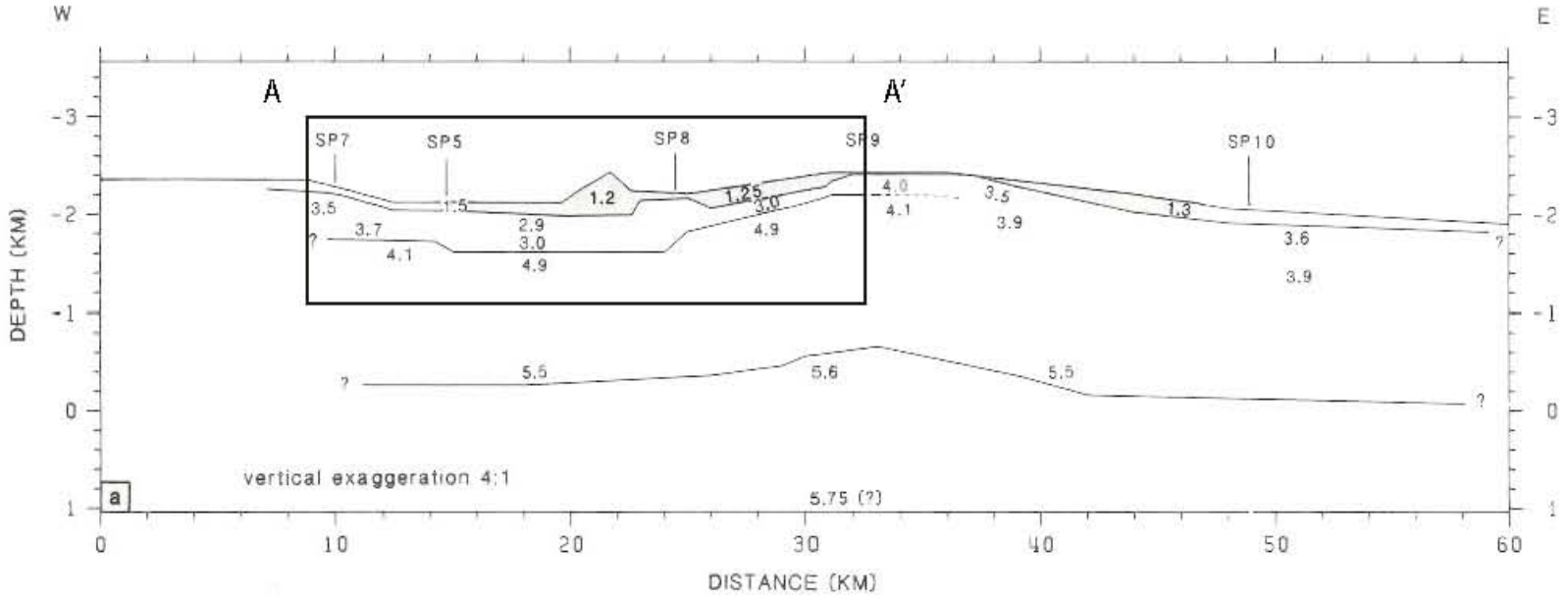

Figure 22. Seismic velocity model modified from Hill et al., 1985. Black box shows approximate location of profile A-A' and referenced velocities.

Gravity data show a decrease of about 11 mGal across the Mono Basin and a decrease of about 5 mGal across the Mono Domes. Aeromagnetic data across the profile show a decrease in magnetic field of around 140 nT across the Mono Basin, however, an increase of roughly 98 nT is observed across the Mono Domes.

Model A (Fig. 20, Table 4) suggests a basement high, or ridge, located under the Mono Domes. The ridge has an asymmetrical shape with more than half of its area west of the domes. The basin is approximately 700 m deep, and the basement ridge is roughly 400 m high, and 6 km wide. The construction report of the Mono Craters tunnel indicates drilling through a zone of highly fractured rock, indicating a fissure or fault zone, beneath the axis of the domes (Gresswell, 1940).

This suggests the basement rock beneath the domes has a lower density than the surrounding rock due to the fracturing caused by the eruption of the domes and/or from a pre-existing fault zone. For this model a basement ridge with a slightly lower density fits the data suggesting a faulted or fractured ridge block, Model B (Fig. 21, Table 4) is derived from work conducted by Shaffer and others (2010). This suggests an elongated cryptodome as a possible source for deformation underneath the northern end of the Mono Domes.

Table 4. Model parameters. Susc, magnetic susceptibility; M, remanent magnetization; MI, remanent inclination; MD, remanent declination; N/A, not available.

Model A			Paleomagnetic data		
Rock unit	Density (kg/m³)	Susc (SI)	M (SI)	MI (deg)	MD (deg)
Ka	2670	0.025	N/A	N/A	N/A
Jkg	2670	0.018	N/A	N/A	N/A
Ridge block	2600	0.025	N/A	N/A	N/A
Tv	2330	0.001	N/A	N/A	N/A
Qbt	2020	0.009	1.3	53	348
Qal	1900	0	N/A	N/A	N/A
Qp	1920	0	N/A	N/A	N/A
Qa	2400	0.025	N/A	N/A	N/A
Dike	1900	0.004	N/A	N/A	N/A
Model B			Paleomagnetic data		
Ka	2670	0.025	N/A	N/A	N/A
Jkg	2670	0.018	N/A	N/A	N/A
Cryptodome	2400	0.001	N/A	N/A	N/A
Tv 2	2330	0.001	N/A	N/A	N/A
Qbt	2020	0.009	1.3	53	348
Qal	1900	0	N/A	N/A	N/A
Qp	1920	0	N/A	N/A	N/A
Qa	2400	0.023	N/A	N/A	N/A
Dike	1900	0.004	N/A	N/A	N/A

A cryptodome is formed as a dike intrudes through crystalline basement and pools along the contact between the basement and overlying sediments (Shaffer and others, 2010; Fig. 23). The cryptodome model suggests a basin depth of about 700 m. The cryptodome is roughly 400 m thick and 6.5 km wide and is asymmetrically located slightly to the west beneath the Mono Domes. The density contrast between the cryptodome and the surrounding basin fill is relatively small. The magnetic susceptibility of the cryptodome is 0.025 SI (see Table 4) assuming it has a basaltic composition. Magnetic susceptibilities of the basement rock are the same as in Model A (Fig. 20).

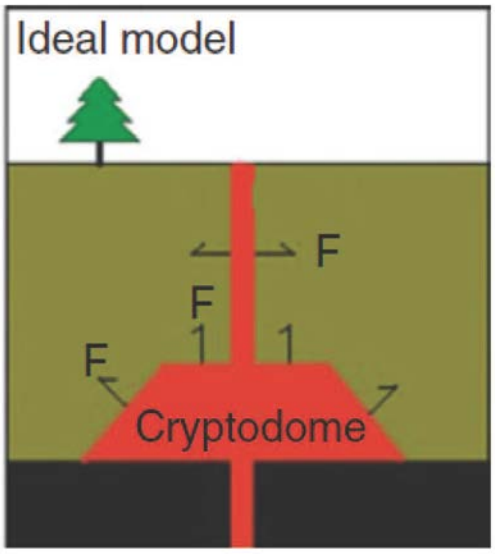

Figure 23. Model of a cryptodome from (Shaffer and others, 2010).

Ground magnetic data collected along profile A-A' (Fig. 24) shows a magnetic anomaly on the order of 180 nT just west of the Mono Domes near the location where the aeromagnetic high was observed. However, neither of the geophysical models produced a

magnetic anomaly great enough to match that of the magnetic high shown in the ground magnetic data. In order to fit the ground magnetic anomaly, a magnetic susceptibility of about 0.040 SI or greater would need to be given to a body about 4-km wide and roughly as deep as the basin.

It is possible that near-surface manmade magnetic objects could be affecting the ground magnetic data, producing a magnetic field not representative of the subsurface geology. Near-surface features would not be resolved in this aeromagneticdataset due to poor resolution, possibly accouting for the difference between the two datasets. The poor resolution of the aeromagnetic data also could affect the magnetic field intensity shown on the aeromagnetic anomaly map.

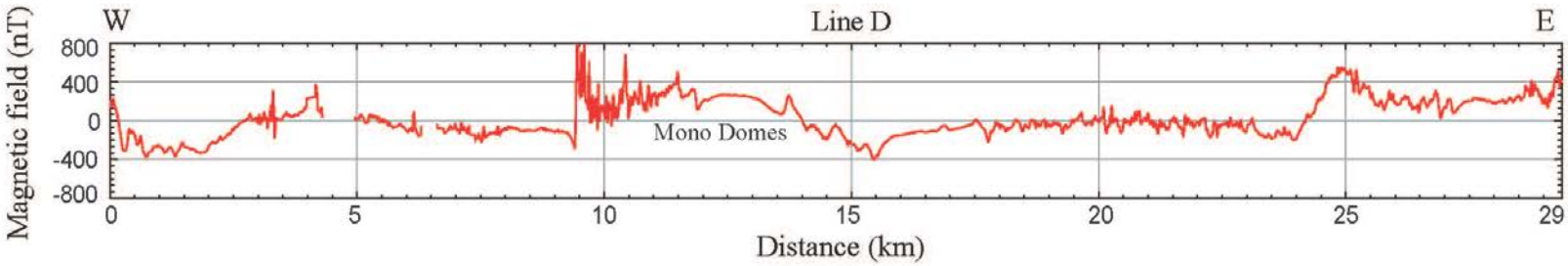

Figure 24. Ground magnetic data collected adjacent to profile A-A'. See Figure 11 for location of Line D.

DISCUSSION

In general, gravity highs in the study area reflect high-density plutonic rocks on the east and west sides of the Mono basin where granitic outcrops are exposed. Gravity lows are observed in Mono Lake and the Long Valley caldera where low-density volcanic rocks and sediments are prevalent; the boundaries of these features are distinctively marked by maximum horizontal gradients. In general, magnetic anomalies reflect moderately magnetic plutonic and volcanic rocks throughout the region. Within the study area, aeromagnetic data reveal an anomalous ring-shaped magnetic high centered over Aeolian Buttes whose eastern boundary follows the arcuate trend of the Mono Domes. The maximum horizontal gradient, reduction-to-the-magnetic-pole (RTP) and residual maps all clearly define the circular magnetic anomaly. The boundaries of the anomaly are delineated in the RTP and horizontal gradient maps. The residual map suggests the source of the anomaly is greater than 100 m deep and not related to near-surface features. Ground magnetic transects throughout the basin on the west side of the Mono Domes show magnetic lows and highs that correlate with the ring-shaped feature shown in the aeromagnetic data (Fig. 25).

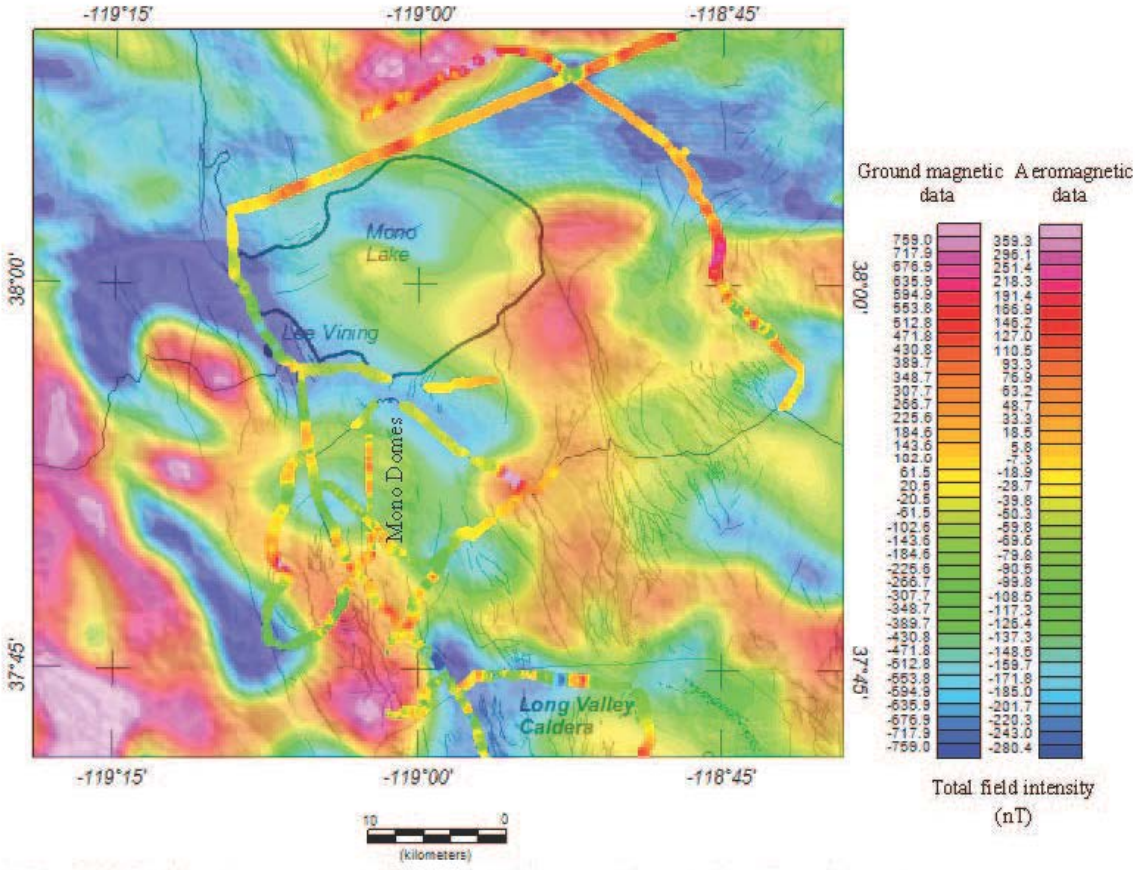

Figure 25. Map showing aeromagnetic data overlaid with truck-towed and ground magnetic data. Note truck-towed/ground magnetic data and aeromagnetic data do not have the same color scale. Truck-towed/ground magnetic data show highs and lows that correlate with aeromagnetic data in the region around the ring-shaped magnetic high, located west of the Mono Domes.

The preferred potential-field model that best supports previous work done in the area is the basement ridge model (Model A, Fig 20). This model suggests that a basement structure, or ridge, is located beneath the Mono Domes with its apex to the west of the domes. Re-analysis of seismic refraction data indicates a basement structure may be present beneath the Mono Domes, as suggested by further evaluations of first-arrival times (D. Hill, oral commun; 2011). The ridge is likely to be fractured and faulted,

possibly due to a pre-existing fault zone which could have served as a conduit for the eruption of the Mono Domes, reducing the ridge's density relative to the surrounding basement rock. The circular geometry of the ridge suggested by the ring-shaped magnetic anomaly is perplexing. Regional tectonics, extensional basin and range faulting, or complicated structural trends throughout the area could have influenced the formation the ridge beneath the domes. The ridge could be part of a horst-and-graben structure, considering the extensional structural trends throughout the region. Poor resolution of the aeromagnetic data may distort the geometry and boundaries of the anomalous magnetic high, possibly causing independent structures to appear as if they have a continuous circular shape. High-resolution aeromagnetic surveys may help delimit the circular magnetic anomaly and determine whether it could instead be the result of intersecting linear features.

The alternate model (Model B, Fig. 21), indicates a cryptodome could be the source of the magnetic anomaly across the Mono Domes. If a cryptodome is present it is possible that dense basaltic materials were trapped in the cryptodome as lighter, less dense rhyolites were erupted. Basaltic dikes 8 to 14 m wide were encountered around the rhyolitic Mono-Inyo feeder dike during the drilling of the Inyo Domes (Heiken and others, 1988), indicating that basaltic rock could be trapped around the Mono Domes conduit. Because basaltic materials have a much higher magnetic susceptibility than rhyolites, a basaltic body located beneath the Mono Domes could be the source of the magnetic high along the profile line. It is unlikely that basaltic intrusions like those found around the Inyo Domes would be the source of the magnetic anomaly because the

modeled width of these dikes were too narrow to produce an anomaly great enough to match the data. However, a large mass of moderately magnetic basaltic rock trapped in a cryptodome could produce a magnetic anomaly great enough to match the magnetic data in the model. Evidence for cryptodome deformation was observed at the northernmost end of the Mono Domes, near Panum crater (Shaffer and others, 2010). If basaltic rock was trapped by cryptodomes during the eruptions of the Mono Domes, the ring-shaped magnetic high should extend closer to the shoreline of Mono Lake. The location of cryptodome deformation does not correlate with the ring-shaped magnetic high, suggesting that a cryptodome is not likely to be associated with the magnetic anomaly located under the Mono Domes.

The anomalous ring-shaped magnetic high is essentially coincident with a ring fracture mapped by Kistler (1966) (Fig. 26). The ring fracture follows the trend of the Mono Domes; the magnetic high diverges from the domes at North Coulee and runs parallel to the northern trace of the ring fracture. The similarity of both trends could imply that the ring fracture and the magnetic high, or modeled basement ridge, are associated.

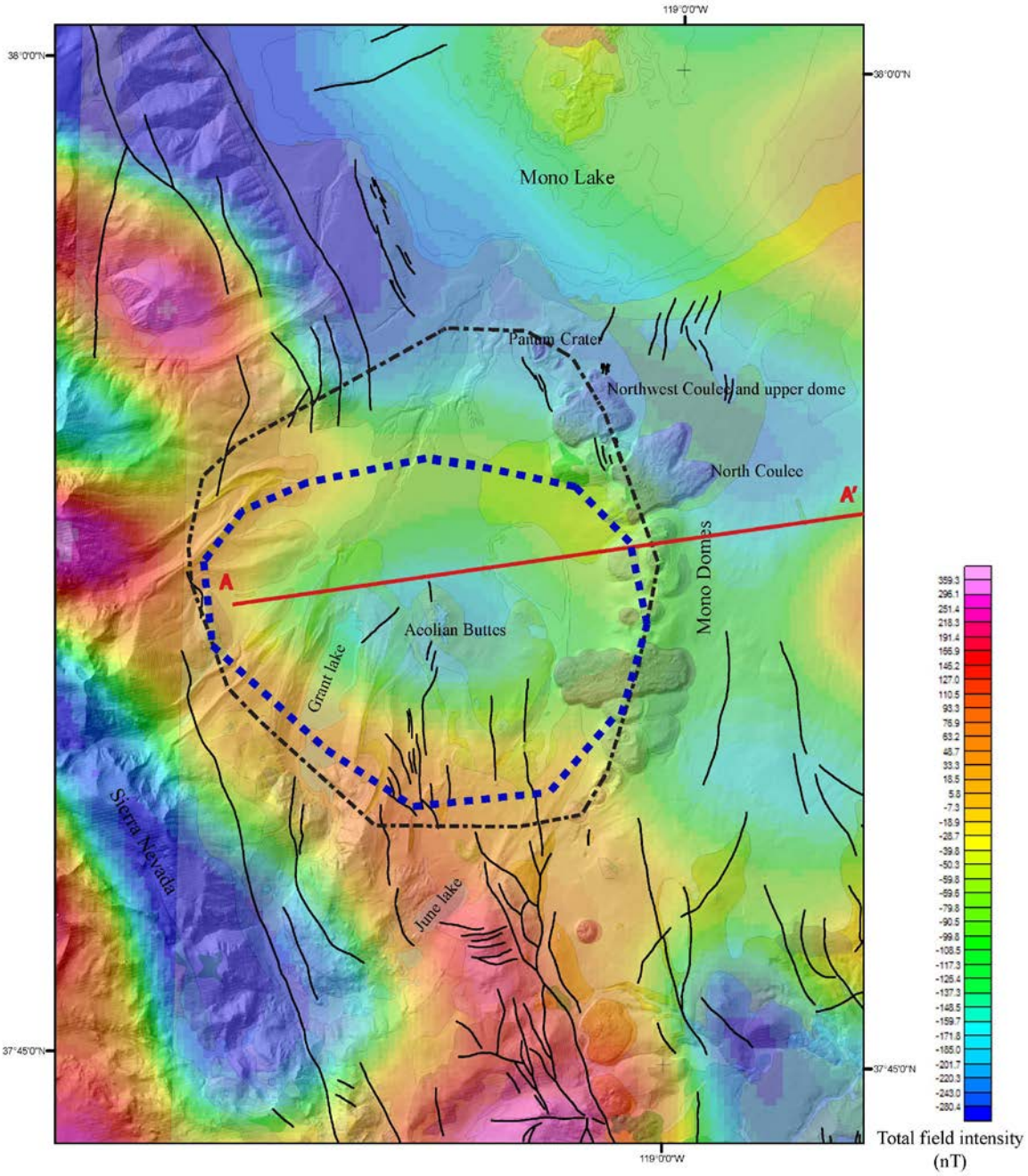

Figure 26. Interpretive map showing geologic map (Bailey, 1989) overlaid with aeromagnetic map (Roberts and Jachens, 1999). Black dashed circle shows location of ring fracture mapped by Kistler (1966). Blue dashed line shows location of interpreted ring-shaped magnetic high. The ring-shaped magnetic high is centered over Aeolian Buttes and coincides with the ring fracture with the exception of the northern trace. Profile A-A' (red line) extends off the map to the east.

In the event that volcanic activity occurs again in the region, eruptions could be focused within the pre-existing fracture zone beneath the domes, possibly continuing its arcuate trend to the west along the ring fracture trace. The close correlation between the circular magnetic anomaly and ring fracture has not been closely evaluated; it would be beneficial to investigate this relationship further to determine if the association holds any implications for future volcanic activity, but a higher resolution aeromagnetic survey would be required for any further analysis.

The most recent volcanic activity in the region occurred 250 ± 50 years ago at the northern end of the Mono-Inyo volcanic chain, forming Pahoa Island and Negit Island. The history of volcanic eruptions over the past 5000 years includes 20 small eruptions at 250-700 year intervals. Given the locations and intervals of eruptions, it is possible the magma chamber for the Mono-Inyo volcanic system could be utilized as a geothermal resource similar to the Casa Diablo geothermal plant located to the south of the Mono Basin, if a significant magma body can be located within the subsurface. We provide a useful foundation from which to continue investigations in this area to assess the geothermal potential the region may hold.

To better define the geometry and location of the basement ridge additional geophysical studies of the area are needed. Paleomagnetic data, which would provide remnant magnetizations of both volcanic and basement rocks, would be useful to constrain the geometry and size of the basement ridge. Additionally, high-resolution

aeromagnetic data would better define the boundaries of the circular-shaped magnetic high.

CONCLUSIONS

Geophysical models of the Mono Domes show that a moderately magnetic structure, 6 -km wide, with about 400 m of relief, and at a depth of about 700 m could be located beneath and slightly to the west of Mono Domes. Potential-field models indicate the basin depth to be roughly 700 m in Pumice Valley. The basement structure may be a fractured ridge, the eastern edge of which could have provided a pathway for the Mono Domes feeder dike. Re-evaluation of a seismic refraction survey conducted in 1985 supports the likelihood of a basement structure. Aeromagnetic data suggests the ridge has a circular geometry. Alternately, the unusual geometry could be due to complicated intersecting structural trends in the area, attributable to the combination of the Mina Deflection, Sierran frontal fault systems, and Basin and Range faulting. A ring fracture mapped by Kistler (1966) coincides with the circular magnetic anomaly, suggesting the two features may be associated. The ring fracture may have been the pre-existing fracture zone that served as the conduit for the Mono Domes feeder dike. Additional geophysical studies are needed to further delineate the shape and origin of the basement ridge.

REFERENCES CITED

Achauer, U., Greene, L., Evans, J.R., and Iyer, H.M., 1986, Nature of the magma chamber underlying the Mono Craters area, Eastern California, as determined from teleseismic travel time residuals: Journal of Geophysical Research, v. 91, no. B14, p. 13,873-13,891.

Axtell, L.H., 1972, Mono Lake geothermal wells abandoned: California Geology, v. 25, p. 66 – 68.

Bailey, R., Dalrymple, G.B., and Lanphere, M.A., 1976, Volcanism, structure and geochronology of Long Valley Caldera, Mono County, California: Journal of Geophysical Research, v. 81, no. 5, p. 725-744.

Bailey, R.A., 1982, Chemical evolution and current state of the Long Valley magma chamber,U.S. Geological Survey, Open-File Report, 84-939, p. 24-40.

Bailey, R., 1989, Geologic map of Long Valley Caldera, Mono-Inyo Craters volcanic chain, andvicinity, Eastern California: U.S. Geological Survey, scale 1:62,500, 2 sheets, 11 p.

Barnes, D.F., Oliver, H.W., and Robbins, S.L., 1969, Standardization of gravimeter calibrations in the Geological Survey: Eos, Transactions, American Geophysical Union, v. 50, no. 10, p. 626-627.

Battaglia, M., Williams, M.J., Venezky, D.Y., Hill, D.P., Langbein, J.O., Farrar, J.F., Howle, M., Sneed, M., Segall, P., 2003, Long Valley Caldera GIS database, U.S. Geological Survey, Digital Data Series DDS-81.

Blakely, R.J., and Simpson, R.W., 1986, Approximating edges of source bodies from gravity or magnetic data: Geophysics, v. 51, p. 1494-1498.

Blakely, R.J., 1995, Potential theory in gravity and magnetic applications: New York, Cambridge University Press, 441 p.

Bursik, M., and Sieh, K., 1989, Range front faulting and volcanism in the Mono Basin, Eastern California: Journal of Geophysical Research, v. 94, no. B11, p. 15, 587-15,609.

Bursik, M., Renshaw, C., McCalpin, J., and Berry, M., 2003, A volcanotectonic cascade: Activation of range front faulting and eruptions by dike intrusion, Mono Basin – Long Valley Caldera, California: Journal of Geophysical Research, v. 108, no. b8, 2393, doi:10.1029/2002JB002032.

Carmichael, R.S., 1982, Handbook of physical rock properties: CRC Press, Boca Raton, Fla. Vol. III.

Christensen, M.N., Gilbert, C.M., Lajoie, K.R., and Al-Rawi, Yehya, 1969, Geological-geophysical interpretation of Mono Basin, California-Nevada: Journal of Geophysical
Research, v. 74, no. 22, p. 5221-5239.

Gardner, G.H.F., Gardner, L.W., and Gregory, A.R., 1974, Formation of velocity and density; The diagnostic basics for stratigraphic traps: Geophysics, v.39, p. 770-780.

Gilbert, C.M., Christensen, M.N., Al Rawi, Y., and Lajoie, K.R., 1968, Structural and volcanic history of Mono Basin, California-Nevada: Geological Society of America Memoirs,116, p. 275-329.

Godson, R.H., and Plouff, Donald, 1988, BOUGUER version 1.0, a microcomputer gravity-terrain-correction program: U.S. Geological Survey Open-File Report 88-644-A, Documentation, 22 p.; 88-644-B, Tables, 61 p., 88-644-C, 5 1/4 - in diskette.

Gresswell, W.K., 1940, Short report on the geological formations encountered in driving the Mono Craters tunnel: California Division of Mines and Geology Bulletin, v. 36, p. 199- 204.

Hayford, J.F., and Bowie, William, 1912, The effect of topography and isostatic compensation upon the intensity of gravity: U.S. Coast and Geodetic Survey Special Publication no. 10, 132 p.

Henry, C.D., and Faulds, J.E., 2005, Coupled magmatic-tectonic evolution of the Walker Lane,Western Nevada and eastern California, *in* Proceedings, Penrose

Conference: Kinematics and Geodynamics of Inraplate Dextral Shear in Eastern California and Western Nevada, p. 18-19.

Hermance, J.F., Slocum, W.M., and Neumann, G.A., 1984, The Long Valley/Mono Basin volcanic complex: A preliminary magentotelluric and magnetic variation interpretation: Journal of Geophysical Research, v. 89, no. B10, p. 8325-8337.

Heiken, G.H., Wohletz, K.H., and Eichelberger, J.C., 1988, Fracture fillings and intrusive Pyroclasts, Inyo Domes, California: Journal of Geophysical Research, 93, p. 4335-4350.

Hildreth, W., 2004, Volcanological perspectives on Long Valley, Mammoth Moutain, and Mono Craters: several contiguous but discrete systems: Journal of Volcanology and Geothermal Research, 136, p.169-198.

Hill, D.P., Kissling, E., Luetgert, J.H., Kradolfer, U., 1985, Constraints on the upper structure of the Long Valley-Mono Craters volcanic complex, Eastern California, from seismic refraction experiments: Journal of Geophysical Research, v. 90, no. B13, p. 11,135 –11,150.

Hill, D.P., 2006, Unrest in Long Valley Caldera, California: 1978-2004, *in* Troise, C., De Natale, G., & Kilburn, C.R.J. (eds) Mechanisms of Activity and Unrest at Large Calderas, Geological Society, London, Special Publication 269, pp. 1-24.

International Union of Geodesy and Geophysics, 1971, Geodetic reference system 1967: International Association of Geodesy Special Publication no. 3, 116 p.

Jachens, R.C., and Roberts, C.W., 1981, Documentation of a FORTRAN program, 'isocomp', for computing isostatic residual gravity: U.S. Geological Open-File Report 81-574, 26 p.

Jacques, H.L., 1940, Mono Craters tunnel construction problems: Journal of the American Water Works Association, v. 32, no. 1, p. 43-56.

Jennings, C.W., Strand, R.G., and Rogers, T.H., 1977, Geologic map of California: California Division of Mines and Geology, scale 1:750,000

Kister, R.W., 1966, Structure and metamorphism in the Mono Craters quadrangle, Sierra Nevada, California: U.S. Geol. Surv. Bull. 122-E, p. E1-E53.

Lee, J., and Stockli, D., 2005, Fault slip transfer in the eastern California shear zone/Walker Lane belt, *in* Proceedings, Penrose Conference: Kinematics and Geodynamics of Inraplate Dextral Shear in Eastern California and Western Nevada, p. 7 – 8.

Morelli, C., ed., 1974, The International Gravity Standardization Net 1971: International Association of Geodesy Special Publication no. 4, 194 p.

Pakiser, L.C., Press, F., and Kane, M.F., 1960, Geophysical investigation of Mono Basin, California: Bulletin of the Geological Society of America, v. 71, p. 415-448.

Pakiser, L.C., 1976, Seismic exploration of Mono Basin, California: Journal of GeophysicalResearch, v. 81, no. 20, p. 3607-3618.

Palmer, H.C., MacDonald, W.D., Gromme, C.S., and Ellwood, B.B., 1996, Magnetic properties and emplacement of the Bishop Tuff, California: Bulletin of Volcanology,v.58, p. 101-116.

Plouff, Donald, 1966, Digital terrain corrections based on geographic coordinates [abs.]: Geophysics, v. 31, no. 6, p. 1208.

Plouff, Donald, 1977, Preliminary documentation for a FORTRAN program to compute gravity terrain corrections based on topography digitized on a geographic grid: U.S. Geological Survey Open-File Report 77-535, 45 p.

Roberts, C.W., and Jachens, R.C., 1999, Preliminary aeromagnetic anomaly map of California: U.S. Geological Survey Open-File Report 99-440, 14 p.

Schaffer, W., Bursik, M., and Renshaw., C., 2010, Elastic source model of the North Mono eruption (1325-1368 A.D.) based on shoreline deformation; Bulletin of Volcanology, doi 10.1007/s00445-010-0385-4.

Sieh, K., and Bursik, M., 1986, Most recent eruption of the Mono Craters, Eastern Central California: Journal of Geophysical Research, v. 91, no. B12, p. 12,539-12,571.

Stewart, J.H., and Carlson, J.E., 1978, Geologic map of Nevada: U.S. Geological Survey, scale 1:500,000.

Swick, C.A., 1942, Pendulum gravity measurements and isostatic reductions: U.S. Coast and Geodetic Survey Special Publication 232, 82 p.

APPENDIX A

GRAVITY BASE STATIONS

GRAVITY BASE STATION

NAME	CITY/STATE
LEEVIN	Lee Vining, California
LATITUDE/LONGITUDE/ELEVATION (NAD27/29) 37°57.34' 119°07.14' 6794.9 ft (GPS)	ACIC Reference No. (Jablonski, 1974) N.A.
OBSERVED GRAVITY (IGSN71) 979,348.30 milligals	(n=2, from Mammoth Lakes MLEQB1)

DESCRIPTION

The station is located at the U.S. Post Office in Lee Vinning, Califonria. The station is outside the front (north side) of the post office, at the left (east) corner of the building, on a cement apron. Read the meter in the corner of the building and the edge of the cement arpon, read the meter facing the building (south).

PHOTO

REFERENCES

GRAVITY BASE STATION

NAME	CITY/STATE
MLEBQ1	Mammoth Lakes/Toms Place, California
LATITUDE/LONGITUDE/ELEVATION (NAD27/29) 37°33.80' 118°41.68' 6951.5 ft (GPS)	ACIC Reference No. (Jablonski, 1974) N.A.
OBSERVED GRAVITY (IGSN71) 979,312.160 milligals	

DESCRIPTION

Station is located near the intersection of U.S. Highway 395 and Rock Creek Road at Toms Place, south of Mammoth Lakes, California. From Toms Place and Highway 395 drive west 0.8 mi on Rock Creek Road, then turn right on Rainbow Tarns Road, then 0.3 mi north. Station is beyond a gated fence, at the edge of a small grassy meadow, on a granitic boulder at the base of a rocky hill, on the north side of the meadow. Site is midway along top of rock about 6 ft above the meadow, and marked with a standard USGS hexagonal gravity marker stamped MLEQB1 1980. Read with the meter facing north. Description revised 6/2010.

PHOTO (by D.A. Ponce, U.S. Geological Survey, 2010)

REFERENCES

Roberts, C.W., Jachens, R.C., and Morin, R.L., 1988, High-precision stations for monitoring gravity changes in Long Valley caldera, California: U.S. Geological Survey Open-File Report 88-50, 19 p.

APPENDIX B

PHYSICAL ROCK PROPERTIES

	Type	Grain Density	GD Ave	Sat. Blk Density	SBD Ave	Dry Bulk Density	DBD Ave	SUSC	SUSC Ave
Sample ID		← kg/m^3 →						← SI →	
10AAPM02A		2488		2329		2222		20.87	
10AAPM02B		2459		2319		2224		12.79	
10AAPM02C	BA	2485	2557	2395	1970	2335	2363	8.02	13.48
10AAPM02D		2508		2.354		2252		14.1	
09MB0004		2847		2806		2783		11.6	
10AAPM03A		2002		1951		1900		0.56	
10AAPM03B		1782		1732		1669		0.48	
10AAPM06B		2153		2122		2096		1.47	
10AAPM06C		2194		2120		2057		1.72	
10MB0020A	OB	1448	2018	1535	1990	1731	1975	0.39	0.78
10MB0020B		2091		2045		2004		0.68	
10MB0020C		2157		2116		2081		0.62	
10MB0020D		2264		2249		2224		0.84	
10MB0020E		2073		2040		2009		0.25	
10MB0028A		2665		2627		2605		10.95	
10MB0028B	GD	2688	2684	647	1983	2623	2629	12.75	13.21
10MB0028C		2699		2674		2660		15.92	
10ELL001A		2130		1879		1656		2.85	
10EEL001B		2038		1756		1484		2.85	
10EEL001C	TU	2058	1935	1774	1687	1506	1419	3	2.46
10MB0064A		1377		1274		1001		1.43	
10MB0064B		1924		1649		1351		1.78	
10EEL001D		2084		1789		1516		2.84	
10AAPM05B		2278		2216		2167		5.77	
10AAPM05C		2292		2206		2140		5.25	
10AAPM04A		2167		2200		2228		0.51	
10AAPM04B		2062		1970		1883		0.46	
10AAPM04C		2217		2147		2089		0.51	
10AAPM04D		2152		2058		1976		0.56	
10AAPM05A		2161		2094		2037		5.33	
10AAPM06A	RH	1916	1831	1843	1774	1765	1687	1.09	1.50
10MB0131A		1304		1252		1080		0.26	
10MB0131B		1231		1205		1092		0.28	
10MB0075A		1560		1505		1406		0.53	
10MB0075B		1854		1809		1758		0.73	
10AAPM01A		1377		1274		1001		1.43	
10AAPM01B		1497		1443		1334		0.61	
10AAPM01C		1461		1421		1335		0.24	
09MB0003		1773		1739		1694		0.41	
10MB0115A		2693		2649		2624		13.22	
10MB0115B		2685		2635		2605		13.74	
10MB0115C		2685		2635		2605		13.08	
09MB0002	GR	2600	2672	2540	2615	2503	2581	2.46	5.54
09MB0005		2917		2865		2839		0.27	
MLEQB1A		2598		2531		2489		0.25	
MLEQB1B		2597		2530		2488		0.29	
MLEQB1C		2604		2534		2491		1.02	
09MB0001	MT	2675	2675	2651	2651	2636	2636	0.03	0.03

NOTES:

BA, basalt; OB, obsidian; GD, granodiorite, TU, Bishop Tuff; RH, rhyolite; GR, granite; MT, metasediment

APPENDIX C

GRAVITY DATA

ID	LAT	LONG	ELEV_M	OG	TG	FAC	BC	CC	ITC	OTC	TTC	TISOC	FAA	SBA	CBA	ISO
10MB0045	37.8893330	-118.9396670	2258.29	979306.4	979982.39	696.55	-252.699	-1.505	0.15	2.05	2.2	203.49	20.57	-232.13	-231.43	-27.94
10MB0046	37.8876670	-118.9338330	2292.4	979302	979982.25	707.06	-256.516	-1.5	0.17	2.06	2.23	203.41	26.79	-229.73	-229	-25.59
10MB0047	37.8841670	-118.9288330	2315.47	979297.7	979981.94	714.18	-259.097	-1.496	0.23	2.06	2.29	203.34	29.96	-229.14	-228.34	-25
10MB0048	37.8861670	-118.9135000	2369.24	979289.1	979982.12	730.75	-265.114	-1.486	0.18	2.13	2.31	203.22	37.71	-227.41	-226.58	-23.36
10MB0049	37.8840000	-118.9003330	2436.02	979278.3	979981.93	751.34	-272.587	-1.47	0.2	2.3	2.5	203.07	47.66	-224.92	-223.89	-20.82
10MB0050	37.8971670	-118.8383330	2357.45	979298.7	979983.08	727.11	-263.794	-1.488	0.64	1.96	2.6	202.73	42.7	-221.1	-219.98	-17.25
10MB0051	37.8936670	-118.8323330	2344.98	979301.5	979982.77	723.27	-262.399	-1.491	0.61	2.01	2.62	202.71	42.02	-220.38	-219.25	-16.54
10MB0052	37.8895000	-118.8261670	2343.24	979303	979982.41	722.74	-262.205	-1.491	0.4	2.04	2.44	202.69	43.36	-218.84	-217.89	-15.2
10MB0053	37.8873330	-118.8166670	2307.85	979311.4	979982.22	711.83	-258.245	-1.497	0.43	2.02	2.45	202.7	40.98	-217.26	-216.31	-13.61
10MB0054	37.8880000	-118.8090000	2265.91	979317.2	979982.28	698.9	-253.552	-1.504	0.31	2.03	2.34	202.74	33.8	-219.76	-218.92	-16.18
10MB0055	37.8891670	-118.7990000	2249.97	979321.3	979982.38	693.98	-251.768	-1.506	0.24	1.93	2.17	202.66	32.92	-218.85	-218.19	-15.53
10MB0056	37.8903330	-118.7903330	2235.98	979322.1	979982.48	689.67	-250.202	-1.508	0.08	1.87	1.95	202.58	29.28	-220.92	-220.48	-17.9
10MB0057	37.8921670	-118.7786670	2202.79	979326.4	979982.64	679.44	-246.488	-1.511	0.15	1.85	2	202.44	23.18	-223.31	-222.82	-20.38
10MB0058	37.8903330	-118.7690000	2221.41	979322.5	979982.48	685.18	-248.572	-1.509	0.22	1.79	2.01	202.33	25.23	-223.34	-222.84	-20.51
10MB0059	37.8920000	-118.7596670	2202.36	979326.6	979982.63	679.31	-246.44	-1.511	0.18	1.75	1.93	202.3	23.32	-223.12	-222.7	-20.4
10MB0060	37.8963330	-118.7518330	2185.75	979330.5	979983.01	674.18	-244.582	-1.512	0.16	1.72	1.88	202.21	21.66	-222.92	-222.55	-20.34
10MB0061	37.8996670	-118.7455000	2167.83	979334.4	979983.3	668.66	-242.576	-1.514	0.26	1.68	1.94	202.1	19.75	-222.82	-222.4	-20.3
10MB0062	37.9066670	-118.7321670	2135.89	979342.9	979983.91	658.81	-239.002	-1.516	0.7	1.58	2.28	201.91	17.81	-221.19	-220.42	-18.51
10MB0063	37.9105000	-118.7221670	2109	979348.3	979984.25	650.52	-235.994	-1.516	0.25	1.5	1.75	201.77	14.62	-221.37	-221.14	-19.37
10MB0064	37.9160000	-118.7133330	2068.83	979358.8	979984.73	638.14	-231.498	-1.517	0.37	1.43	1.8	201.66	12.19	-219.31	-219.02	-17.36
10MB0065	37.9210000	-118.7051670	2009.24	979369	979985.17	619.77	-224.831	-1.516	0.41	1.46	1.87	201.57	3.56	-221.27	-220.92	-19.34
10MB0066	37.8656670	-118.9123330	2399.39	979277.6	979980.32	740.04	-268.487	-1.479	0.18	2.17	2.35	203.27	37.34	-231.15	-230.28	-27.01
10MB0067	37.8548330	-118.9280000	2428.1	979270.2	979979.37	748.89	-271.7	-1.472	0.26	2.21	2.47	203.3	39.7	-232	-231	-27.7
10MB0068	37.8438330	-118.9466670	2393.96	979273.5	979978.41	738.37	-267.88	-1.481	0.08	2.15	2.23	203.42	33.45	-234.43	-233.68	-30.26
10MB0069	37.8318330	-118.9713330	2462.08	979259.9	979977.36	759.37	-275.503	-1.463	0.09	2.25	2.34	203.24	41.94	-233.56	-232.69	-29.45
10MB0070	37.8251670	-118.9800000	2414.99	979269.2	979976.77	744.85	-270.233	-1.476	0.13	2.18	2.31	203.27	37.25	-232.99	-232.15	-28.88
10MB0071	37.8185000	-118.9896670	2399.51	979272.5	979976.19	740.08	-268.501	-1.479	0.09	2.23	2.32	203.24	36.41	-232.09	-231.25	-28.01
10MB0072	37.8193330	-118.9946670	2393.59	979273.1	979976.26	738.26	-267.839	-1.481	0.13	2.26	2.39	203.2	35.1	-232.74	-231.83	-28.63
10MB0073	37.8206670	-119.0031670	2341.44	979282.8	979976.38	722.18	-262.003	-1.491	0.64	2.39	3.03	203.26	28.62	-233.38	-231.84	-28.58
10MB0074	37.8218330	-119.0093330	2362.2	979280.5	979976.48	728.58	-264.326	-1.487	1.17	2.4	3.57	203.19	32.65	-231.68	-229.6	-26.41
10MB0075	37.8246670	-119.0153330	2436.75	979256.7	979976.73	751.56	-272.668	-1.47	2.22	2.51	4.73	203.01	31.58	-241.09	-237.83	-34.82
10MB0076	37.8263330	-119.0200000	2370.7	979275.6	979976.87	731.2	-265.278	-1.486	1.96	2.5	4.46	203.09	29.93	-235.34	-232.37	-29.28
10MB0077	37.8301670	-119.0243330	2313.19	979286.3	979977.21	713.47	-258.842	-1.497	1.5	2.62	4.12	203.21	22.55	-236.29	-233.67	-30.46
10MB0078	37.8351670	-119.0295000	2291.67	979292.2	979977.65	706.84	-256.434	-1.5	0.82	2.73	3.55	203.2	21.38	-235.06	-233.01	-29.81
10MB0079	37.8388330	-119.0335000	2256.77	979299	979977.97	696.08	-252.529	-1.505	1.1	2.92	4.02	203.27	17.08	-235.45	-232.94	-29.67
10MB0080	37.8440000	-119.0388330	2253.54	979299.8	979978.42	695.08	-252.167	-1.505	0.77	2.92	3.69	203.27	16.46	-235.71	-233.53	-30.26
10MB0081	37.8486670	-119.0448330	2237.99	979304.3	979978.83	690.29	-250.428	-1.507	0.34	2.92	3.26	203.26	15.72	-234.71	-232.96	-29.7
10MB0082	37.8541670	-119.0525000	2173.83	979316.2	979979.31	670.51	-243.248	-1.513	0.27	3.18	3.45	203.33	7.36	-235.88	-233.95	-30.62
10MB0083	37.8580000	-119.0585000	2152.25	979320.8	979979.65	663.86	-240.833	-1.515	0.2	3.26	3.46	203.33	4.99	-235.84	-233.89	-30.56
10MB0084	37.8625000	-119.0646670	2126.8	979325.3	979980.04	656.01	-237.985	-1.516	0.29	3.38	3.67	203.34	1.27	-236.71	-234.56	-31.22
10MB0085	37.8503330	-119.0605000	2202.24	979310.7	979978.98	679.27	-246.427	-1.511	0.25	3.12	3.37	203.18	10.95	-235.48	-233.62	-30.44
10MB0086	37.8446670	-119.0685000	2247.23	979302.5	979978.48	693.14	-251.461	-1.506	0.19	3.2	3.39	202.97	17.2	-234.26	-232.37	-29.4
10MB0087	37.8181670	-119.0483330	2318.71	979286.4	979976.16	715.17	-259.459	-1.496	0.12	3.01	3.13	202.86	25.44	-234.02	-232.39	-29.53
10MB0088	37.8231670	-119.0415000	2305.63	979288.8	979976.6	711.14	-257.996	-1.498	0.16	2.88	3.04	203.02	23.33	-234.67	-233.12	-30.1
10MB0089	37.8300000	-119.0343330	2302.52	979290.6	979977.2	710.18	-257.648	-1.498	0.28	2.77	3.05	203.15	23.55	-234.09	-232.54	-29.39

ID	LAT	LONG	ELEV_M	OG	TG	FAC	BC	CC	ITC	OTC	TTC	TISOC	FAA	SBA	CBA	ISO
10MB0090	37.8513330	-119.0383330	2251.56	979302.2	979979.06	694.47	-251.945	-1.506	0.74	2.87	3.61	203.29	17.57	-234.37	-232.27	-28.98
10MB0091	37.8586670	-119.0400000	2207.88	979311.8	979979.71	681.01	-247.058	-1.511	0.23	3	3.23	203.36	13.11	-233.95	-232.23	-28.87
10MB0092	37.8656670	-119.0400000	2188.46	979314.5	979980.32	675.02	-244.885	-1.512	0.09	3.02	3.11	203.41	9.22	-235.67	-234.07	-30.66
10MB0093	37.8730000	-119.0401670	2164.6	979320.4	979980.96	667.66	-242.215	-1.514	0.08	3.01	3.09	203.47	7.07	-235.15	-233.57	-30.1
10MB0094	37.8890000	-119.0415000	2128.57	979326.3	979982.37	656.56	-238.183	-1.516	0.22	2.88	3.1	203.58	0.51	-237.68	-236.09	-32.51
10MB0095	37.8970000	-119.0416670	2114.09	979328.7	979983.07	652.09	-236.563	-1.516	1.11	2.77	3.88	203.59	-2.28	-238.84	-236.48	-32.89
10MB0096	37.9055000	-119.0430000	2097.57	979331.7	979983.81	647	-234.715	-1.517	1.01	2.67	3.68	203.61	-5.13	-239.84	-237.68	-34.07
10MB0097	37.9230000	-119.0463330	2078.46	979331.7	979985.34	641.11	-232.576	-1.517	0.18	2.54	2.72	203.58	-12.56	-245.14	-243.94	-40.36
10MB0098	37.9315000	-119.0513330	2056.06	979333.4	979986.09	634.2	-230.069	-1.517	0.29	2.53	2.82	203.59	-18.54	-248.6	-247.3	-43.71
10MB0099	37.9463330	-119.0693330	1978.15	979348.9	979987.39	610.18	-221.352	-1.514	0.27	3	3.27	203.64	-28.36	-249.71	-247.95	-44.31
10MB0100	37.8886670	-119.0700000	2090.47	979336.6	979982.34	644.81	-233.92	-1.517	0.01	3.18	3.19	203.41	-0.93	-234.85	-233.18	-29.77
10MB0101	37.8828330	-119.0666670	2092.7	979334.7	979981.82	645.5	-234.169	-1.517	0.02	3.2	3.22	203.47	-1.64	-235.81	-234.11	-30.64
10MB0102	37.8831670	-119.0486670	2132.69	979326.2	979981.85	657.82	-238.644	-1.516	0.07	2.89	2.96	203.51	2.22	-236.43	-234.98	-31.47
10MB0103	37.8921670	-119.0471670	2115.37	979329.2	979982.64	652.49	-236.706	-1.516	0.16	2.84	3	203.59	-0.93	-237.64	-236.15	-32.56
10MB0104	37.8941670	-119.0223330	2241.86	979299.8	979982.82	691.48	-250.861	-1.507	2.91	2.56	5.47	203.37	8.48	-242.38	-238.42	-35.05
10MB0105	37.8938330	-119.0298330	2176.55	979315.3	979982.79	671.35	-243.552	-1.513	2.05	2.64	4.69	203.49	3.81	-239.74	-236.56	-33.07
10MB0106	37.8780000	-119.0281670	2177.13	979314.5	979981.4	671.53	-243.616	-1.513	1.03	3.02	4.05	203.53	4.66	-238.96	-236.42	-32.89
10MB0107	37.8708330	-119.0243330	2205.99	979308.6	979980.77	680.42	-246.846	-1.511	2.09	2.93	5.02	203.47	8.28	-238.57	-235.06	-31.59
10MB0108	37.8668330	-119.0315000	2195.72	979312.5	979980.42	677.26	-245.697	-1.512	0.47	3.13	3.6	203.46	9.38	-236.32	-234.23	-30.77
10MB0109	37.8668330	-119.0243330	2217.12	979306.6	979980.42	683.85	-248.091	-1.51	1.95	2.93	4.88	203.47	10.02	-238.07	-234.7	-31.23
10MB0110	37.8590000	-119.0213330	2285.76	979292.5	979979.74	705.01	-255.772	-1.501	3.22	2.64	5.86	203.33	17.78	-237.99	-233.63	-30.3
10MB0111	37.8588330	-119.0271670	2239.64	979302.2	979979.72	690.8	-250.612	-1.507	1.48	2.89	4.37	203.42	13.31	-237.3	-234.44	-31.02
10MB0112	37.8555000	-119.0251670	2265.24	979295.8	979979.43	698.69	-253.477	-1.504	2.8	2.75	5.55	203.36	15.02	-238.46	-234.41	-31.05
10MB0113	37.8410000	-119.0440000	2307.28	979290.5	979978.16	711.65	-258.18	-1.498	0.47	2.77	3.24	203.12	23.98	-234.2	-232.46	-29.34
10MB0114	37.8356670	-119.0488330	2367.53	979277.3	979977.69	730.22	-264.923	-1.486	0.86	2.82	3.68	202.91	29.84	-235.08	-232.89	-29.98
10MB0115	37.8335000	-119.0536670	2415.97	979268.8	979977.5	745.15	-270.342	-1.475	1.45	3	4.45	202.73	36.42	-233.92	-230.95	-28.22
10MB0116	37.8236670	-119.0548330	2321.39	979286.2	979976.64	716	-259.759	-1.495	0.21	3	3.21	202.85	25.59	-234.17	-232.45	-29.6
10MB0117	37.8075000	-119.0583330	2335.23	979280.7	979975.22	720.27	-261.308	-1.493	0.35	3.44	3.79	202.65	25.74	-235.57	-233.27	-30.62
10MB0118	37.8031670	-119.0646670	2341.23	979280.3	979974.85	722.12	-261.979	-1.492	0.78	3.74	4.52	202.49	27.57	-234.41	-231.38	-28.89
10MB0119	37.8023330	-119.0695000	2344.34	979278.5	979974.77	723.08	-262.327	-1.491	0.35	3.93	4.28	202.4	26.81	-235.52	-232.73	-30.33
10MB0120	37.8031670	-119.0768330	2337.51	979281.1	979974.85	720.97	-261.563	-1.492	0.84	4.08	4.92	202.32	27.2	-234.36	-230.94	-28.62
10MB0121	37.8081670	-119.0780000	2339.25	979281.2	979975.28	721.51	-261.758	-1.492	0.81	3.91	4.72	202.37	27.42	-234.34	-231.11	-28.74
10MB0122	37.8145000	-119.0786670	2345.41	979281	979975.84	723.4	-262.447	-1.491	0.47	3.75	4.22	202.4	28.58	-233.87	-231.14	-28.74
10MB0123	37.8218330	-119.0793330	2298.74	979290.6	979976.48	709.02	-257.225	-1.499	0.6	3.8	4.4	202.53	23.16	-234.06	-231.16	-28.63
10MB0124	37.8280000	-119.0770000	2280.48	979294.7	979977.02	703.39	-255.182	-1.502	0.38	3.64	4.02	202.68	21.11	-234.07	-231.55	-28.87
10MB0125	37.8346670	-119.0770000	2246.22	979301.9	979977.6	692.83	-251.348	-1.506	0.4	3.65	4.05	202.77	17.15	-234.2	-231.66	-28.89
10MB0126	37.8993330	-118.9798330	2140.98	979323.7	979983.27	660.38	-239.571	-1.515	0.28	2.45	2.73	203.66	0.84	-238.74	-237.52	-33.86
10MB0127	37.8730000	-118.9843330	2353.24	979280.5	979980.96	725.82	-263.323	-1.489	0.91	2.42	3.33	203.33	25.33	-237.99	-236.15	-32.82
10MB0128	37.8658330	-118.9850000	2396.64	979272	979980.33	739.2	-268.18	-1.48	0.87	2.48	3.35	203.26	30.91	-237.27	-235.4	-32.14
10MB0129	37.8586670	-118.9863330	2424.93	979266.5	979979.71	747.92	-271.345	-1.473	0.57	2.49	3.06	203.21	34.68	-236.66	-235.07	-31.86
10MB0130	37.8510000	-118.9911670	2427.98	979265.5	979979.04	748.86	-271.686	-1.472	1.04	2.41	3.45	203.2	35.3	-236.39	-234.41	-31.21
10MB0131	37.8465000	-118.9913330	2425.23	979267.1	979978.64	748.01	-271.379	-1.473	0.96	2.36	3.32	203.22	36.47	-234.91	-233.07	-29.85
10MB0132	37.8385000	-118.9955000	2403.59	979269.2	979977.94	741.34	-268.958	-1.478	1.33	2.28	3.61	203.27	32.58	-236.38	-234.25	-30.98
10MB0133	37.8296670	-118.9993330	2408.53	979267.9	979977.17	742.86	-269.51	-1.477	1.1	2.31	3.41	203.17	33.63	-235.88	-233.95	-30.78
10MB0134	37.8221670	-119.0090000	2362.81	979280.4	979976.51	728.77	-264.394	-1.487	1.29	2.39	3.68	203.19	32.61	-231.78	-229.59	-26.4

ID	LAT	LONG	ELEV_M	OG	TG	FAC	BC	CC	ITC	OTC	TTC	TISOC	FAA	SBA	CBA	ISO
10MB0135	37.8223330	-118.9826670	2427.88	979266.3	979976.52	748.83	-271.676	-1.472	0.09	2.2	2.29	203.22	38.63	-233.05	-232.23	-29.01
10MB0136	37.8386670	-118.9838330	2413.16	979271.4	979977.95	744.29	-270.029	-1.476	0.16	2.26	2.42	203.26	37.77	-232.26	-231.31	-28.05
10MB0137	37.8545000	-118.9801670	2431.08	979268.2	979979.34	749.81	-272.034	-1.472	0.2	2.42	2.62	203.24	38.69	-233.35	-232.2	-28.96
10MB0138	37.8606670	-118.9785000	2390.94	979275.6	979979.88	737.44	-267.542	-1.481	0.44	2.39	2.83	203.32	33.12	-234.42	-233.07	-29.75
10MB0139	37.8666670	-118.9753330	2328.37	979287.7	979980.41	718.15	-260.54	-1.494	0.29	2.34	2.63	203.44	25.42	-235.12	-233.99	-30.55
10MB0140	37.8731670	-118.9753330	2300.84	979293.3	979980.98	709.67	-257.46	-1.499	0.25	2.36	2.61	203.43	21.99	-235.47	-234.36	-30.93
10MB0141	37.8806670	-118.9725000	2255.03	979304.5	979981.63	695.54	-252.334	-1.505	0.22	2.33	2.55	203.53	18.44	-233.89	-232.85	-29.32
10MB0142	37.8946670	-118.9728330	2178.01	979317.8	979982.86	671.8	-243.715	-1.513	0.18	2.32	2.5	203.58	6.7	-237.01	-236.03	-32.45
10MB0143	37.8803330	-118.9611670	2268.84	979302	979981.61	699.8	-253.879	-1.503	0.1	2.16	2.26	203.51	20.17	-233.71	-232.95	-29.44
10MB0144	37.8733330	-118.9660000	2294.11	979296.6	979980.99	707.59	-256.707	-1.5	0.09	2.22	2.31	203.48	23.23	-233.47	-232.66	-29.18
10MB0145	37.8655000	-118.9670000	2317.82	979290.4	979980.31	714.9	-259.36	-1.496	0.12	2.23	2.35	203.46	25	-234.36	-233.51	-30.05
10MB0146	37.8581670	-118.9643330	2348.85	979283.9	979979.66	724.46	-262.832	-1.49	0.17	2.17	2.34	203.42	28.69	-234.14	-233.29	-29.87
10MB0147	37.8515000	-118.9583330	2372.78	979279.3	979979.08	731.84	-265.509	-1.485	0.19	2.12	2.31	203.42	32.11	-233.4	-232.58	-29.16
10MB0148	37.8448330	-118.9513330	2393.02	979274.5	979978.49	738.08	-267.774	-1.481	0.06	2.13	2.19	203.43	34.04	-233.73	-233.03	-29.6
10MB0149	37.8398330	-118.9521670	2398.11	979272.9	979978.06	739.65	-268.344	-1.48	0.1	2.13	2.23	203.42	34.52	-233.83	-233.08	-29.66
10MB0150	37.8315000	-118.9595000	2452.21	979262.4	979977.33	756.33	-274.398	-1.466	0.19	2.19	2.38	203.28	41.43	-232.96	-232.05	-28.77
10MB0151	37.8243330	-118.9578330	2445.41	979263.4	979976.7	754.23	-273.637	-1.468	0.16	2.16	2.32	203.28	40.92	-232.72	-231.87	-28.59
10MB0152	37.8023330	-118.9671670	2438.7	979266.4	979974.77	752.16	-272.887	-1.47	0.12	2.17	2.29	203.24	43.79	-229.1	-228.28	-25.04
10MB0153	37.7936670	-118.9718330	2469.03	979257.5	979974.01	761.51	-276.28	-1.462	0.12	2.3	2.42	203.11	44.96	-231.33	-230.37	-27.26
10MB0154	37.7976670	-118.9753330	2483.42	979258.9	979974.36	765.95	-277.89	-1.457	0.22	2.34	2.56	203.09	50.52	-227.37	-226.27	-23.18
10MB0155	37.7980000	-118.9891670	2489.39	979263.5	979974.39	767.79	-278.559	-1.456	0.18	2.4	2.58	203.01	56.9	-221.66	-220.53	-17.52
10MB0156	37.7916670	-119.0043330	2425.42	979266.9	979973.84	748.07	-271.4	-1.473	0.16	2.43	2.59	202.99	41.12	-230.28	-229.17	-26.18
10MB0157	37.7855000	-119.0048330	2431.27	979264.7	979973.3	749.87	-272.055	-1.472	0.09	2.52	2.61	202.92	41.26	-230.8	-229.66	-26.74
10MB0158	37.7786670	-119.0088330	2440.9	979260.8	979972.7	752.84	-273.132	-1.469	0.06	2.69	2.75	202.78	40.99	-232.15	-230.86	-28.08
10MB0159	37.7678330	-119.0228330	2473.57	979246.9	979971.75	762.91	-276.789	-1.46	0.73	3.29	4.02	202.46	38.05	-238.74	-236.18	-33.72
10MB0160	37.7655000	-119.0265000	2498.11	979241.4	979971.55	770.48	-279.534	-1.453	1.36	3.38	4.74	202.35	40.3	-239.23	-235.94	-33.59
10MB0161	37.7611670	-119.0268330	2533.89	979232.7	979971.17	781.51	-283.538	-1.442	1.6	3.45	5.05	202.22	43.01	-240.52	-236.92	-34.7
10MB0162	37.7585000	-119.0271670	2536.85	979231	979970.93	782.42	-283.869	-1.441	2.59	3.51	6.1	202.19	42.47	-241.4	-236.74	-34.55
10MB0163	37.7556670	-119.0243330	2527.1	979232.7	979970.69	779.41	-282.778	-1.444	1.69	3.5	5.19	202.19	41.45	-241.33	-237.58	-35.39
10MB0164	37.7521670	-119.0273330	2520.09	979234.5	979970.38	777.25	-281.993	-1.446	3.96	3.61	7.57	202.11	41.33	-240.67	-234.54	-32.43
10MB0165	37.7490000	-119.0233330	2494.48	979238.4	979970.1	769.36	-279.128	-1.454	1.94	3.57	5.51	202.18	37.62	-241.51	-237.45	-35.27
10MB0166	37.7485000	-119.0168330	2488.94	979239.6	979970.06	767.65	-278.508	-1.456	1.4	3.44	4.84	202.28	37.2	-241.31	-237.93	-35.65
10MB0167	37.9440000	-119.0961670	2055.42	979348.8	979987.19	634	-229.998	-1.517	0.18	3.78	3.96	203.38	-4.38	-234.38	-231.93	-28.55
10MB0168	37.9445000	-119.0900000	2029.85	979349.8	979987.23	626.12	-227.136	-1.516	0.3	3.55	3.85	203.46	-11.28	-238.41	-236.08	-32.62
10MB0169	37.9440000	-119.0806670	1974.59	979356.4	979987.19	609.08	-220.953	-1.514	0.18	3.48	3.66	203.6	-21.69	-242.64	-240.5	-36.9
10MB0170	37.9425000	-119.0703330	2004.09	979345.2	979987.05	618.18	-224.254	-1.515	0.19	2.94	3.13	203.59	-23.7	-247.96	-246.34	-42.75
LEEVIN	37.9556670	-119.1190000	2071.09	979348.3	979988.21	638.83	-231.751	-1.517	1.89	5.47	7.36	203.15	-1.07	-232.82	-226.98	-23.83
10MB1001	37.8871670	-119.0888330	2098.64	979337.5	979982.2	647.33	-234.834	-1.517	0.02	3.76	3.78	203.26	2.65	-232.18	-229.92	-26.66
10MB1002	37.8891670	-119.0850000	2093.55	979338.4	979982.38	645.76	-234.264	-1.517	0.01	3.6	3.61	203.3	1.76	-232.5	-230.41	-27.11
10MB1003	37.8911670	-119.0815000	2089.19	979339	979982.55	644.42	-233.777	-1.517	0.01	3.47	3.48	203.34	0.88	-232.9	-230.94	-27.6
10MB1004	37.8931670	-119.0778330	2085.35	979339.5	979982.73	643.23	-233.347	-1.517	0.01	3.36	3.37	203.36	0.04	-233.31	-231.46	-28.1
10MB1005	37.8951670	-119.0743330	2083.58	979339.5	979982.91	642.69	-233.149	-1.517	0.01	3.23	3.24	203.4	-0.74	-233.89	-232.17	-28.77
10MB1006	37.8975000	-119.0706670	2081.39	979339.5	979983.11	642.01	-232.904	-1.517	0.02	3.13	3.15	203.45	-1.63	-234.53	-232.9	-29.45
10MB1007	37.8995000	-119.0673330	2081.24	979339.2	979983.29	641.96	-232.887	-1.517	0.02	3.01	3.03	203.49	-2.09	-234.97	-233.46	-29.97
10MB1008	37.9021670	-119.0630000	2080.23	979338.9	979983.52	641.65	-232.774	-1.517	0.02	2.93	2.95	203.53	-2.98	-235.76	-234.32	-30.79

ID	LAT	LONG	ELEV_M	OG	TG	FAC	BC	CC	ITC	OTC	TTC	TISOC	FAA	SBA	CBA	ISO
10MB1009	37.9045000	-119.0595000	2080.32	979338.1	979983.72	641.68	-232.784	-1.517	0.03	2.87	2.9	203.54	-3.92	-236.7	-235.32	-31.78
10MB1010	37.9066670	-119.0560000	2081.51	979336.9	979983.91	642.05	-232.917	-1.517	0.06	2.81	2.87	203.56	-4.93	-237.85	-236.5	-32.94
10MB1011	37.9091670	-119.0521670	2083.92	979335.7	979984.13	642.79	-233.187	-1.517	0.15	2.74	2.89	203.57	-5.68	-238.86	-237.49	-33.92
10MB1012	37.9113330	-119.0491670	2087.58	979333.9	979984.32	643.92	-233.596	-1.517	0.24	2.66	2.9	203.58	-6.5	-240.1	-238.71	-35.13
10MB1013	37.9140000	-119.0456670	2088.92	979332.2	979984.56	644.33	-233.746	-1.517	0.41	2.6	3.01	203.57	-8.01	-241.76	-240.26	-36.69
10MB1014	37.9171670	-119.0431670	2093.49	979329.6	979984.83	645.74	-234.258	-1.517	0.51	2.54	3.05	203.55	-9.45	-243.71	-242.17	-38.62
10MB1015	37.9201670	-119.0401670	2082.88	979329.9	979985.1	642.47	-233.071	-1.517	0.75	2.51	3.26	203.58	-12.77	-245.84	-244.1	-40.52
10MB1016	37.9223330	-119.0365000	2079.68	979328.6	979985.29	641.48	-232.713	-1.517	1.07	2.47	3.54	203.59	-15.18	-247.89	-245.87	-42.28
10MB1017	37.9246670	-119.0330000	2070.08	979328.7	979985.49	638.52	-231.638	-1.517	0.85	2.43	3.28	203.62	-18.28	-249.92	-248.16	-44.54
10MB1018	37.9245000	-119.0285000	2042.04	979334.1	979985.48	629.88	-228.5	-1.517	1.25	2.49	3.74	203.69	-21.51	-250.01	-247.79	-44.1
10MB1019	37.9265000	-119.0230000	2008.45	979340.1	979985.65	619.52	-224.742	-1.516	0.81	2.57	3.38	203.76	-26.03	-250.77	-248.9	-45.14
10MB1020	37.9281670	-119.0190000	1994.37	979342.3	979985.8	615.18	-223.166	-1.515	0.4	2.58	2.98	203.79	-28.34	-251.51	-250.04	-46.25
10MB1021	37.9291670	-119.0145000	1989.28	979342.8	979985.89	613.61	-222.597	-1.515	0.22	2.56	2.78	203.79	-29.47	-252.07	-250.8	-47.01
10MB1022	37.9313330	-119.0106670	1986.56	979342.9	979986.08	612.77	-222.293	-1.514	0.09	2.47	2.56	203.79	-30.45	-252.74	-251.69	-47.9
10MB1023	37.9340000	-119.0073330	1987.2	979342	979986.31	612.97	-222.365	-1.514	0.1	2.35	2.45	203.8	-31.33	-253.7	-252.76	-48.96
10MB1024	37.9340000	-119.0036670	1977.73	979344.5	979986.31	610.05	-221.304	-1.514	0.07	2.36	2.43	203.8	-31.73	-253.03	-252.11	-48.31
10MB1025	37.9333330	-118.9991670	1975.01	979345.7	979986.25	609.21	-221	-1.514	0.06	2.36	2.42	203.82	-31.29	-252.29	-251.39	-47.57
10MB1026	37.9331670	-118.9945000	1982.18	979344.8	979986.24	611.42	-221.802	-1.514	0.07	2.28	2.35	203.8	-30.02	-251.82	-250.99	-47.19
10MB1027	37.9331670	-118.9900000	1989.58	979344.3	979986.24	613.7	-222.631	-1.515	0.08	2.21	2.29	203.77	-28.25	-250.88	-250.1	-46.33
10MB1028	37.9330000	-118.9856670	1995.5	979344.4	979986.22	615.53	-223.292	-1.515	0.07	2.14	2.21	203.75	-26.27	-249.56	-248.87	-45.12
10MB1029	37.9330000	-118.9806670	2001.5	979345	979986.22	617.38	-223.964	-1.515	0.08	2.1	2.18	203.71	-23.83	-247.79	-247.13	-43.42
10MB1030	37.9335000	-118.9750000	2015.34	979343.7	979986.27	621.64	-225.513	-1.516	0.14	2.02	2.16	203.69	-20.96	-246.47	-245.82	-42.13
10MB1031	37.9356670	-118.9715000	2027.56	979341.1	979986.46	625.41	-226.88	-1.516	0.18	1.93	2.11	203.61	-19.99	-246.87	-246.27	-42.66
10MB1032	37.9363330	-118.9665000	2035.03	979340.7	979986.51	627.72	-227.716	-1.516	0.09	1.89	1.98	203.63	-18.07	-245.79	-245.33	-41.7
10MB1033	37.9358330	-118.9618330	2035.76	979342.5	979986.47	627.94	-227.798	-1.516	0.06	1.9	1.96	203.64	-16.06	-243.86	-243.42	-39.78
10MB1034	37.9366670	-118.9571670	2039.57	979343.2	979986.54	629.12	-228.224	-1.517	0.05	1.89	1.94	203.62	-14.24	-242.47	-242.04	-38.42
10MB1035	37.9373330	-118.9536670	2037.86	979344.4	979986.6	628.59	-228.033	-1.517	0.05	1.88	1.93	203.6	-13.6	-241.63	-241.22	-37.62
10MB1036	37.9383330	-118.9478330	2038.96	979345.5	979986.69	628.93	-228.156	-1.517	0.04	1.88	1.92	203.58	-12.28	-240.43	-240.03	-36.45
10MB1037	37.9390000	-118.9435000	2040.79	979345.8	979986.75	629.49	-228.361	-1.517	0.05	1.88	1.93	203.56	-11.41	-239.77	-239.36	-35.8
10MB1038	37.9338330	-118.9386670	2063.83	979343.5	979986.29	636.6	-230.939	-1.517	0.1	1.92	2.02	203.52	-6.16	-237.1	-236.6	-33.08
10MB1039	37.9271670	-118.9408330	2083.09	979339.3	979985.71	642.54	-233.095	-1.517	0.13	1.97	2.1	203.53	-3.88	-236.98	-236.39	-32.86
10MB1040	37.9215000	-118.9440000	2103.79	979334.3	979985.21	648.92	-235.41	-1.517	0.13	1.98	2.11	203.54	-1.98	-237.39	-236.8	-33.26
10MB1041	37.9055000	-118.9528330	2158.62	979323.6	979983.81	665.82	-241.546	-1.514	0.15	2.06	2.21	203.58	5.63	-235.92	-235.23	-31.65
10MB1042	37.8981670	-118.9570000	2197.76	979317	979983.17	677.89	-245.925	-1.511	0.17	2.06	2.23	203.56	11.74	-234.18	-233.46	-29.9
10MB1043	37.8965000	-118.9623330	2189.62	979317.9	979983.02	675.38	-245.015	-1.512	0.17	2.12	2.29	203.6	10.28	-234.73	-233.96	-30.36
10MB1044	37.9040000	-118.9620000	2148.14	979325	979983.68	662.59	-240.373	-1.515	0.17	2.1	2.27	203.61	3.89	-236.48	-235.72	-32.11
10MB1045	37.9110000	-118.9575000	2117.32	979330.7	979984.29	653.09	-236.925	-1.516	0.15	2.08	2.23	203.61	-0.52	-237.44	-236.73	-33.12
10MB1046	37.9180000	-118.9553330	2086.97	979336.7	979984.91	643.73	-233.528	-1.517	0.13	2.06	2.19	203.61	-4.49	-238.02	-237.35	-33.74
10MB1047	37.9253330	-118.9550000	2067.67	979339.9	979985.55	637.78	-231.369	-1.517	0.07	1.99	2.06	203.61	-7.82	-239.19	-238.65	-35.04
10MB1048	37.9315000	-118.9546670	2050.97	979343	979986.09	632.63	-229.5	-1.517	0.05	1.94	1.99	203.61	-10.45	-239.95	-239.48	-35.87
10MB1049	37.9258330	-118.9808330	2028.84	979340.4	979985.59	625.81	-227.024	-1.516	0.1	2.17	2.27	203.73	-19.42	-246.44	-245.69	-41.96
10MB1050	37.9225000	-118.9888330	2029.57	979337.8	979985.3	626.03	-227.105	-1.516	0.14	2.33	2.47	203.73	-21.45	-248.56	-247.6	-43.87
10MB1051	37.9195000	-118.9986670	2030.36	979336	979985.04	626.28	-227.194	-1.516	0.36	2.55	2.91	203.73	-22.76	-249.95	-248.56	-44.83
10MB1052	38.0453330	-119.1588330	2100.44	979356.9	979996.08	647.88	-235.035	-1.517	0.09	5.32	5.41	202.65	8.7	-226.34	-222.44	-19.79
10MB1053	38.0468330	-119.1536670	2088.15	979359.7	979996.21	644.09	-233.661	-1.517	0.07	4.84	4.91	202.71	7.59	-226.07	-222.68	-19.97

ID	LAT	LONG	ELEV_M	OG	TG	FAC	BC	CC	ITC	OTC	TTC	TISOC	FAA	SBA	CBA	ISO
10MB1009	37.9045000	-119.0595000	2080.32	979338.1	979983.72	641.68	-232.784	-1.517	0.03	2.87	2.9	203.54	-3.92	-236.7	-235.32	-31.78
10MB1010	37.9066670	-119.0560000	2081.51	979336.9	979983.91	642.05	-232.917	-1.517	0.06	2.81	2.87	203.56	-4.93	-237.85	-236.5	-32.94
10MB1011	37.9091670	-119.0521670	2083.92	979335.7	979984.13	642.79	-233.187	-1.517	0.15	2.74	2.89	203.57	-5.68	-238.86	-237.49	-33.92
10MB1012	37.9113330	-119.0491670	2087.58	979333.9	979984.32	643.92	-233.596	-1.517	0.24	2.66	2.9	203.58	-6.5	-240.1	-238.71	-35.13
10MB1013	37.9140000	-119.0456670	2088.92	979332.2	979984.56	644.33	-233.746	-1.517	0.41	2.6	3.01	203.57	-8.01	-241.76	-240.26	-36.69
10MB1014	37.9171670	-119.0431670	2093.49	979329.6	979984.83	645.74	-234.258	-1.517	0.51	2.54	3.05	203.55	-9.45	-243.71	-242.17	-38.62
10MB1015	37.9201670	-119.0401670	2082.88	979329.9	979985.1	642.47	-233.071	-1.517	0.75	2.51	3.26	203.58	-12.77	-245.84	-244.1	-40.52
10MB1016	37.9223330	-119.0365000	2079.68	979328.6	979985.29	641.48	-232.713	-1.517	1.07	2.47	3.54	203.59	-15.18	-247.89	-245.87	-42.28
10MB1017	37.9246670	-119.0330000	2070.08	979328.7	979985.49	638.52	-231.638	-1.517	0.85	2.43	3.28	203.62	-18.28	-249.92	-248.16	-44.54
10MB1018	37.9245000	-119.0285000	2042.04	979334.1	979985.48	629.88	-228.5	-1.517	1.25	2.49	3.74	203.69	-21.51	-250.01	-247.79	-44.1
10MB1019	37.9265000	-119.0230000	2008.45	979340.1	979985.65	619.52	-224.742	-1.516	0.81	2.57	3.38	203.76	-26.03	-250.77	-248.9	-45.14
10MB1020	37.9281670	-119.0190000	1994.37	979342.3	979985.8	615.18	-223.166	-1.515	0.4	2.58	2.98	203.79	-28.34	-251.51	-250.04	-46.25
10MB1021	37.9291670	-119.0145000	1989.28	979342.8	979985.89	613.61	-222.597	-1.515	0.22	2.56	2.78	203.79	-29.47	-252.07	-250.8	-47.01
10MB1022	37.9313330	-119.0106670	1986.56	979342.9	979986.08	612.77	-222.293	-1.514	0.09	2.47	2.56	203.79	-30.45	-252.74	-251.69	-47.9
10MB1023	37.9340000	-119.0073330	1987.2	979342	979986.31	612.97	-222.365	-1.514	0.1	2.35	2.45	203.8	-31.33	-253.7	-252.76	-48.96
10MB1024	37.9340000	-119.0036670	1977.73	979344.5	979986.31	610.05	-221.304	-1.514	0.07	2.36	2.43	203.8	-31.73	-253.03	-252.11	-48.31
10MB1025	37.9333330	-118.9991670	1975.01	979345.7	979986.25	609.21	-221	-1.514	0.06	2.36	2.42	203.82	-31.29	-252.29	-251.39	-47.57
10MB1026	37.9331670	-118.9945000	1982.18	979344.8	979986.24	611.42	-221.802	-1.514	0.07	2.28	2.35	203.8	-30.02	-251.82	-250.99	-47.19
10MB1027	37.9331670	-118.9900000	1989.58	979344.3	979986.24	613.7	-222.631	-1.515	0.08	2.21	2.29	203.77	-28.25	-250.88	-250.1	-46.33
10MB1028	37.9330000	-118.9856670	1995.5	979344.4	979986.22	615.53	-223.292	-1.515	0.07	2.14	2.21	203.75	-26.27	-249.56	-248.87	-45.12
10MB1029	37.9330000	-118.9806670	2001.5	979345	979986.22	617.38	-223.964	-1.515	0.08	2.1	2.18	203.71	-23.83	-247.79	-247.13	-43.42
10MB1030	37.9335000	-118.9750000	2015.34	979343.7	979986.27	621.64	-225.513	-1.516	0.14	2.02	2.16	203.69	-20.96	-246.47	-245.82	-42.13
10MB1031	37.9356670	-118.9715000	2027.56	979341.1	979986.46	625.41	-226.88	-1.516	0.18	1.93	2.11	203.61	-19.99	-246.87	-246.27	-42.66
10MB1032	37.9363330	-118.9665000	2035.03	979340.7	979986.51	627.72	-227.716	-1.516	0.09	1.89	1.98	203.63	-18.07	-245.79	-245.33	-41.7
10MB1033	37.9358330	-118.9618330	2035.76	979342.5	979986.47	627.94	-227.798	-1.516	0.06	1.9	1.96	203.64	-16.06	-243.86	-243.42	-39.78
10MB1034	37.9366670	-118.9571670	2039.57	979343.2	979986.54	629.12	-228.224	-1.517	0.05	1.89	1.94	203.62	-14.24	-242.47	-242.04	-38.42
10MB1035	37.9373330	-118.9536670	2037.86	979344.4	979986.6	628.59	-228.033	-1.517	0.05	1.88	1.93	203.6	-13.6	-241.63	-241.22	-37.62
10MB1036	37.9383330	-118.9478330	2038.96	979345.5	979986.69	628.93	-228.156	-1.517	0.04	1.88	1.92	203.58	-12.28	-240.43	-240.03	-36.45
10MB1037	37.9390000	-118.9435000	2040.79	979345.8	979986.75	629.49	-228.361	-1.517	0.05	1.88	1.93	203.56	-11.41	-239.77	-239.36	-35.8
10MB1038	37.9338330	-118.9386670	2063.83	979343.5	979986.29	636.6	-230.939	-1.517	0.1	1.92	2.02	203.52	-6.16	-237.1	-236.6	-33.08
10MB1039	37.9271670	-118.9408330	2083.09	979339.3	979985.71	642.54	-233.095	-1.517	0.13	1.97	2.1	203.53	-3.88	-236.98	-236.39	-32.86
10MB1040	37.9215000	-118.9440000	2103.79	979334.3	979985.21	648.92	-235.41	-1.517	0.13	1.98	2.11	203.54	-1.98	-237.39	-236.8	-33.26
10MB1041	37.9055000	-118.9528330	2158.62	979323.6	979983.81	665.82	-241.546	-1.514	0.15	2.06	2.21	203.58	5.63	-235.92	-235.23	-31.65
10MB1042	37.8981670	-118.9570000	2197.76	979317	979983.17	677.89	-245.925	-1.511	0.17	2.06	2.23	203.56	11.74	-234.18	-233.46	-29.9
10MB1043	37.8965000	-118.9623330	2189.62	979317.9	979983.02	675.38	-245.015	-1.512	0.17	2.12	2.29	203.6	10.28	-234.73	-233.96	-30.36
10MB1044	37.9040000	-118.9620000	2148.14	979325	979983.68	662.59	-240.373	-1.515	0.17	2.1	2.27	203.61	3.89	-236.48	-235.72	-32.11
10MB1045	37.9110000	-118.9575000	2117.32	979330.7	979984.29	653.09	-236.925	-1.516	0.15	2.08	2.23	203.61	-0.52	-237.44	-236.73	-33.12
10MB1046	37.9180000	-118.9553330	2086.97	979336.7	979984.91	643.73	-233.528	-1.517	0.13	2.06	2.19	203.61	-4.49	-238.02	-237.35	-33.74
10MB1047	37.9253330	-118.9550000	2067.67	979339.9	979985.55	637.78	-231.369	-1.517	0.07	1.99	2.06	203.61	-7.82	-239.19	-238.65	-35.04
10MB1048	37.9315000	-118.9546670	2050.97	979343	979986.09	632.63	-229.5	-1.517	0.05	1.94	1.99	203.61	-10.45	-239.95	-239.48	-35.87
10MB1049	37.9258330	-118.9808330	2028.84	979340.4	979985.59	625.81	-227.024	-1.516	0.1	2.17	2.27	203.73	-19.42	-246.44	-245.69	-41.96
10MB1050	37.9225000	-118.9888330	2029.57	979337.8	979985.3	626.03	-227.105	-1.516	0.14	2.33	2.47	203.73	-21.45	-248.56	-247.6	-43.87
10MB1051	37.9195000	-118.9986670	2030.36	979336	979985.04	626.28	-227.194	-1.516	0.36	2.55	2.91	203.73	-22.76	-249.95	-248.56	-44.83
10MB1052	38.0453330	-119.1588330	2100.44	979356.9	979996.08	647.88	-235.035	-1.517	0.09	5.32	5.41	202.65	8.7	-226.34	-222.44	-19.79
10MB1053	38.0468330	-119.1536670	2088.15	979359.7	979996.21	644.09	-233.661	-1.517	0.07	4.84	4.91	202.71	7.59	-226.07	-222.68	-19.97

ID	LAT	LONG	ELEV_M	OG	TG	FAC	BC	CC	ITC	OTC	TTC	TISOC	FAA	SBA	CBA	ISO
10MB1054	38.0478330	-119.1495000	2078.13	979362.6	979996.29	641	-232.539	-1.517	0.04	4.52	4.56	202.73	7.3	-225.24	-222.19	-19.46
10MB1055	38.0490000	-119.1450000	2068.46	979364.6	979996.4	638.02	-231.457	-1.517	0.02	4.21	4.23	202.76	6.27	-225.19	-222.47	-19.71
10MB1056	38.0500000	-119.1406670	2064.08	979365.9	979996.48	636.67	-230.966	-1.517	0.02	3.95	3.97	202.79	6.07	-224.9	-222.44	-19.65
10MB1057	38.0511670	-119.1363330	2061.94	979366.8	979996.59	636.01	-230.728	-1.517	0.02	3.7	3.72	202.79	6.2	-224.53	-222.33	-19.54
10MB1058	38.0521670	-119.1321670	2059.11	979367.4	979996.68	635.14	-230.41	-1.517	0.03	3.52	3.55	202.8	5.85	-224.56	-222.53	-19.73
10MB1059	38.0538330	-119.1266670	2049.75	979368.8	979996.82	632.25	-229.363	-1.517	0.09	3.34	3.43	202.83	4.22	-225.15	-223.23	-20.4
10MB1060	38.0553330	-119.1218330	2052.37	979368.4	979996.95	633.06	-229.657	-1.517	0.07	3.15	3.22	202.83	4.53	-225.12	-223.42	-20.59
10MB1061	38.0566670	-119.1178330	2053.29	979369.6	979997.07	633.34	-229.759	-1.517	0.09	3.01	3.1	202.83	5.91	-223.85	-222.27	-19.44
10MB1062	38.0581670	-119.1130000	2052.04	979371.1	979997.2	632.96	-229.619	-1.517	0.16	2.87	3.03	202.84	6.89	-222.73	-221.22	-18.38
10MB1063	38.0595000	-119.1086670	2045.67	979373	979997.32	630.99	-228.906	-1.517	0.25	2.79	3.04	202.82	6.7	-222.21	-220.68	-17.86
10MB1064	38.0608330	-119.1045000	2037.07	979375.9	979997.44	628.34	-227.944	-1.517	0.29	2.72	3.01	202.84	6.82	-221.12	-219.63	-16.79
10MB1065	38.0621670	-119.1006670	2032.92	979376.7	979997.55	627.07	-227.481	-1.516	0.31	2.65	2.96	202.84	6.23	-221.25	-219.81	-16.97
10MB1066	38.0636670	-119.0961670	2030.91	979376	979997.68	626.44	-227.256	-1.516	0.25	2.58	2.83	202.82	4.8	-222.46	-221.15	-18.33
10MB1067	38.0648330	-119.0925000	2028.84	979375.1	979997.79	625.81	-227.024	-1.516	0.22	2.52	2.74	202.81	3.16	-223.86	-222.64	-19.83
10MB1068	38.0661670	-119.0885000	2023.45	979375.3	979997.9	624.14	-226.42	-1.516	0.24	2.48	2.72	202.83	1.53	-224.89	-223.68	-20.85
10MB1069	38.0676670	-119.0836670	2005.49	979379.1	979998.04	618.61	-224.411	-1.515	0.15	2.49	2.64	202.85	-0.32	-224.73	-223.61	-20.76
10MB1070	38.0693330	-119.0786670	1997.2	979380.2	979998.18	616.05	-223.483	-1.515	0.12	2.44	2.56	202.82	-1.91	-225.39	-224.34	-21.52
10MB1071	38.0693330	-119.0786670	1997.2	979381.6	979998.18	616.05	-223.483	-1.515	0.11	2.44	2.55	202.82	-0.56	-224.04	-223	-20.18
10MB1072	38.0718330	-119.0706670	1978.27	979383	979998.4	610.22	-221.365	-1.514	0.1	2.38	2.48	202.83	-5.16	-226.53	-225.56	-22.73
10MB1073	38.0733330	-119.0663330	1973.76	979384.4	979998.53	608.82	-220.861	-1.514	0.08	2.34	2.42	202.8	-5.34	-226.2	-225.3	-22.5
10MB1074	38.0745000	-119.0626670	1970.68	979383.9	979998.64	607.88	-220.516	-1.513	0.07	2.28	2.35	202.8	-6.82	-227.34	-226.5	-23.7
10MB1075	38.0758330	-119.0585000	1970.68	979382.9	979998.75	607.88	-220.516	-1.513	0.06	2.22	2.28	202.77	-7.96	-228.48	-227.71	-24.94
10MB1076	38.0773330	-119.0540000	1971.87	979383.6	979998.88	608.24	-220.649	-1.513	0.06	2.15	2.21	202.75	-7.09	-227.74	-227.04	-24.29
10MB1077	38.0788330	-119.0493330	1974.98	979380.5	979999.02	609.2	-220.997	-1.514	0.06	2.07	2.13	202.69	-9.3	-230.3	-229.68	-26.99
10MB1078	38.0801670	-119.0453330	1976.29	979380.5	979999.13	609.6	-221.144	-1.514	0.07	2.02	2.09	202.68	-9.07	-230.22	-229.64	-26.96
10MB1079	38.0811670	-119.0420000	1975.53	979380.8	979999.22	609.37	-221.058	-1.514	0.06	1.98	2.04	202.65	-9.09	-230.14	-229.62	-26.97
10MB1080	38.0826670	-119.0375000	1971.9	979381.5	979999.35	608.25	-220.653	-1.513	0.06	1.95	2.01	202.61	-9.58	-230.23	-229.73	-27.12
10MB1081	38.0840000	-119.0336670	1965.23	979382.8	979999.47	606.19	-219.906	-1.513	0.06	1.95	2.01	202.57	-10.5	-230.41	-229.91	-27.34
10MB1082	38.0855000	-119.0290000	1965.08	979383	979999.6	606.15	-219.889	-1.513	0.05	1.91	1.96	202.53	-10.46	-230.35	-229.9	-27.37
10MB1083	38.0866670	-119.0253330	1965.11	979382.9	979999.7	606.16	-219.892	-1.513	0.04	1.88	1.92	202.49	-10.67	-230.56	-230.16	-27.67
10MB1084	38.0881670	-119.0206670	1965.59	979382.2	979999.84	606.31	-219.947	-1.513	0.04	1.83	1.87	202.47	-11.3	-231.25	-230.89	-28.42
10MB1085	38.0895000	-119.0168330	1966.72	979381.8	979999.95	606.65	-220.073	-1.513	0.03	1.8	1.83	202.43	-11.47	-231.55	-231.23	-28.8
10MB1086	38.0910000	-119.0120000	1969.22	979380.8	980000.08	607.42	-220.352	-1.513	0.03	1.74	1.77	202.41	-11.83	-232.19	-231.93	-29.52
10MB1087	38.0921670	-119.0083330	1970.01	979380.1	980000.19	607.67	-220.441	-1.513	0.02	1.72	1.74	202.37	-12.41	-232.85	-232.63	-30.26
10MB1088	38.0936670	-119.0035000	1971.08	979379.2	980000.32	608	-220.56	-1.513	0.03	1.68	1.71	202.32	-13.14	-233.7	-233.5	-31.18
10MB1089	38.0955000	-118.9981670	1972.6	979377.8	980000.48	608.47	-220.731	-1.513	0.01	1.63	1.64	202.27	-14.17	-234.9	-234.77	-32.5
10MB1090	38.0968330	-118.9936670	1973.52	979377	980000.6	608.75	-220.833	-1.513	0.02	1.6	1.62	202.22	-14.87	-235.71	-235.6	-33.38
10MB1091	38.0990000	-118.9873330	1974.04	979376.6	980000.79	608.91	-220.891	-1.514	0.01	1.57	1.58	202.1	-15.3	-236.19	-236.13	-34.03
10MB1092	38.1003330	-118.9831670	1974.92	979376.1	980000.9	609.18	-220.99	-1.514	0.03	1.55	1.58	202.06	-15.62	-236.61	-236.54	-34.48
10MB1093	38.1018330	-118.9786670	1976.41	979375.3	980001.04	609.64	-221.157	-1.514	0.02	1.53	1.55	202.02	-16.13	-237.29	-237.25	-35.23
10MB1094	38.1031670	-118.9743330	1976.05	979374.7	980001.15	609.53	-221.116	-1.514	0.02	1.52	1.54	201.97	-16.97	-238.08	-238.06	-36.09
10MB1095	38.1046670	-118.9696670	1977.21	979373.8	980001.28	609.89	-221.246	-1.514	0.03	1.48	1.51	201.92	-17.61	-238.86	-238.86	-36.94
10MB1096	38.1061670	-118.9653330	1980.38	979372.4	980001.42	610.86	-221.601	-1.514	0.03	1.45	1.48	201.86	-18.12	-239.72	-239.75	-37.89
10MB1097	38.1113330	-118.9493330	1987.88	979370.2	980001.87	613.18	-222.44	-1.514	0.04	1.38	1.42	201.63	-18.46	-240.9	-240.99	-39.36
10MB1098	38.1168330	-118.9323330	2001.74	979369.2	980002.35	617.45	-223.992	-1.515	0.03	1.29	1.32	201.39	-15.67	-239.66	-239.85	-38.46

.

ID	LAT	LONG	ELEV_M	OG	TG	FAC	BC	CC	ITC	OTC	TTC	TISOC	FAA	SBA	CBA	ISO
10MB1099	38.1221670	-118.9158330	2024.91	979366.1	980002.82	624.59	-226.584	-1.516	0.03	1.2	1.23	201.08	-12.16	-238.75	-239.03	-37.95
10MB1100	38.1280000	-118.8980000	2042.5	979364.7	980003.33	630.02	-228.552	-1.517	0.02	1.14	1.16	200.77	-8.61	-237.16	-237.52	-36.75
10MB1101	38.1330000	-118.8825000	2061.82	979366.5	980003.77	635.97	-230.714	-1.517	0.03	1.1	1.13	200.46	-1.26	-231.98	-232.37	-31.91
10MB1102	38.1386670	-118.8646670	2076.48	979366.1	980004.27	640.49	-232.354	-1.517	0.06	1.1	1.16	200.17	2.3	-230.06	-230.41	-30.24
100101	37.8870000	-119.0891670	2099.1	979337.5	979982.19	647.47	-234.885	-1.517	0.02	3.77	3.79	203.26	2.79	-232.1	-229.83	-26.57
100102	37.8891670	-119.0851670	2092.6	979338.4	979982.38	645.47	-234.159	-1.517	0.02	3.62	3.64	203.31	1.48	-232.68	-230.55	-27.24
100103	37.8910000	-119.0816670	2089.46	979339	979982.54	644.5	-233.807	-1.517	0.01	3.48	3.49	203.33	0.97	-232.84	-230.87	-27.54
100104	37.8931670	-119.0776670	2085.05	979339.6	979982.73	643.14	-233.313	-1.517	0.01	3.36	3.37	203.36	-0.04	-233.35	-231.5	-28.14
100105	37.8951670	-119.0741670	2084.62	979339.5	979982.91	643.01	-233.265	-1.517	0.01	3.22	3.23	203.39	-0.43	-233.7	-231.99	-28.6
100106	37.8953330	-119.0740000	2083.03	979339.5	979982.92	642.52	-233.088	-1.517	0.01	3.23	3.24	203.4	-0.95	-234.04	-232.31	-28.91
100107	37.8978330	-119.0705000	2081.14	979339.4	979983.14	641.93	-232.876	-1.517	0.01	3.13	3.14	203.45	-1.78	-234.66	-233.03	-29.58
100108	37.9000000	-119.0665000	2081.33	979339.3	979983.33	641.99	-232.897	-1.517	0.01	2.99	3	203.51	-2.02	-234.92	-233.44	-29.93
100109	37.9030000	-119.0618330	2079.96	979338.8	979983.59	641.57	-232.743	-1.517	0.01	2.91	2.92	203.53	-3.27	-236.01	-234.61	-31.08
100110	37.9048330	-119.0590000	2080.29	979337.9	979983.75	641.67	-232.781	-1.517	0.02	2.86	2.88	203.55	-4.16	-236.94	-235.57	-32.02
100111	37.9071670	-119.0555000	2081.84	979336.9	979983.96	642.15	-232.955	-1.517	0.06	2.8	2.86	203.56	-4.91	-237.87	-236.52	-32.96
100112	37.9093330	-119.0520000	2084.86	979335.6	979984.15	643.08	-233.292	-1.517	0.14	2.73	2.87	203.57	-5.48	-238.77	-237.42	-33.85
100113	37.9118330	-119.0485000	2089.1	979333.6	979984.37	644.39	-233.766	-1.517	0.25	2.65	2.9	203.58	-6.39	-240.16	-238.78	-35.2
100114	37.9140000	-119.0455000	2089.83	979332.1	979984.56	644.61	-233.848	-1.517	0.43	2.59	3.02	203.56	-7.8	-241.65	-240.14	-36.58
100115	37.9171670	-119.0430000	2094.31	979329.7	979984.83	645.99	-234.35	-1.517	0.54	2.54	3.08	203.55	-9.18	-243.53	-241.97	-38.42
100116	37.9201670	-119.0401670	2084.25	979329.8	979985.1	642.89	-233.224	-1.517	0.73	2.51	3.24	203.58	-12.41	-245.63	-243.91	-40.33
10MB0191	38.0390000	-119.1676670	2139.06	979347.1	979995.52	659.79	-239.357	-1.515	0.66	6.26	6.92	202.51	11.35	-228.01	-222.6	-20.09
10MB0192	38.0338330	-119.1713330	2174.05	979337.9	979995.07	670.57	-243.272	-1.513	1.17	6.77	7.94	202.46	13.45	-229.82	-223.39	-20.93
10MB0193	38.0308330	-119.1790000	2223.73	979327.2	979994.8	685.89	-248.831	-1.509	2.76	7.47	10.23	202.27	18.27	-230.56	-221.84	-19.57
10MB0194	38.0323330	-119.1905000	2265.58	979314.8	979994.93	698.79	-253.514	-1.504	5.45	8.12	13.57	202.07	18.61	-234.9	-222.84	-20.77
10MB0195	38.0345000	-119.2056670	2323.55	979301.2	979995.12	716.66	-260.001	-1.495	6.78	8.85	15.63	201.78	22.69	-237.31	-223.17	-21.39
10MB0196	38.0338330	-119.2140000	2364.43	979293.6	979995.07	729.26	-264.575	-1.487	6.71	9.28	15.99	201.6	27.82	-236.75	-222.25	-20.65
10MB0197	38.0283330	-119.2388330	2380.46	979287.5	979994.58	734.21	-266.369	-1.484	10.17	11.99	22.16	201.15	27.11	-239.26	-218.59	-17.44
10MB0198	38.0271670	-119.2471670	2435.29	979276.7	979994.48	751.11	-272.505	-1.471	10.54	11.71	22.25	200.87	33.28	-239.22	-218.44	-17.57
10MB0199	38.0241670	-119.2528330	2462.36	979271.9	979994.22	759.45	-275.533	-1.463	9.95	11.89	21.84	200.69	37.12	-238.42	-218.04	-17.35
10MB0200	38.0316670	-119.2280000	2392.04	979284.8	979994.88	737.78	-267.665	-1.481	10.38	10.28	20.66	201.31	27.74	-239.92	-220.74	-19.43
10MB0201	37.9500000	-119.2098330	2631.95	979234.2	979987.71	811.73	-294.51	-1.407	14.33	8.9	23.23	200.74	58.18	-236.33	-214.51	-13.77
10MB0202	37.9476670	-119.1901670	2494.45	979266.5	979987.51	769.35	-279.125	-1.454	9.54	9.43	18.97	201.38	48.32	-230.8	-213.29	-11.91
10MB0203	37.9415000	-119.1813330	2403.01	979281	979986.97	741.16	-268.893	-1.478	11.35	9.68	21.03	201.65	35.19	-233.71	-214.15	-12.5
10MB0204	37.9335000	-119.1510000	2233.33	979321.1	979986.27	688.85	-249.906	-1.508	4.2	7.62	11.82	202.44	23.73	-226.17	-215.86	-13.42
10MB0205	37.9393330	-119.1350000	2196.48	979328.8	979986.78	677.49	-245.782	-1.512	2.51	6.15	8.66	202.73	19.53	-226.25	-219.1	-16.37
10MB0206	37.9443330	-119.1170000	2141.83	979341	979987.22	660.64	-239.667	-1.515	1.52	4.74	6.26	203.01	14.46	-225.2	-220.46	-17.45
10MB0207	37.8875000	-119.0995000	2109.73	979336.1	979982.23	650.75	-236.076	-1.516	0.03	4.2	4.23	203.14	4.58	-231.49	-228.78	-25.64
10MB0208	37.8820000	-119.1055000	2131.59	979330.9	979981.75	657.49	-238.521	-1.516	0.07	4.53	4.6	202.99	6.59	-231.93	-228.85	-25.86
10MB0209	37.8753330	-119.1083330	2151.49	979325	979981.17	663.62	-240.748	-1.515	0.17	4.71	4.88	202.85	7.5	-233.25	-229.88	-27.03
10MB0210	37.8613330	-119.1083330	2192.94	979314.9	979979.94	676.4	-245.387	-1.512	0.38	4.81	5.19	202.68	11.36	-234.03	-230.35	-27.67
10MB0211	37.8425000	-119.1180000	2186.54	979312.7	979978.29	674.43	-244.67	-1.512	2.58	6.99	9.57	202.36	8.87	-235.8	-227.74	-25.38
10MB0212	37.8531670	-119.1121670	2185.02	979315.1	979979.22	673.96	-244.5	-1.513	1.58	5.56	7.14	202.56	9.88	-234.62	-228.99	-26.43
10MB0213	37.8258330	-119.1208330	2191.79	979306.4	979976.83	676.05	-245.257	-1.512	4.92	8.86	13.78	202.1	5.65	-239.61	-227.34	-25.24
10MB0214	37.8181670	-119.1175000	2187.52	979305	979976.16	674.73	-244.779	-1.512	7.28	9.16	16.44	202.07	3.55	-241.23	-226.3	-24.23
10MB0215	37.8118330	-119.1091670	2175.11	979306.5	979975.6	670.91	-243.391	-1.513	8.4	8.17	16.57	202.19	1.83	-241.56	-226.51	-24.32

ID	LAT	LONG	ELEV_M	OG	TG	FAC	BC	CC	ITC	OTC	TTC	TISOC	FAA	SBA	CBA	ISO
10MB0216	37.8075000	-119.1088330	2187.82	979303.3	979975.22	674.82	-244.814	-1.512	9.67	8.05	17.72	202.11	2.9	-241.92	-225.71	-23.6
10MB0217	37.8003330	-119.1180000	2199.47	979301.5	979974.6	678.41	-246.116	-1.511	6.8	10.15	16.95	201.78	5.36	-240.75	-225.32	-23.54
10MB0218	37.7928330	-119.1225000	2207.76	979296.7	979973.94	680.97	-247.044	-1.511	4.8	11.56	16.36	201.54	3.75	-243.3	-228.45	-26.91
10MB0219	37.7855000	-119.1260000	2202.36	979293.8	979973.3	679.31	-246.44	-1.511	5.29	12.55	17.84	201.32	-0.18	-246.62	-230.29	-28.97
10MB0220	37.7745000	-119.1261670	2207.51	979289	979972.34	680.9	-247.017	-1.511	7.64	12.46	20.1	201.11	-2.43	-249.45	-230.86	-29.75
10MB0221	37.7690000	-119.1233330	2199.44	979290.1	979971.85	678.41	-246.113	-1.511	7.37	12.49	19.86	201.1	-3.39	-249.51	-231.16	-30.06
10MB0222	37.7625000	-119.1116670	2234.95	979288.2	979971.28	689.35	-250.086	-1.508	4.17	10.88	15.05	201.19	6.31	-243.77	-230.23	-29.04
10MB0223	37.7701670	-119.0891670	2300.48	979283.5	979971.96	709.55	-257.419	-1.499	2.11	6.94	9.05	201.71	21.14	-236.28	-228.72	-27.01
10MB0224	37.7741670	-119.0785000	2353.45	979274.5	979972.31	725.88	-263.347	-1.489	3.51	5.55	9.06	201.87	28.04	-235.3	-227.73	-25.86
10MB0225	37.7875000	-119.0668330	2340.13	979273.8	979973.47	721.78	-261.857	-1.492	6.3	4.36	10.66	202.29	22.15	-239.71	-230.54	-28.25
10MB0226	37.7971670	-119.0630000	2361.86	979274	979974.32	728.48	-264.288	-1.487	2.02	3.72	5.74	202.44	28.15	-236.14	-231.88	-29.44
10MB0227	37.8053330	-119.0568330	2333.76	979280.9	979975.03	719.81	-261.144	-1.493	0.76	3.48	4.24	202.65	25.72	-235.42	-232.67	-30.02
10MB0228	37.7411670	-118.9870000	2289.29	979276.6	979969.42	706.11	-256.168	-1.5	0.12	3.03	3.15	203.04	13.31	-242.85	-241.2	-38.16
10MB0229	37.7275000	-118.9920000	2336.35	979256.1	979968.22	720.61	-261.434	-1.492	0.08	2.98	3.06	202.71	8.46	-252.97	-251.41	-48.7
10MB0230	37.7251670	-119.0126670	2372.84	979258.4	979968.02	731.86	-265.516	-1.485	0.82	3.74	4.56	202.29	22.21	-243.31	-240.23	-37.94
10MB0231	37.7193330	-119.0158330	2388.78	979252.3	979967.51	736.78	-267.3	-1.482	1.17	3.79	4.96	202.1	21.53	-245.77	-242.29	-40.19
10MB0232	37.7141670	-119.0361670	2473.82	979239.3	979967.05	762.99	-276.816	-1.46	3.38	4.05	7.43	201.46	35.26	-241.56	-235.59	-34.13
10MB0233	37.7123330	-119.0550000	2536.12	979225.7	979966.89	782.19	-283.787	-1.441	3.28	4.79	8.07	200.9	40.98	-242.8	-236.17	-35.27
10MB0234	37.9235000	-119.0170000	2018.63	979339	979985.39	622.66	-225.881	-1.516	0.86	2.59	3.45	203.76	-23.77	-249.65	-247.72	-43.96
10MB0235	37.9170000	-119.0050000	2054.35	979331.6	979984.82	633.67	-229.878	-1.517	0.72	2.55	3.27	203.7	-19.52	-249.4	-247.65	-43.95
10MB0236	37.9041670	-118.9865000	2128.05	979323	979983.69	656.4	-238.125	-1.516	0.54	2.45	2.99	203.66	-4.28	-242.41	-240.93	-37.27
10MB0237	37.8728330	-118.8775000	2481.01	979268.9	979980.95	765.2	-277.621	-1.458	0.27	2.31	2.58	202.91	53.15	-224.47	-223.35	-20.44
10MB0238	37.8641670	-118.8713330	2547.18	979254.9	979980.19	785.6	-285.025	-1.438	0.23	2.62	2.85	202.84	60.33	-224.7	-223.29	-20.45
10MB0239	37.8483330	-118.8671670	2614.12	979234.3	979978.8	806.23	-292.515	-1.414	0.21	2.96	3.17	202.81	61.69	-230.83	-229.07	-26.26
10MB0240	37.8568330	-118.8830000	2509.08	979257.3	979979.55	773.86	-280.762	-1.45	0.25	2.46	2.71	203.02	51.58	-229.19	-227.93	-24.91
10MB0241	37.8516670	-118.9011670	2522.95	979248.4	979979.09	778.13	-282.314	-1.445	0.64	2.53	3.17	203.1	47.44	-234.87	-233.15	-30.05
10MB0242	37.8468330	-118.9165000	2526.18	979248.5	979978.67	779.13	-282.675	-1.444	0.21	2.54	2.75	203.14	48.95	-233.72	-232.42	-29.28
10MB0243	37.8368330	-118.9218330	2514.72	979250.6	979977.79	775.6	-281.393	-1.448	0.41	2.45	2.86	203.16	48.36	-233.04	-231.62	-28.46
10MB0244	37.7818330	-118.9383330	2419.75	979263.2	979972.98	746.32	-270.765	-1.474	1.42	2.35	3.77	203.37	36.54	-234.23	-231.93	-28.56
10MB0245	37.7761670	-118.9466670	2303.98	979282.3	979972.48	710.64	-257.812	-1.498	1.8	2.45	4.25	203.54	20.44	-237.37	-234.62	-31.08
10MB0246	37.7660000	-118.9425000	2308.62	979280.9	979971.59	712.06	-258.33	-1.497	0.54	2.38	2.92	203.5	21.36	-236.97	-235.55	-32.05
10MB0247	37.7593330	-118.9413330	2245.67	979292.6	979971.01	692.66	-251.287	-1.506	0.46	2.56	3.02	203.63	14.23	-237.06	-235.55	-31.92

NOTES:

ID	Station name
LAT	Latitude, in degrees (NAD27, south is negative)
LONG	Longitude, in degrees (NGVD29, west is negative)
ELEV_M	Elevation, in m
OG	Observed gravity, in mGal (IGSN 71)
TG	Theoretical gravity, in mGal (GRS67)
GRAVITY CORRECTIONS	
FAC	Free-air correction, in mGal (Swick, 1942)
BC	Bouguer correction, in mGal
CC	Curvature correction, in mGal (radius 166.7 km)
TERRAIN CORRECTIONS	
ITC	Inner-zone terrain correction, in mGal
OTC	Outer-zone terrain correction, in mGal (radius 166.7 km)
TTC	Total terrain correction, in mGal (166.7 km or 180 deg)
ISOSTATIC CORRECTIONS	
TISOC	Total isostatic correction
ANOMALIES	
FAA	Free-air anomaly, in mGal
SBA	Simple Bouguer anomaly, in mGal
CBA	Complete Bouguer anomaly reduced for a density of 2.67 g/cm3, in mGal
ISO	Isostatic gravity anomaly reduced for a density of 2.67 g/cm3, in mGal

APPENDIX D

TRUCK-TOWED MAGNETOMETER PROFILES

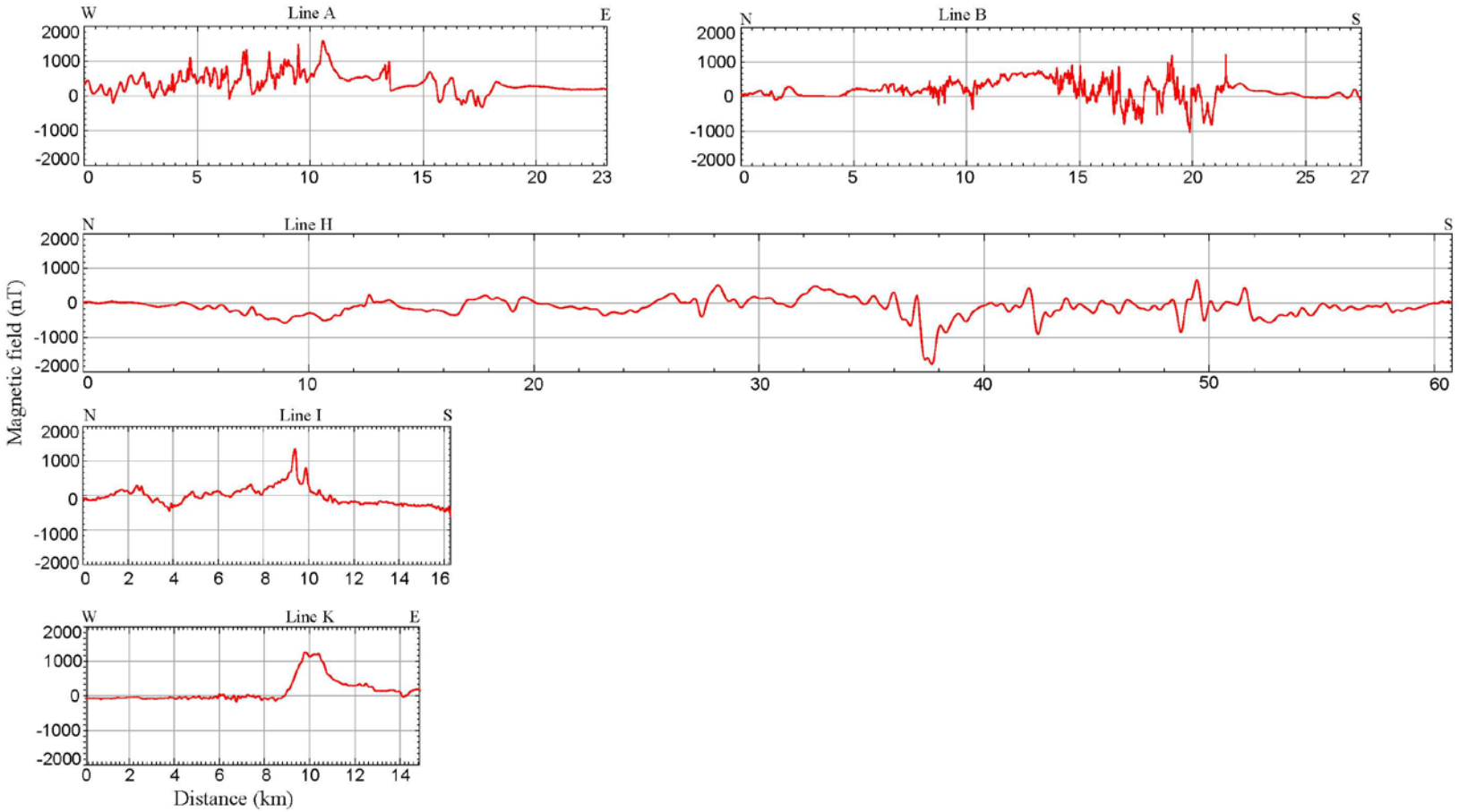
W
Line A
E
N
Line B
S
N
Line H
S
N
Line I
S
W
Line K
E
Magnetic field (nT)
Distance (km)

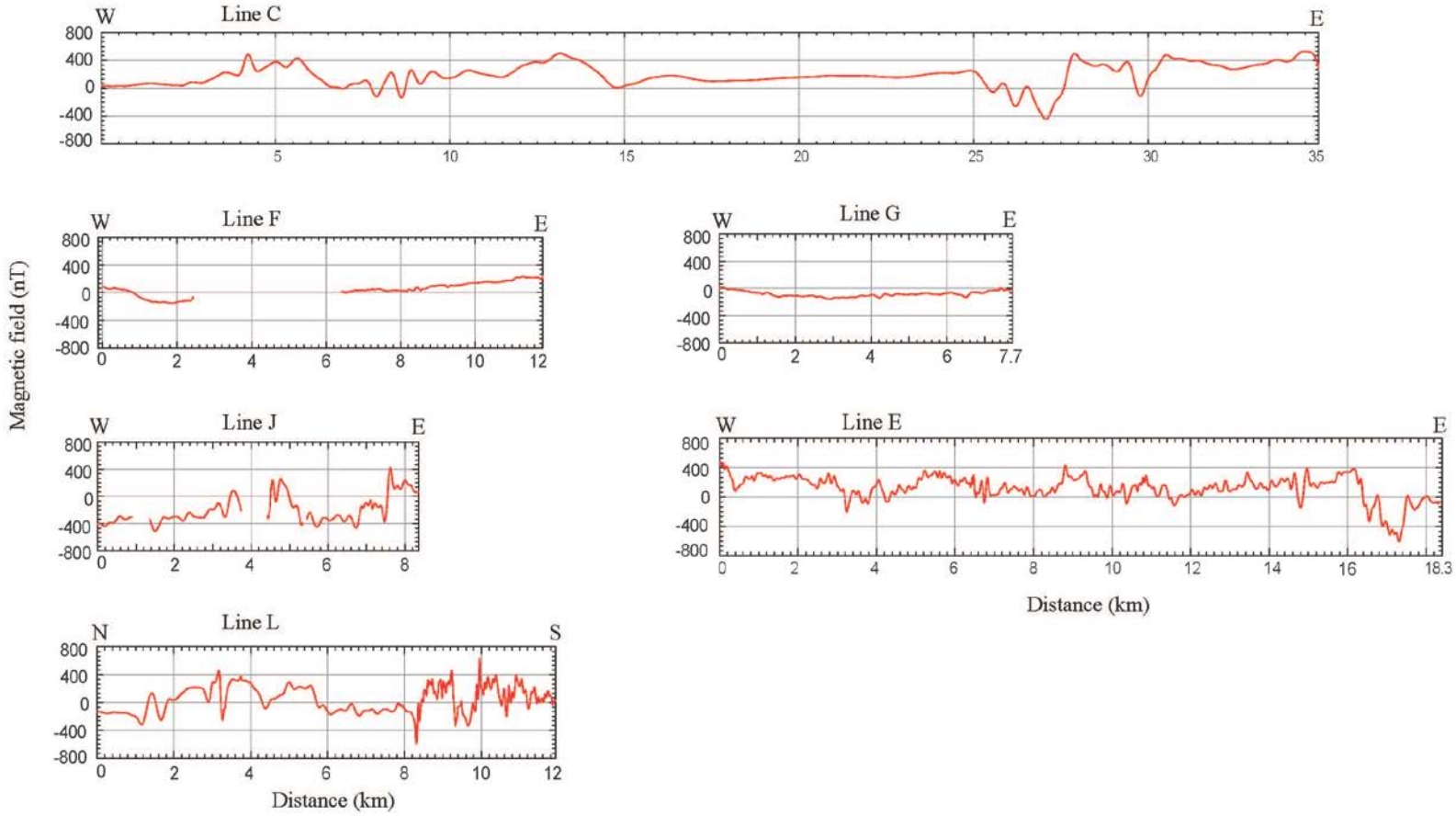
Line C
W
E
800
400
0
-400
-800
5
10
15
20
25
30
35
Line F
W
E
0
2
4
6
8
10
12
Line G
W
E
7.7
Line J
W
E
Line E
W
E
16
18.3
Distance (km)
Magnetic field (nT)
Line L
N
S
Distance (km)

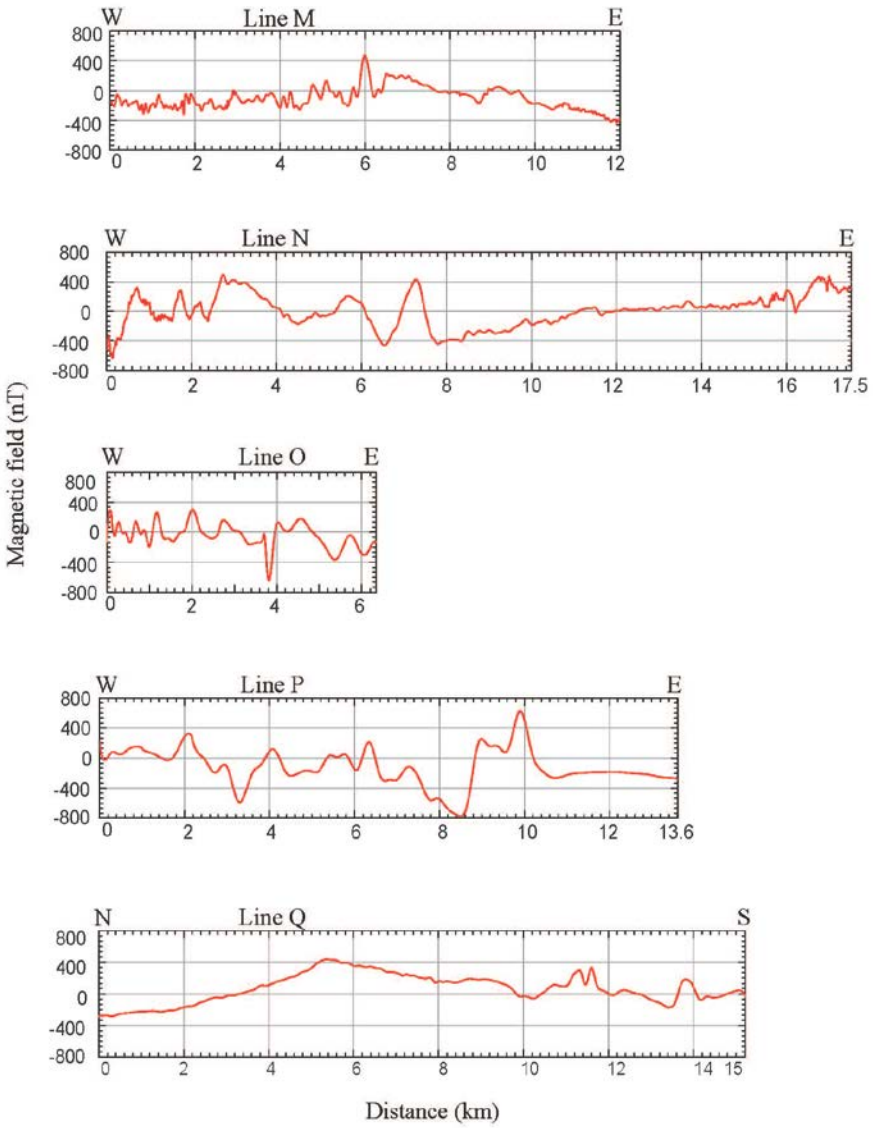
W
Line M
E
800
400
0
-400
-800
0
2
4
6
8
10
12
W
Line N
E
800
400
0
-400
-800
0
2
4
6
8
10
12
14
16
17.5
W
Line O
E
800
400
0
-400
-800
0
2
4
6
W
Line P
E
800
400
0
-400
-800
0
2
4
6
8
10
12
13.6
N
Line Q
S
800
400
0
-400
-800
0
2
4
6
8
10
12
14
15
Magnetic field (nT)
Distance (km)